UNIVERSITY OF CALIFORNIA

Los Angeles

Efficient Optical Coupling to the Nanoscale

A dissertation submitted in partial satisfaction of the
requirements for the degree Doctor of Philosophy
in Electrical Engineering

by

Josh Conway

2006

The dissertation of Josh Conway is approved.

Jia-Ming Liu

Chan Joshi

Russel Caflisch

Eli Yablonovitch, Committee Chair

University of California, Los Angeles

2006

TABLE OF CONTENTS

LIST OF FIGURES AND TABLES

Acknowledgements

I am indebted to many for their support during the research and writing of this thesis. First and foremost, I must thank my wife. She went to bed alone every night during the writing of this dissertation as I would work until sunrise. Even while pregnant and keeping the household running, she still had the time and energy to support me and keep me going when I needed it. And without even a single complaint of living off a grad student's salary, she is the hero of this dissertation.

I would also like to thank my advisor, Professor Eli Yablonovitch for sharing his unique view of science and the world. He has taught me many universal concepts which serve to add depth and perspective to my knowledge of physics and engineering. I am indebted to Prof. Russel Caflisch, another member of my thesis committee, for the insights into the taper design problem. It was refreshing to be able to intelligently discuss the plasmonic optimization problem with someone from a completely different background. I would also like to express my sincere thanks to Prof. Jia-Ming Liu and Prof. Chan Joshi for serving on my thesis committee, and making the time to participate in my qualifying examination.

Of course, what would acknowledgements be without giving thanks to those who gave me life and guided me along this path? My parents, Sonya and Carl, deserve a large amount of gratitude and thanks. Particularly, I would like to thank my mom, a professor herself, for showing me the satisfaction which accompanies successful research.

I am also hugely indebted to my lab-mates. They are the nuts and bolts of the operation, eager to give their time to help me when I was stuck. My former colleagues Adit Narasimha and Hans Robinson deserve special recognition for imparting their general interest in technology and physics. They were both always willing to stop whatever they were doing and help me through a confusing point of theory, or to just discuss the operating principles of some new-fangled device. My present colleagues, Subal Sahni and Thomas Szkopek have been a pleasure to work with, whether it is finding a cup of coffee at 2AM or debating feasibility of a novel idea. Finally, I would like to thank the rest of my plasmonics team. Shantha Vedantam, Hyojune Lee, and Japeck Tang have all worked hard in the pursuit of the device described in these pages. It is their tireless work which will demonstrate the unique power of the plasmonic lens, and to them I am very grateful.

I cannot forget to thank the many support staff who keep my paperwork to a minimum and allow us students to focus on science. My thanks go to Jaymie Otayde, Michael Aurelio and Deeona Columbia. They were all a pleasure to work with.

VITA

August 3, 1977	Born, Berkeley, California
1999	B.S., Physics, *summa cum laude* University of Illinois Urbana, Illinois
1999	Bronze Tablet Recipient
2001	M.S., Electrical Engineering University of Illinois Urbana, Illinois
2001-2002	Photonic Engineer Boeing Satellite Systems El Segundo, California
2002	Ursula Mandel Fellowship
2004	Electrical Engineering Departmental Fellowship

PUBLICATIONS AND PRESENTATIONS

J. Conway, F. Shen, C.M. Herring, J.G. Eden, and M.L. Ginter, "The $4p\pi{}^3\Pi_g$-$a{}^3\Sigma_u^+$ system in ${}^{20}\mathrm{Ne}_2$ and ${}^{22}\mathrm{Ne}_2$." *Journal of Chemical Physics*, vol 115, no. 11, pp 5126-5131 (2001).

J. Conway, A. Magerkurth, and S. Willenbrock, "Quarkonium Spectrum from Perturbation Theory," *European Journal of Physics*, vol 22, pp 533-540 (2001).

US Patent 7,006,725, "High Extinction Ratio Fiber Interferometer."

US Patent 6,924,894, "Temperature Compensated Interferometer."

US Patent 6,614,591, "High Power Optical Combiner."

D. M. Pianto, E. H. Cannon, J. Conway, Y. Lyanda-Geller, and D.K. Campbell, "Offset Potential in Finite Lateral Surface Superlattices", Meeting of the American Physical Society (1998).

ABSTRACT OF THE DISSERTATION

Efficient Optical Coupling to the Nanoscale

by

Josh Conway
Doctor of Philosophy in Electrical Engineering
University of California Los Angeles, 2006
Professor Eli Yablonovitch, Chair

Efficient confinement of the optical field to nanometer dimensions will enable an entire new class of low power optical devices. The range of devices that could be created is staggering. In addition to greatly enhancing microscopy and optical lithography, such an advance would allow for optical non-linearities with only a few photons. While the technological impetus is great, there is currently no device in the prior art which can achieve nanoscale optical focusing with any degree of efficiency. This dissertation presents the analysis and simulation of a novel plasmonic lens which can confine the optical field with astonishing efficiency. The key to the function of the device is the use of surface plasmons in a Metal-Insulator-Metal slab geometry. The unique dispersion of these modes allows for very large wave-vectors, achieving X-ray wavelengths with visible frequencies. This effect is exploited to achieve enhancements of the square of the electric field which are greater than 10^5 compared to that of the focus of a microscope objective. Through the use of extensive analysis and electromagnetic simulations, this novel device is demonstrated to have less than 10dB of loss when focusing the field of a visible photon to 3nm by 7nm.

CHAPTER 1 INTRODUCTION

The charm of history and its enigmatic lesson consist in the fact that, from age to age, nothing changes and yet everything is completely different.

-Aldous Huxley

This dissertation presents a novel plasmonic lens for efficiently coupling the optical field to the nanoscale. Through analysis, electromagnetic simulation and basic proof-of-concept experiments, the design presented herein is demonstrated to have higher energy concentration and greater efficiency than the prior art. To convey these results to the reader, the material is presented as follows. Chapter 1 gives the motivation and elementary background on optical focusing and surface plasmons. Chapter 2 details the precise design considerations of this plasmonic lens. Chapter 3 lays out the electromagnetic simulation results. Chapters 4-6 present more advanced topics and analyses of various applications.

1.1 Motivation

The ability to focus the optical field to deeply sub-wavelength dimensions opens the door to an entirely new class of photonic devices. If one could combine the imaging powers of X-ray wavelengths with the economy and maturity of visible light sources, one could greatly broaden the practical engineering toolbox. Imagine focusing visible photons to spatial dimensions less than ten nanometers. By doing so, electron beam microscopy is immediately displaced by optical microscopy, replacing expensive electron beam sources with inexpensive visible lasers. Beyond simple economics, though, this achievement would extend the range of nanometer scale microscopy to living biological samples and highly insulating surfaces.

In addition to the goal of nanoscale optical energy concentration and focusing, we add the constraint of efficiency. It is not sufficient to simply deliver optical energy to a nanoscale spatial regime. This coupling must be done efficiently, making this the watchword of this dissertation. Such powerful focusing could then be used to generate optical nonlinearities with very low photon counts. Enabling a suite of novel non-linear devices in passive optical geometries, this leads to novel optical switches, all-optical logic and highly sensitive detector arrays. All of these reasons compel us to address the physical and engineering principles that determine the smallest volume to which light can be efficiently focused.

A simple thought experiment can clarify some of the ramifications of efficient optical coupling to the nanoscale. Consider the energy of a single visible photon. For the sake of quantitative discussion, a red photon is chosen at 2eV, yielding a free space wavelength of 620nm. The reader is now asked to forego the objections of the Heisenberg Uncertainty Principle or the classical diffraction limit, and simply consider the energetic implications of confining the photon to a volume of 1nm^3. The details as to how we will arrive at such confinement are postponed until after the motivation has been established. This geometric scheme is illustrated in Figure 1-1.

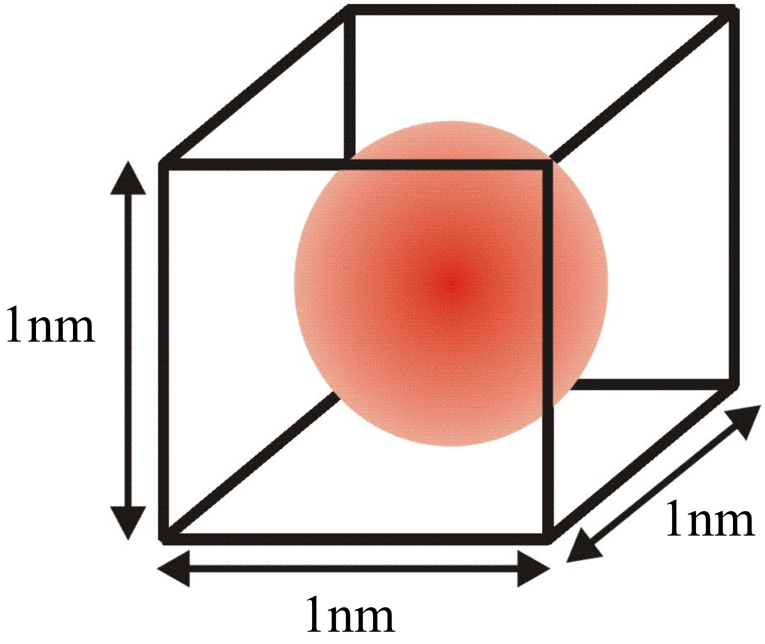

Figure 1-1: A single red photon confined to 1nm^3

Computing the optical energy density is now trivial. The energy of the photon is a known quantity, as is the volume. Turning the crank on this transparent equation yields

$$Energy\ Density = \frac{2eV}{\left(10^{-9}m\right)^3}\frac{1.6\times10^{-19}J}{eV} = 3\times10^{8}J/m^3 \qquad (1\text{-}1)$$

Optical energy density is not a standard figure of merit for most photonics engineers. To connect our humble photon to some standard of optical energy density we consider the sun. As the reader is well aware all life on earth, as well as most of the heat in our solar system, is powered by the optical energy radiating from the surface of the sun. The sun can be modeled as an ideal black body, which permits the use of a variation of the Stefan's law[1] to determine the radiant intensity over all wavelengths emanating from the sun's surface. Dividing the intensity by velocity yields the optical energy density, which is computed below, assuming a black body temperature of 5,400K.

$$Energy\ Density = \sigma T^4 / c = 0.2 J / m^3 \qquad (1\text{-}2)$$

The discrepancy between the energy densities of these systems is startling. The optical energy density, summed over all of the frequencies emanating from the sun, is more than *a billion times smaller* than that of a single red photon focused to the nanoscale. Clearly, compressed optical modes have enormous energy densities. In fact, the electric field of our nano-focused photon is on the order of 10^{10} V/m.

These levels of optical compression are great enough to achieve optical non-linearities in common materials with very low photon counts. For instance, Silica glass[2] has a non-linear index coefficient (n_2) of approximately 6 x 10^{-23} m^2/V^2. Achieving a 1% change in refractive index, then, requires only 8 photons. Employing more exotic nonlinear materials, such as lead-silicate or chalcogenides, will increase the changes in refractive index by orders of magnitude. Thus, focusing to the nanoscale will allow for a new regime of low-power nonlinear optics.

1.2 Nanoscale Focusing in a Diffractive World

There are, of course, several problems implicit in focusing light to deeply sub-wavelength dimensions. These limits for homogenous media come directly from Maxwell's Equations. We begin with Maxwell's Equations in differential form[3]

$$\nabla \times E = -\mu \frac{dH}{dt} \qquad (1\text{-}3)$$

$$\nabla \times H = J_f + \frac{dD}{dt} \tag{1-4}$$

These equations can be simplified for very high frequency fields. The magnetic response of a material involves currents which generally cannot respond at optical frequencies[4]. Although there are numerous magnetic dipole transitions for many natural media at optical frequencies[5,6], these tend to be very weak and are negligible for the materials in this thesis, making $\mu = \mu_0$. Likewise the free currents, represented by J_f, cannot respond at these frequencies, and they too are zero. The assumption of homogenous, isotropic linear media then allows us to eliminate the auxiliary field *H*. After some simplification, we arrive at the wave equation.

$$-\nabla^2 E = \frac{n^2\omega^2}{c^2} E \tag{1-5}$$

In the equation above, *n* represents the index of refraction which is equal to the square root of the relative dielectric constant (ε) of the medium. The electric field may now be decomposed into a complete basis set of plane waves[7], with k_i representing the spatial frequency in the direction *i*.

$$k_x^2 + k_y^2 + k_z^2 = \frac{n^2\omega^2}{c^2} \tag{1-6}$$

$$k_i \le \frac{n\omega}{c} = \frac{2\pi n}{\lambda_0} \tag{1-7}$$

This puts a fundamental limit on the achievable spatial wave-vector, which is constrained principally by the low indices of refraction in conventional optical materials. In the regime of low loss in the visible band of the spectrum, indices of refraction top out around 1.9 with flint glass[8]. This limits the maximum wave-vector to a spatial frequency of $4\pi/\lambda_0$. As is known in the art, the spot focus in the image plane can be represented as a Fourier transform of spatial frequencies. The above equations then set an upper limit on the frequency which thereby determines the minimum pitch at the image to be greater than $\lambda_0/2$.

The use of focusing optics in the regime of Fraunhoffer diffraction[9] drastically worsens the situation. As is typically the case with diffractive optics, a circular lens is used as the focusing element. This lens forms a circular aperture which acts as a low pass spatial filter with a maximum spatial frequency of $\frac{nD}{2\lambda_0 d_i}$. Here D represents the diameter of the lens and d_i is the distance from the lens to the image plane. With the high spatial frequencies cut-off, the circular optic creates an Airy disk[10] in the image plane, as illustrated in Figures 1-2(a) and 1-2(b). The diffraction limited spot is now limited to a minimum diameter of approximately $\frac{1.22\lambda_0}{NA}$, where the numerical aperture (NA) is defined as $n\sin\theta$. Although typically worse in practice, this then sets the minimum pitch to greater than 0.65 λ_0. Clearly, focusing to 1nm spot sizes is not possible using conventional focusing techniques at visible frequencies. To fulfill the promise of advanced microscopy and low-power non-linear optics, then, a new solution is needed.

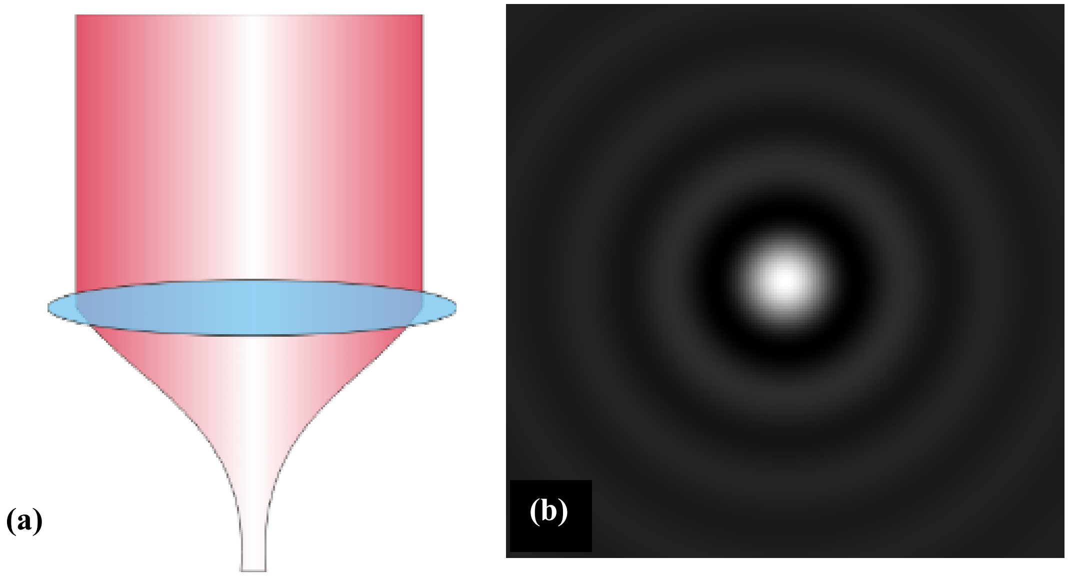

Figure 1-2: (a) Illustrates the diffraction limited spot size due to the clipping of the higher spatial frequencies. (b) shows the field pattern of an Airy disk.

1.3 Surface Plasmons, the Key to Optical Confinement

It is evident that deeply sub-wavelength focal spots cannot be formed through conventional focusing using a lens system or microscope objective. This is due, primarily, to the lack of high-index media at visible frequencies. What if, however, one was able to achieve a high *effective* index with conventional optical materials? That is the potential of surface plasmon optics. By employing geometries of conductors (such as metals or doped semiconductors) with dielectrics (such as air or glass), modes at optical frequencies can be created with effective indices of refraction that are orders of magnitude higher than those of the constituent materials. In fact, these indices can be so high as to create *X*-ray wavelengths (less than 10nm) with visible frequencies.

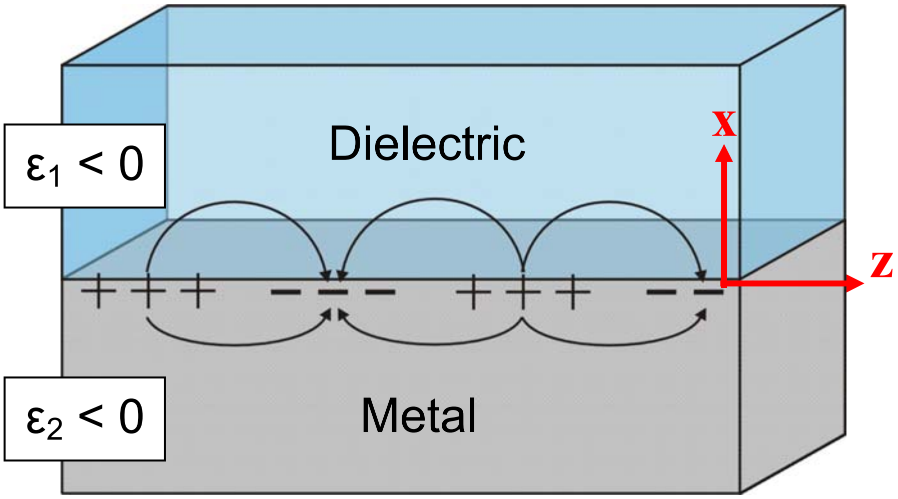

Figure 1-3: Geometry for single interface Surface Plasmon

The reason surface plasmon modes can achieve anomalously high wave-vectors at visible frequencies is because they are mediated by electrons rather than free space optical fields[11]. Surface plasmons are electron oscillations[12,13] at optical frequencies which are localized to the interface of a material with a positive dielectric constant and that of a negative dielectric constant (as illustrated in Figure 1-3). At wave-vectors much smaller than the Fermi wave-vector[12] of the conductor, these modes can be well described by Maxwell's Equations. Quantum mechanical considerations only become necessary at very short plasmon wavelengths, beyond the scope of this dissertation and are not required for determining the limits of efficient focusing. At low wave-vectors, the behavior of these surface modes can be understood intuitively. In this regime, they are essentially transverse in character, although strictly speaking they have a small longitudinal component. These transverse fields generate a polarization in the dielectric which is aligned with the stimulating field. In the metal, however, the polarization will be in the opposite direction of the applied field owing to its negative dielectric constant. Now we have a situation where the stimulating field is creating equal and opposite electric displacements (*D*), in phase with each other across an interface. These opposing electric displacements serve to attract and confine the current to this interface, thus generating the collective electron oscillations of the surface plasmon.

Starting from Maxwell's Equations, it is valuable to derive the characteristics of this simple plasmonic system. Again we take the free current to be zero and the relative permeability (μ_r) of all media to be unity. Following Economou[14], we will assume translational symmetry and homogeneity in the $\hat{y}$ direction (following the axes of Figure 1-3) and propagation with wave-vector k in the $\hat{z}$ direction. The behavior in the $\hat{x}$ direction is taken to be exponentially decaying away from the interface. Derived above in Equation (1-6), the wave equation tells us that the exponential decay constant in medium i must be

$$K_i^2 = k^2 - \frac{\varepsilon_i w^2}{c^2} \tag{1-8}$$

We now have enough information to determine the fields to within a scale factor. In the dielectric (medium 1), we define

$$E_{1x} = Ae^{-K_1 x} e^{i(kz-\omega t)} \tag{1-9}$$

The scalar quantity A represents a scale factor to be determined. From Gauss's Law we may derive E_z

$$E_{1z} = \frac{K_1}{ik} E_{1x} = A \frac{K_1}{ik} e^{-K_1 x} e^{i(kz-\omega t)} \tag{1-10}$$

Likewise for the conductor, we may derive E_x and E_z. In this case, we set the scale factor to unity, as only the relative scale factor carries importance.

$$E_{2x} = e^{K_2 x} e^{i(kz-\omega t)} \tag{1-11}$$

$$E_{2z} = -\frac{K_2}{ik} e^{K_2 x} e^{i(kz-\omega t)} \tag{1-12}$$

Applying the electromagnetic boundary conditions at the interface allows one to then solve for A. The continuity of E_z and D_x yield

$$A = \frac{\varepsilon_2}{\varepsilon_1} = -\frac{K_2}{K_1} \tag{1-13}$$

Some simple algebra may then be used to solve for k, finally generating the dispersion relation for these simple surface plasmon modes[15].

$$k = \frac{\omega}{c} \sqrt{\frac{\varepsilon_1 \varepsilon_2}{\varepsilon_1 + \varepsilon_2}} \tag{1-14}$$

The wave-vector is no longer a linear function of permittivity as in standard dielectrics. Because we have the sum of dielectrics of opposite sign in the denominator, very large wave-vectors are possible.

These wave-vectors, of course, are intimately tied to the dispersion of the constituent materials. One cannot discuss the plasmon dispersion relations without a model for the relative permittivities. Dielectric materials tend to have fairly constant permittivities over large bandwidths, while conductors tend to be very dispersive. To illustrate the dispersion relations of a typical material system, a Drude model[16] serves as a simple approximation for a metal. Here we will assume a lossless Drude metal and denote the plasma frequency as $\omega_{p.}$

$$\varepsilon_m = 1 - \frac{\omega_p^2}{\omega^2} \tag{1-15}$$

Taking free space as the dielectric material allows us to generate a dispersion relation, plotted in Figure 1-4. For generality, the frequency is plotted in units of the plasma frequency (ω_p) and the wave-vector in units of ω_p/c. As a point of reference, the light line is plotted as a grey dashed line and represents the dispersion relation of an optical field propagating in the dielectric medium along the same direction as the surface plasmon.

While this is a very simplified material system, there are two important characteristics of surface plasmons which are evident in this model. The first is that the dispersion relation always lies at higher wave-vectors than the light line. Due to the difference in wave-vector, then, the plasmon field cannot efficiently couple to radiating optical modes. Conversely, free-space optical fields cannot directly stimulate surface plasmons unless a mechanism introduces additional momentum. Of course, this result is to be expected from our initial assumptions. By defining the mode to have an exponential decay normal to the surface, we assured an imaginary wave-vector in this dimension. The absolute square of this positive quantity then adds to the light-line wave-vector to determine k^2 (as in Equation (1-6)), hence k must always be greater than that of the free space field.

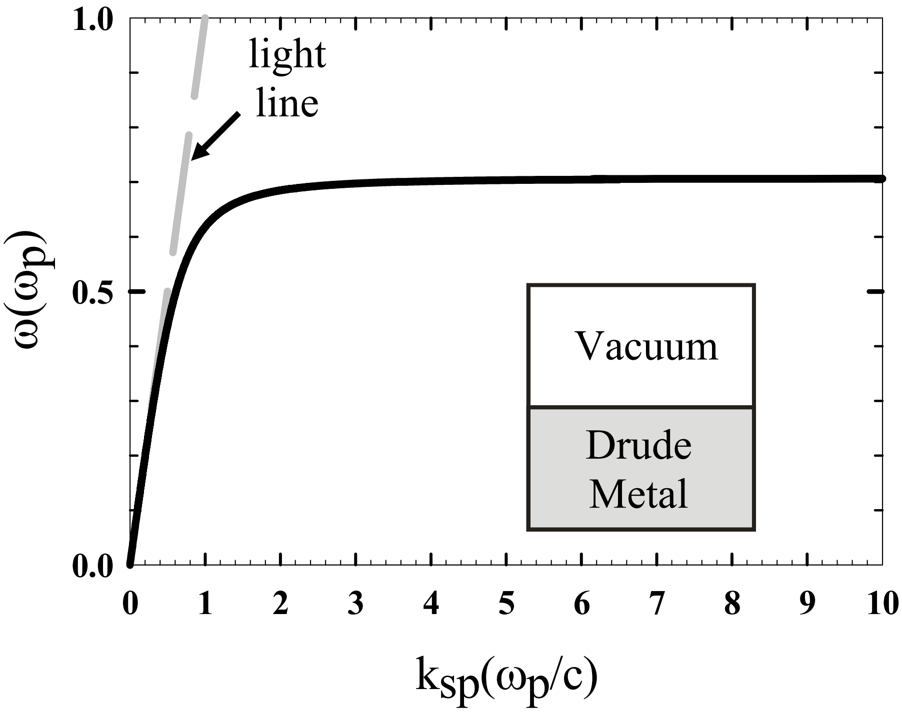

Figure 1-4: Dispersion relation for a Drude Metal plotted in units of the plasma frequency. The dashed line represents the light line.

The second defining feature of this dispersion relation occurs as the frequency approaches 0.7 ω_p. Here the wave-vector grows very large, orders of magnitude larger than the light line. It is precisely this feature which we will exploit to allow efficient focusing to the nanoscale. Although the permittivities of these materials may be modest, their geometry and interactions create an effective index much larger than that available from conventional transparent media. The reader may observe that these wave-vectors seem to violate Heisenberg's Uncertainty Principle[17] for optical fields in these materials. One resolution of this lies in the charge carrying fluid of electrons. Because these modes are mediated by collective electron oscillations with sub-Angstrom wavelengths, they may achieve very large *optical* wave-vectors. In the parlance of plasma physics, the energy is in the form of oscillating charge separations between the negative electrons and the positive ionic background of the metal, waves that extend to large wave-vectors.

1.4 Surface Enhanced Raman Scattering, a Proof of Principle

A proof of concept for the dramatic focusing powers of surface plasmons lies in the serendipitous discovery of Surface Enhanced Raman Scattering (SERS) more than 30 years ago[18]. In the original experiment, an optical field irradiated an electrochemical cell containing aqueous pyridine[19]. The spontaneous Raman intensity emanating from the cell was found to be enhanced by six orders of magnitude compared to that of aqueous pyridine without the presence of the cell[20]. Since that time, Raman enhancements of approximately 15 orders of magnitude[21,22] have been reported and it is now known that this enhancement is due to the interaction of the surface with the optical energy and the adsorbed particle. This effect has proved invaluable in chemical spectroscopy. Making the Raman Spectra detectable with less than 100μW of optical input power[23], this technique allows for the rapid identification of trace molecules by their unique Raman signature[24].

The basic geometry for SERS is simple. A molecule is adsorbed onto a rough metallic surface. For the metallic substrate, silver tends to show the greatest enhancement, although the other coinage metals have large enhancements as well. Most conductors, in fact, will show some enhancement[25]. The substrate is illuminated and the scattered light is collected. Besides collected radiation at the probe frequency, various other spectral lines are present. These are generated by the process of Raman scattering, and are due to the interaction of the probe radiation and the vibrational states of the adsorbed molecule. Because this scattering is so intimately related to the structure of the molecule, Raman scattering produces a unique distinguishing spectrum.

While clearly useful, SERS has proven difficult to pin down theoretically. In the time since its initial discovery, there has been little agreement as to the precise mechanisms responsible for this massive enhancement of the Raman process[26]. This is due to the combination of electromagnetic effects of the plasmon modes on the metallic surface as well as the chemical effects of the adsorbed particle interacting with the metallic surface. One certainty is that electromagnetic effects account for a significant part of the Raman intensity enhancement. This is due to the generation of localized surface plasmons. As mentioned in the previous sections, light cannot generate surface plasmons on planar surfaces. Rough surfaces, on the other hand, can add the missing momentum to create plasmons directly from the free-space optical field. These plasmons then have fields highly localized to the surface, precisely at the location of the adsorbed molecule. Various simulations[27] and analyses[25] have shown that these modes can account for at least six orders of magnitude of enhancement. Such a mode is shown in Figure 1-5, which plots the electric field in a 2D simulation of a nano-structured silver substrate illuminated from above with 2.6eV photons. The structure creates a 10x field enhancement near the adsorbed molecule.

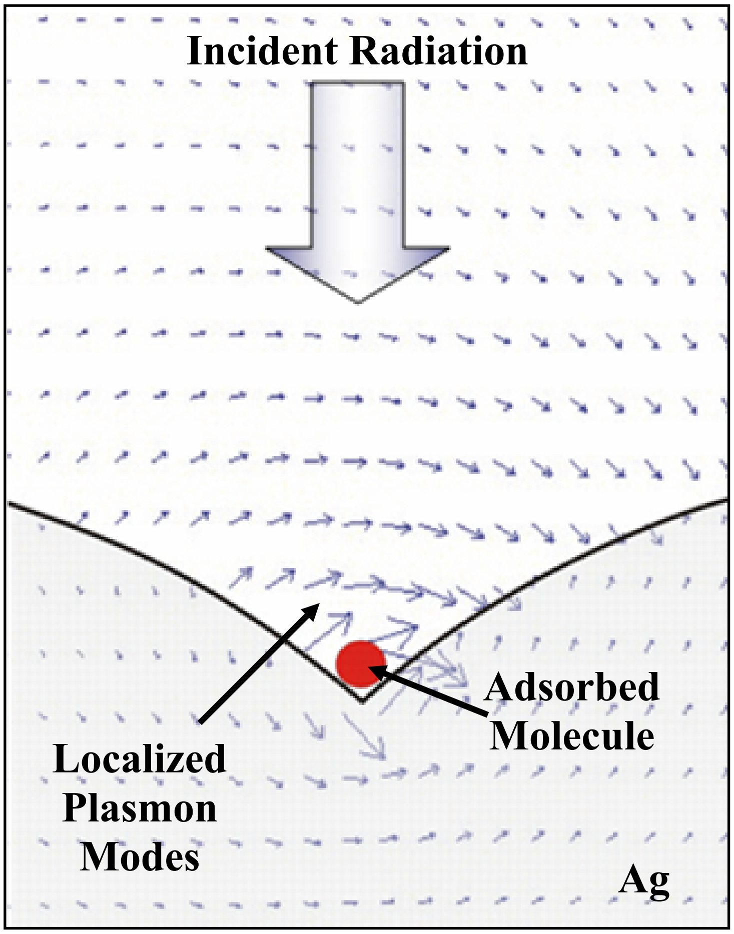

Figure 1-5: 2-d electromagnetic simulation showing the optical field enhancement on a rough silver surface

The reader will now wonder how these modes, with field enhancements of approximately one order of magnitude, can account for Raman intensity enhancements of six orders of magnitude. This can be explained by the enhancement of the scattered field[25]. The same mechanism which enhances the incident field will, by reciprocity, enhance the out-coupling and directionality of the scattered field. This gain is then squared again to account for the detected intensity, giving an approximate Raman gain of the field enhancement raised to the fourth power. Even greater Raman enhancements can be achieved when the rough metallic surface focuses the plasmons to localized hot-spots. This suggests that far greater enhancements may be attained by optimized structures in superior geometries. Engineering such controlled structures is the subject of this dissertation.

1.5 The Prior Art: Photo-assisted STM and Tapered Plasmonic Wires

As demonstrated by the incredible enhancements seen in Surface Enhanced Raman Scattering, even random roughness can lead to sharp focusing and localization of the optical field. It then falls to the engineer to construct optimized and reproducible devices which will fulfill the greater potential of surface plasmons. Because the benefits are so far-reaching, the pursuit of optical confinement at deeply sub-wavelength dimensions employing plasmons is a not new one. Most prominently, photo-assisted Scanning-Tunneling Microscopy (STM) has shown a great deal of success in the laboratory[28,29]. The scheme employs standard laboratory equipment to achieve very high field concentration in a controlled volume localized to the nanometer regime.

As illustrated in Figure 1-6, the technique involves a sharp metallic tip positioned nanometers above a conductive surface. This small gap between the two conductors is then illuminated with laser radiation polarized along the axis of the STM tip. The electric field of the optical beam drives oscillations of the free electron gas in the metal, which peaks at the tip. These plasmon oscillations propagate down the conical geometry, toward the apex and account for the very high field enhancements which occur even without the substrate. It must be noted that the field enhancements are far greater in the presence of the conducting surface, and this enhancement is very sensitive to the spacing between the tip and conductor[30]. A zeroeth order explanation for this effect can be understood by considering the gap as a very small capacitor. As the spacing is sub-wavelength, all of the optical voltage is across this gap. Thus, smaller gaps create larger fields. Theory has shown that this can lead to very large enhancements of the square of the electric field[28,31,32]. The greatest *measured* enhancement (known to the author) using a gold tip showed only a factor of 50 intensity enhancement[33]. This technique has proven itself very valuable in the laboratory environment. By combining high optical power with nanometer positioning, this technology has enabled a host of applications from optically trapping particles[28], to the nano-machining of metals[34].

Moving forward to higher field enhancements, greater efficiencies and robust construction will extend the range of previous applications and enable entirely new technologies. This, however, will require a large step forward in design. Photo-assisted STM is impeded by two fundamental problems. First is the delicacy of the tip. The atomically sharp tip resting nanometers above a substrate is not suitable for any applications outside of the controlled lab environment. Second is the intrinsic size mismatch between the free space beam and the nanoscale enhanced region. As discussed previously, the optical beam is diffraction limited to dimensions on the order of a micron. The intersection of the micron focal spot and nanometer tip creates an implicit loss mechanism in the design. Thus, Photo-assisted STM is inherently inefficient.

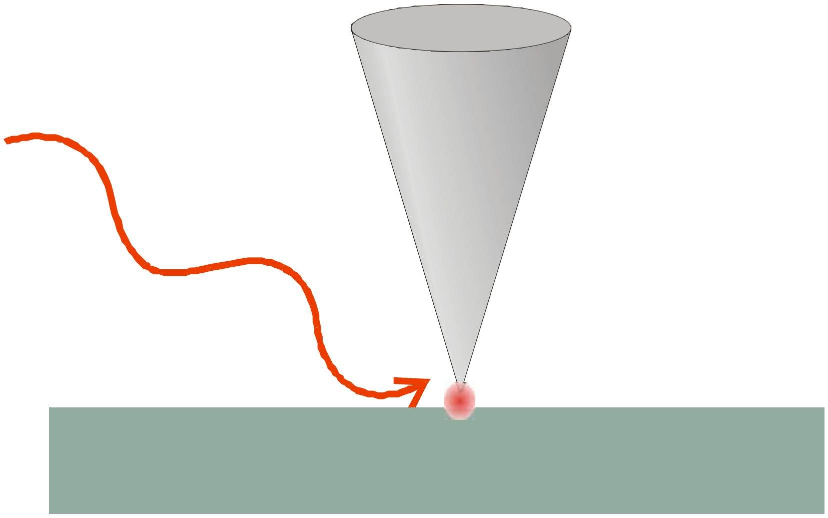

Figure 1-6: Technique for Photoassisted STM

A key physical process which contributes to the enhancement of the Photo-assisted STM is the propagation of plasmons down a tapered metallic wire. Although analogous to the geometry described above, this tends to be treated separately in the literature and is known as the Negative Dielectric (ND) pin[35]. This design is characterized by a solid cylinder of negative dielectric surrounded by a positive dielectric medium which extends to infinity. This geometry has the advantageous feature of a monotonically increasing *k*-vector with decreasing pin radius[36]. Classical calculations using bulk dielectric constants show no minimum cut-off radius. Therefore the pin has the capacity to focus the energy in both the transverse and longitudinal dimensions. Building on this, a cylindrical cone structure has been analyzed[37,38,39], creating a tapered plasmonic wire (see Figure 1-7). These analyses showed an E^2 enhancement on the order of thousands as the silver wire adiabatically tapers from 50nm to 2nm radius. Illustrating the potential of plasmonic focusing, the structure achieved these results because it not only confines the mode geometrically, but also temporally via reductions in the group velocity.

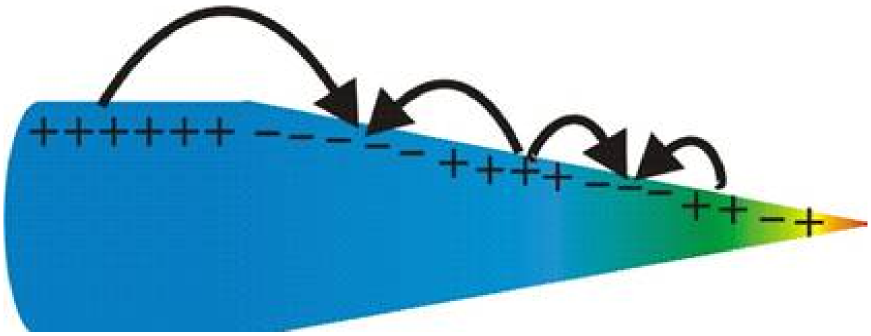

Figure 1-7: Tapered ND Pin Geometry

Calculations show that the adiabatically tapered pin yields large confinement and field enhancement, but it, too, is not a practical technique for achieving these results. It must be noted that the E^2 enhancement described above was calculated by ignoring the absorption effects of silver. We repeated the analysis of this device using the complex dielectric constant of silver, not merely the real part. When we include even optimistic numbers for the imaginary component of epsilon, our calculations yield an E^2 enhancement of approximately 40. As opposed to an enhancement on the order of thousands which was achieved in a lossless medium, the more realistic case is much less impressive. Reference 38 took the effects of electron scattering at the surface into account through the use of the Hydrodynamic Model[40], but ignored the more basic first order absorption effects. Clearly the previously published analyses are incomplete without thorough investigation of these effects and when taken into account, the adiabatic tapered pin is very inefficient. This design, while promising on paper, will not achieve efficient coupling to the nanoscale.

1.6 The Prior Art: Enhanced Transmission Apertures and Tapered Fiber Probes

Eliminating inefficiency is essential to the operation of low power devices. Various methods have been proposed to address these issues. Receiving the most press is the enhanced transmission effect through sub-wavelength apertures[41,42] which sparked a renewed wave of research in surface plasmons[43,44,45,46]. In this method, a free space optical field irradiates a metal film, typically 60-100nm thick. The film has a small cylindrical hole, generally with a grating[47] or hole array around it. Both the grating and array act to add the missing momentum to the free space beam, allowing surface plasmons to couple to the top side of the metal film (see Figure 1-8). These surface plasmons are loosely bound to a single side of the film but can evanescently couple to the opposite side of the film. Once propagating on the opposite side of the film, these plasmons will then out-couple at the hole to both the near and far field. The optical energy which transmits through the hole is then 'enhanced' compared to that which would be transmitted by strict diffraction in a non-conducting occluding film.

As a focusing method, this technique is fundamentally relegated to unacceptably low efficiencies when the out-coupled mode is smaller than 10nm. The problem lies in the classical skin depth. Because the free space photons can tunnel directly through very thin metal films, the metallic layer is required to be optically thick. This constraint immediately limits the plasmon wavelength which will achieve efficient evanescent tunneling[43] across the film. The large plasmon wavelength, in turn, disperses the energy in both the transverse and longitudinal directions, fundamentally limiting the ultimate focal size of the field.

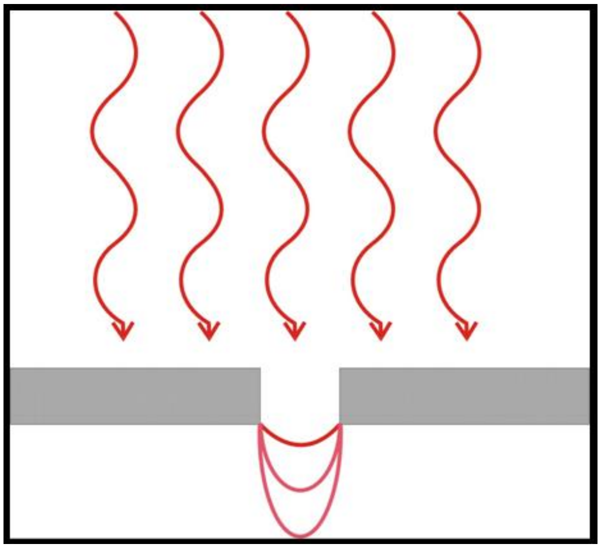

Figure 1-8: Geometry of enhanced transmission through sub-wavelength apertures

Finally, we present a method of coupling light to very small dimensions which does not employ surface plasmons. Tapered fiber probes, instead, create a very small aperture and thereby the transmitted light is localized to a very small focus. This is achieved by either pulling the fiber or chemically etching it into a tapered configuration. The fiber is then coated with a metal, typically Aluminum. An aperture is then created at the end of the tip by shaving back the metal to expose a very small aperture. The reader is warned not to confuse this geometry with that of a plasmonic waveguide. Metals are the only media which can block light with only tens of nanometers of thickness. These metals may therefore create the smallest possible aperture size at the apex, limited only by the skin depth of the metal. This scheme is illustrated in Figure 1-9.

This method is an open trade between efficiency and aperture size. Because the propagating modes of the fiber are cut off in the taper, the propagation is strictly evanescent. Therefore, the shortest tapers (generally achieved via chemical etching[48]) tend to have the highest throughput. The loss is also restricted by the poor transmission through the aperture[49]. These losses limit the apertures to larger than the skin depth because of the practicality achieving even moderate efficiencies. Typical losses tend to be 50-60dB for a 100nm diameter aperture, however losses of 20-30dB have been demonstrated for a triple tapered fiber[50] (also with a 100nm aperture). Clearly this is not an efficient or even plausible method of coupling to the nanoscale, but serves as an important benchmark.

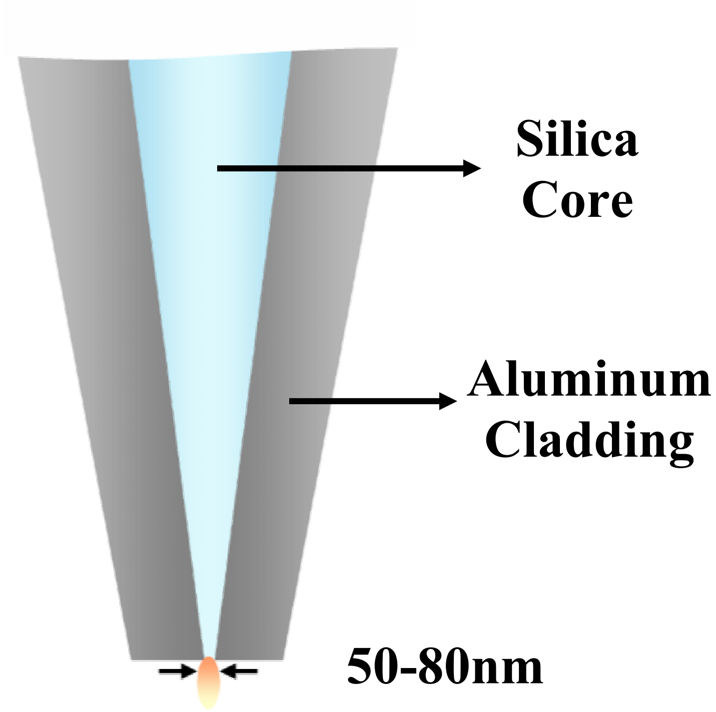

Figure 1-9: Operational schematic of tapered fiber probe

1.7 Looking to the Future

Efficient optical coupling to the nanoscale, suggested by the serendipitous success of Surface Enhanced Raman Scattering, has not been effectively demonstrated by the prior art. The inefficiencies of photoassisted STM tells us that a guided mode is necessary to bring the optical field to small dimensions. Good coupling, therefore, needs a traveling mode solution. The work with plasmonic wires shows that the design must take crippling propagation losses into account. In addition, the device must be designed based on potentially feasible fabrication techniques. In the remainder of this thesis, we present a design which addresses all of these issues and arrives at true efficient coupling to the nanoscale.

CHAPTER 2 MATERIALS AND DISPERSION

The important thing in science is not so much to obtain new facts as to discover new ways of thinking about them.

-Sir William Bragg

This chapter presents the fundamental engineering principles which make optical coupling to the nanoscale feasible. Throughout the text, efficiency is emphasized rather than simply achieving a small spot size. As is known in the field, the losses associated with even ideal materials can be devastating to efficient propagation. To this end, a quantitative analysis of materials systems is presented. Then we describe the dispersion relations and how they detail the physical mechanisms of efficient optical coupling. Finally we present our design for the novel plasmonic lens.

2.1 Materials Systems for Plasmonic Focusing

Effective nano-focusing is ultimately a function of efficiency. Before continuing to describe the design and analysis of our focusing device, we must digress to the material properties which govern the absorption and dispersion properties of the plasmon. Losses are implicit in confining a macroscopic optical field to nanoscale dimensions. Increasing field confinement and wave-vector leads to slower group and phase velocities. This increases the interaction time of the field with the loss mechanisms of the media, which in turn creates a proportionally degraded throughput. In fact, the losses can be catastrophic for certain systems, negating any advantages of field enhancement. To ignore this fact would remove any of the real-world engineering aspects of the problem and relegate it to a mere intellectual curiosity. This puts a premium on analysis of loss mechanisms and material properties.

Surface plasmon modes tend to be very lossy and the majority of this loss is due to absorption in the metal. The poor transmission properties of plasmons are described by their decay length, which is defined as the length over which the intensity decays by e^{-1}. Typical surface plasmon decay lengths are less than 10μm[51], while 'long range' surface plasmons can travel as far as hundreds of microns[52,53]. The long range plasmons capitalize on geometric and material effects which keep most of the field inside the dielectric media[54]. As is the case for all optimized waveguides, the decay lengths are limited by dissipation in the metal. As the electrons collectively oscillate at these surface plasmon frequencies, they collide with the background lattice of positive ions, transferring energy which is dissipated as heat. This powerful loss mechanism strongly constrains the design of any plasmonic device. For surface plasmons to achieve even modest levels of efficiency careful selection of materials and operating frequencies is required.

Ideally, a comparison of the modal Quality Factor (Q) over frequencies and materials would yield the ideal operating point. This trade study, though, is clouded by the realities of the system. Modal Q, which will henceforth be referred to as Q_{mod}, is determined by the details of the geometry of the plasmonic waveguide and the Q_{mod} can vary by orders of magnitude simply by altering the dimensions. It must be stressed that the loss is determined primarily by the properties of the conductor. Because of this, it is the intrinsic *Q* of the metal that is most important.

Material *Q* is a quantity which we introduce here to quantify the efficiency of large wave-vector plasmon propagation for various materials and frequencies. This metric originates from the classical expression for Q_{mod} in dispersive media. In such media, the derivative of the dielectric constant takes on added importance. The term $d(\omega\varepsilon)/d\omega$ replaces the relative dielectric constant (ε) in determining the energy of the electric field and *Q*-factor for the plasmon modes. This is especially significant in conductors where ε is negative and thermodynamics requires a positive electric-field energy. From Landau and Lifshitz[55] (although a more accessible derivation may be found in reference 56) the total energy stored in the field is given by

$$U = \frac{1}{2}\int\left(\frac{\partial\left(\omega\varepsilon_0\varepsilon'\right)}{\partial\omega}E^2 + \frac{\partial\left(\omega\mu_0\mu'\right)}{\partial\omega}H^2\right)d\tau \qquad (2\text{-}1)$$

The quantities ε_0 and μ_0 are the permittivity and permeability of free space, respectively while ε' and μ' are the real parts of the relative dielectric constant and relative permeability. The integral is taken over volume (τ). Equation (2-1) is derived in the literature for semitransparent dispersive media and, as the reader is well aware, good conductors tend to be highly reflective in the frequency range that supports surface plasmons (below the plasma frequency of the conductor). This is a far cry from transparency. The mathematical assumptions which lead to this definition of stored energy, however, do not strictly require transparency. They demand, instead, that the imaginary component of the wave-vector be small in comparison to the real component. This justifies the above formalism, even below the plasma frequency. Therefore, the expression is valid in the regime of interest. The average heat evolved in the material per unit time in the lossy medium is[55]:

$$\frac{dU}{dt} = \omega \int \left(\varepsilon_0 \varepsilon'' E^2 + \mu_0 \mu'' H^2 \right) d\tau \tag{2-2}$$

The terms ε'' and μ'' are the imaginary components of the relative dielectric constant and relative permeability. With these pieces in place, it remains to define the *Q*-factor as a function of frequency, which we will define as the modal *Q* (Q_{mod}).

$$Q_{\text{mod}} \equiv \frac{\omega U}{dU/dt} = \frac{\frac{1}{2}\int \left(\frac{\partial\left(\omega \varepsilon_0 \varepsilon'\right)}{\partial \omega} E^2 + \frac{\partial\left(\omega \mu_0 \mu'\right)}{\partial \omega} H^2 \right) d\tau}{\int \left(\varepsilon_0 \varepsilon'' E^2 + \mu_0 \mu'' H^2 \right) d\tau} \tag{2-3}$$

Equation (2-3) can be simplified by remembering that the imaginary component of the permeability (μ'') tends to zero at optical frequencies. We may then work from this to define a quantity known as the material *Q* (Q_{mat}) which only takes the electrical energy into account, dropping the second term from the numerator of Equation (2-3). As will be shown explicitly in Chapter 4, the energy stored in the magnetic field becomes negligible at large wave-vectors. This then simplifies Equation (2-3) to a function only of the electric field and modal geometry. Now we define the material *Q* (Q_{mat}) by integrating Equation (2-3) only over the spatial region of the metal. Because the material *Q* is only integrated over a single material, it can then be simplified, canceling the integral over E^2. This yields the contribution to the modal *Q* due strictly to the portion of the field which penetrates the metal and which is the chief limitation to achieving high Q_{mod}.

$$Q_{mat} \equiv \frac{\frac{1}{2}\int_{material} \frac{\partial(\omega\varepsilon')}{\partial\omega} E^2 d\tau}{\int_{material} \varepsilon'' E^2 d\tau} \tag{2-4}$$

$$Q_{mat} \equiv \frac{\partial(\omega\varepsilon')/\partial\omega}{2\varepsilon''} \tag{2-5}$$

Cast in the simple form above, we now may evaluate the material Q factors for various high-conductivity metals. We used the experimentally determined dielectric constants of silver[57,58,59,60], gold[61], aluminum[62] and copper[61]. The results, plotted in Figure 2-1, illustrate why plasmon modes have such poor propagation characteristics. Silver has the highest Q_{mat} factor, topping out around 30, while the other materials lie below 20. Various tricks can be played to keep the modal energy in the low loss dielectric, but at high k-vectors, a significant fraction of the energy must penetrate into the metal.

The material Q not only places silver far above the other conventional conductors for supporting surface plasmons, but it limits the bandwidth of efficient operation. Clearly the efficiency is diminished when operating outside of the photon frequency range of 2eV-3eV. These intrinsic material properties create a fundamental barrier which limits broadband plasmonic applications at large wave-vectors.

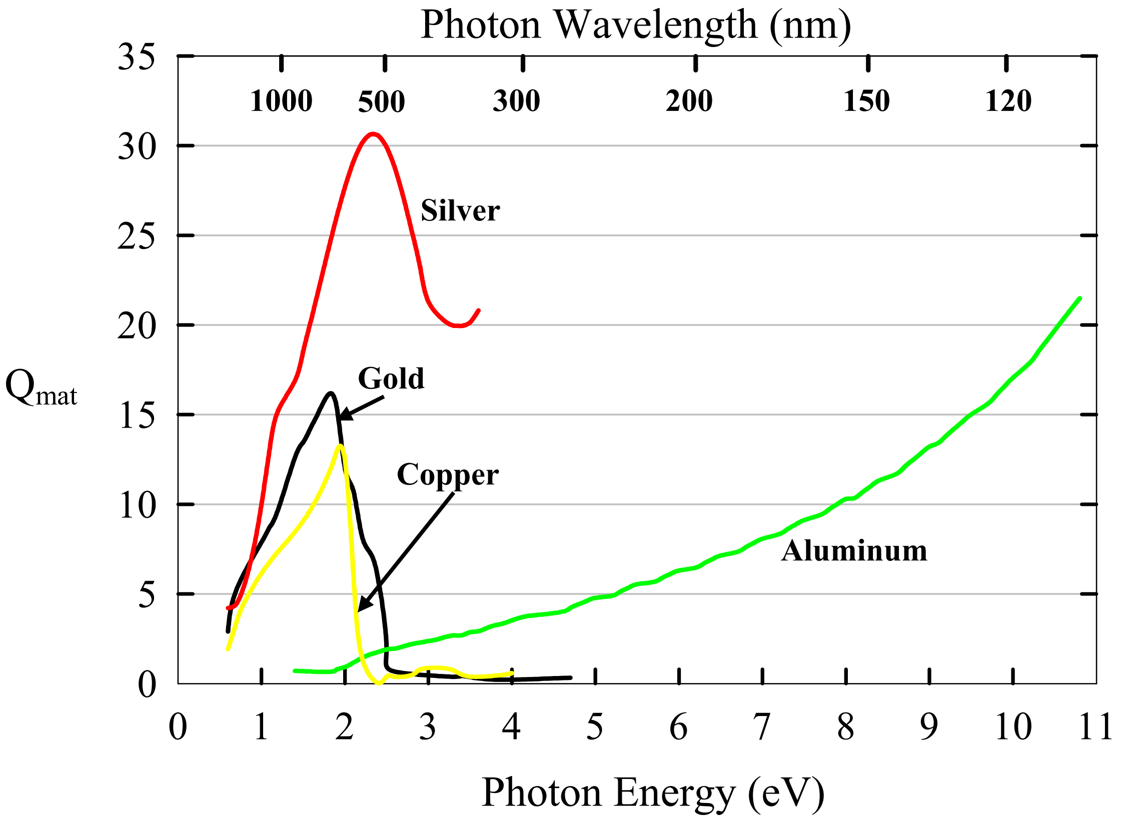

Figure 2-1: Material Q for various good conductors

While the optical properties of silver are favorable, the physical mechanisms that create them are a challenge to model. As is known in the field, the dielectric constant of silver cannot be adequately represented simply by the intraband transitions of a Drude character. This is because there is a mixture of free-electron states with a polarizable d-band[63], causing the plasma frequency to be pushed down from ~9eV, where it would sit in the absence of interband transitions. This is graphically illustrated in the works of Ehrenreich and Phillip[64], which clearly illustrate the onset of interband transitions near 4eV. In the region of interest, this can be modeled with an additional term added to the

Drude model with a value of approximately 5[63]. The surface plasmon parameters are very dependent on the material constants, so these approximations could not be made for our calculations. In fact, the experimentally determined optical constants must be used in any thorough analysis. In this work, we used the tabulated values for evaporated silver. Over the region of interest (from 1.2 eV to 3.2eV), an analytical fit of the experimental data was used. In these empirical fits, $\hbar\omega$ is the photon energy in electron Volts.

$$\varepsilon'(\hbar\omega) = -7.62 - 356e^{-1.72\hbar\omega} + 1.8\hbar\omega \tag{2-6}$$

$$\varepsilon''(\hbar\omega) = 2.77 - \frac{16.1}{\hbar\omega} + \frac{31.2}{\left(\hbar\omega\right)^2} - \frac{16.3}{\left(\hbar\omega\right)^3} \tag{2-7}$$

A spline fit was used to interpolate between experimentally derived values outside of our range of interest. The real and imaginary components of the dielectric constant are shown in Figure 2-2 and Figure 2-3, respectively. As will be discussed below, the real part of epsilon will determine the plasmon wavelength and the imaginary part determines the magnitude of absorption. Note that the magnitude of the real part of epsilon is always more than ten times greater than that of the imaginary part over the region of interest. Additional plots and tables on the properties of silver are given in Appendix A.

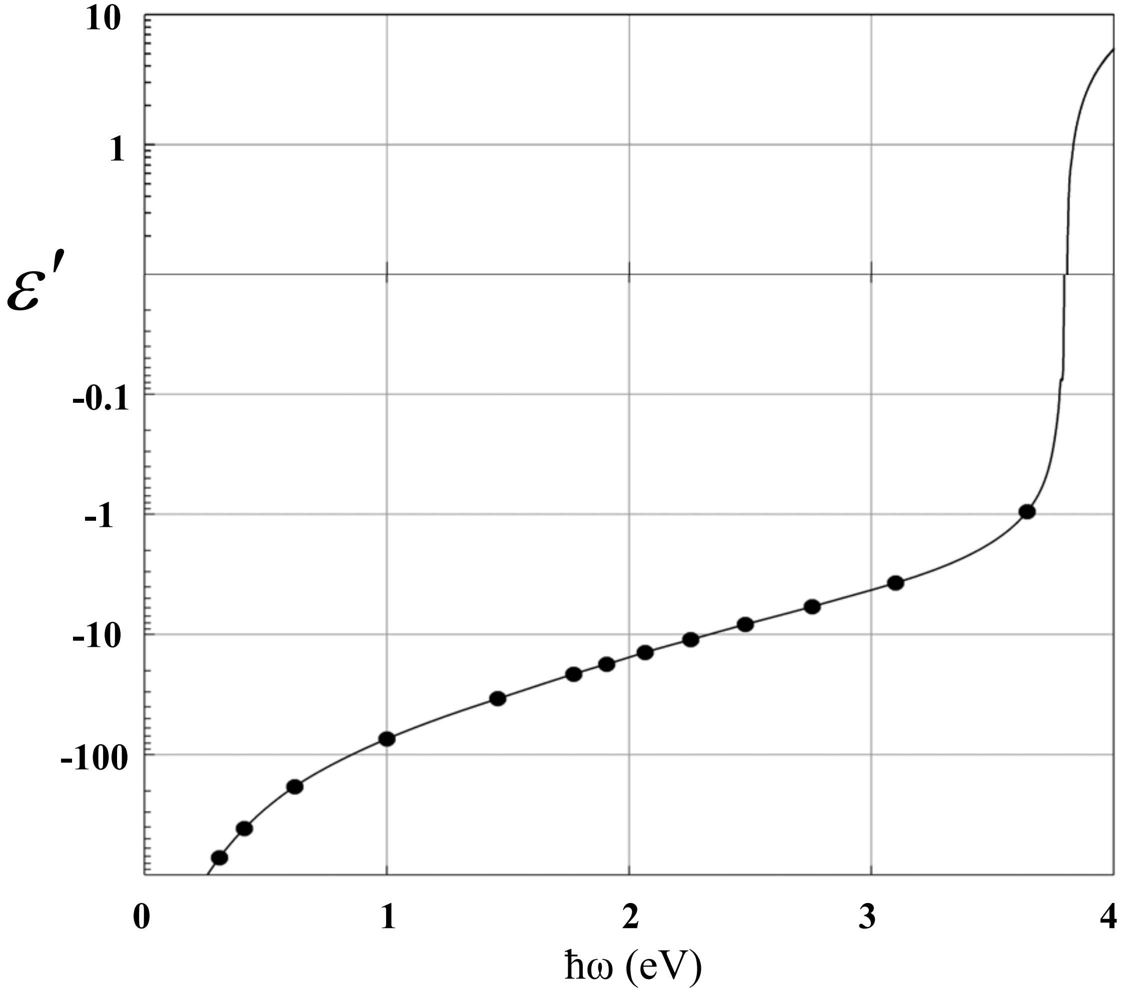

Figure 2-2: Empirical real component of the dielectric constant of silver

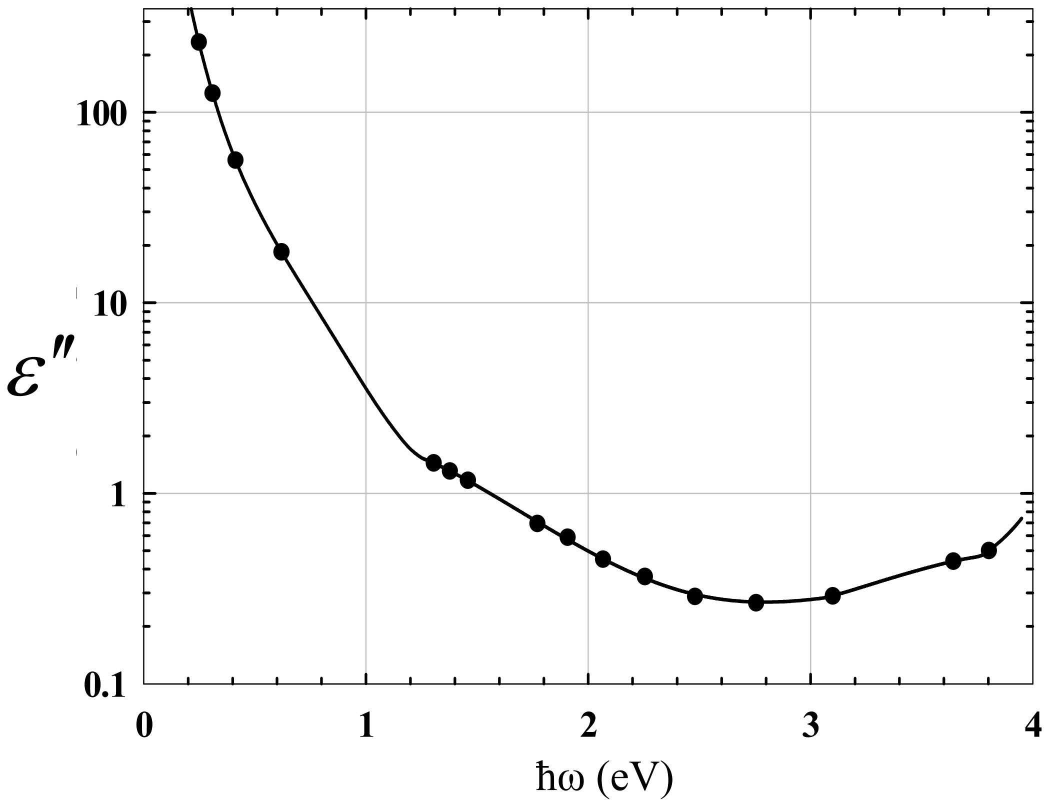

Figure 2-3: Empirical imaginary component of the dielectric constant of silver

2.2 Double Sided Plasmons

For our plasmonic focusing device, we have chosen a system very different from those discussed in Chapter 1. To create a compact device that is useful for real world applications, we need low loss and a robust design which lends itself to modern nano-fabrication technology. Addressing these concerns, we have dismissed the ND hole and pin geometries and chosen to build upon slab mode plasmons. Specifically, we will work with double sided slab plasmons in the micro-strip wave-guide configuration. This geometry consists of a thin planar film which is symmetrically surrounded by a medium of the opposite dielectric constant. This layout and plasmon mode profile is illustrated in Figure 2-4 for this metal-insulator-metal (MIM) scheme. The basic structure is analogous to conventional micro-strip, shown in Figure 2-5.

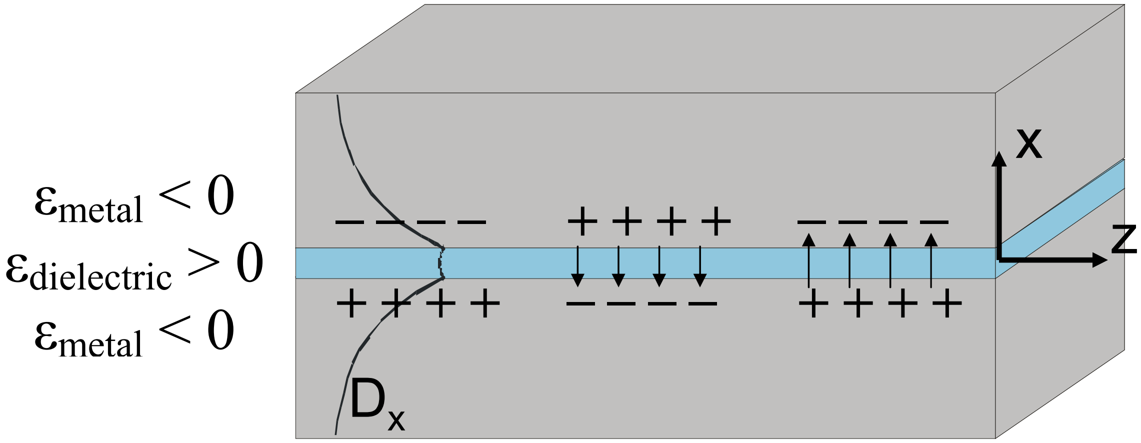

Figure 2-4: Geometry of double sided MIM plasmon

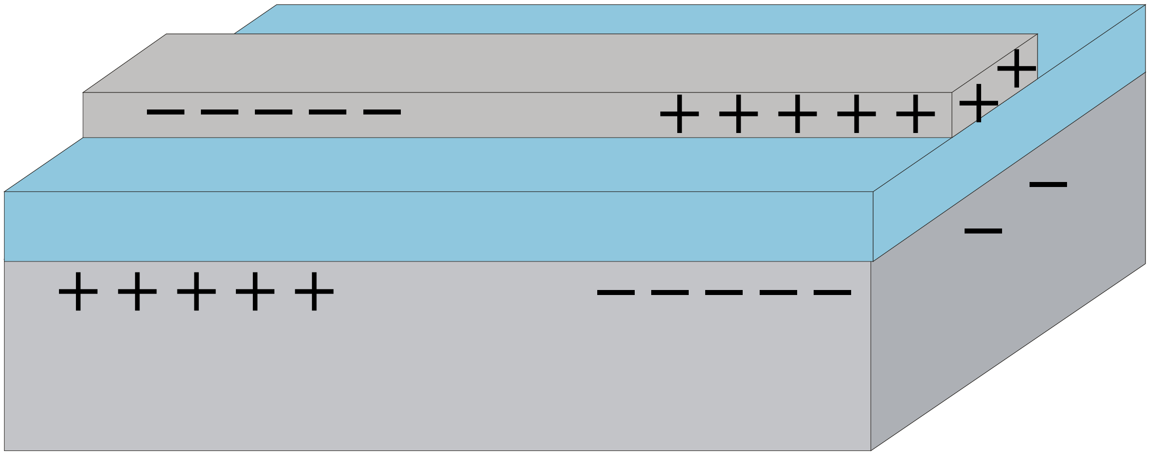

Figure 2-5: Geometry of conventional micro-strip

From a fabrication perspective, the key to this structure is that it relies on conventional planar processing techniques. Leveraging off of the semiconductor processing industry allows for a tunable dielectric thickness down to a single nanometer, as gate oxides thinner than 1.3nm have been report as far back as 1998[65] and 1.1nm oxides are now the standard for the 65nm node of the ITRS Roadmap[66]. The ultimate manufacturing limit to lateral confinement of plasmonic structures is a function of the minimum thickness of the dielectric layer. Fortunately, the modern semiconductor processing industry is built on the construction of repeatable and high quality planar dielectric layers. This is in stark contrast to photo-assisted STM and tapered plasmonic wires described in Chapter 1. Requiring full three-dimensional control of the silver as it tapers down to molecular dimensions, these geometries are prohibitively difficult to fabricate. Although atomically sharp silver STM tips have been developed, they tend to be difficult to reproduce and have an overall shape[67,68,69] which makes them poor for plasmonic focusing.

In regards to nanoscopic fabrication, the Metal-Insulator-Metal structure has a distinct advantage. This is due to the material properties of silver. At ambient temperatures, silver forms a polycrystalline structure. In bulk silver, these grains tend to be on the order of 100nm in diameter. As the silver is made thin, as in the case of an STM tip, these grains will shrink to the radius of the tip, actually changing the nanoscopic shape. This leads to an increased resistivity due to grain and interface boundary scattering. By using the MIM structure and working with thin amorphous dielectrics, we mitigate this additional loss mechanism.

The converse of the MIM structure, the Insulator-Metal-Insulator (IMI) system, provides a particular case in point. This planar structure supports propagating plasmons, however it suffers from diminished grain size when the metal film is made to be thin.

Electrons in a nanometer-scale silver film will suffer from much greater grain-boundary scattering losses than those in thick silver. Thus, the insulator-metal-insulator system is inherently lossier[70]. This problem becomes catastrophic as the film thickness reduces to the scale of monolayers. Electron energy loss spectroscopy experiments[71] have shown that ultra-thin silver films form grains that completely localize the plasmons, not allowing them to propagate at all. In the case of the MIM system, however, the thin insulating layer can be made of an amorphous dielectric. This allows for a much smoother interface and puts no limitations on the size of the silver grains in the metal plates. Furthermore, the MIM geometry is superior in terms of efficiency and greater field confinement[72].

2.3 Dispersion Relations

The dispersion relation for the MIM slab structure contains the important physical pieces required for full three-dimensional optical confinement. The Metal-Insulator-Metal dispersion relations are derived in the literature[13,14,73] using various techniques and levels of complexity. To complete the analysis of our device, a derivation is given below starting with Maxwell's equations. The geometry and coordinate system is shown in Figure 2-6. First we begin with the wave equation of Chapter 1 where ω is the angular frequency of oscillation, c is the speed of light, and ε is the relative dielectric constant of the medium.

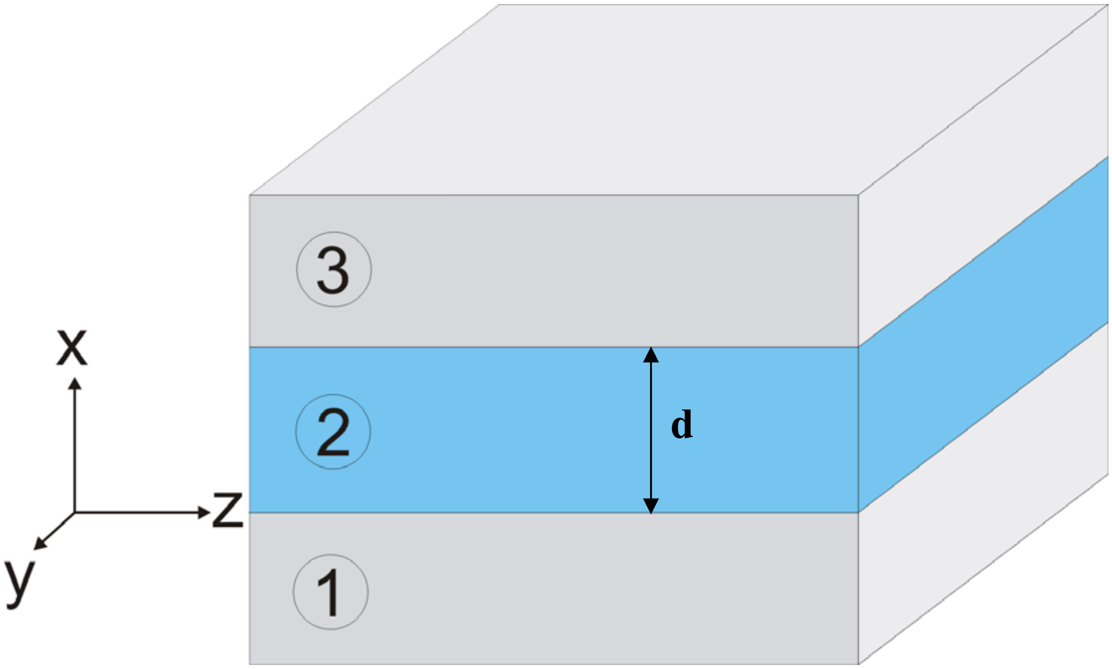

Figure 2-6: Geometry and coordinate system for MIM plasmons

$$-\nabla^2 E = \left(k_x^2 + k_y^2 + k_z^2\right) E = \frac{\varepsilon\omega^2}{c^2} E \qquad (2\text{-}8)$$

This simplification assumes that the field has exponential and sinusoidal variation in the *x* and *z* direction. We also assume and that the fields have no variation in the homogenous *y*-direction. Now, to create modes bound to the surface (i.e. *surface* plasmons) the fields must decay in the direction normal to the surface. Mathematically this means that k_x is imaginary and thus $k_x^2 < 0$. Combined with the wave-equation, then, $k_z^2 > \left|\frac{\varepsilon\omega^2}{c^2}\right|$ in the dielectric and therefore the plasmon wave-vector (k_z) has a larger momentum than the light line. This, too, is a prerequisite for bound modes. In line with the notation of reference[14], we define $k \equiv k_z$ and $K \equiv ik_x = k^2 - \frac{\varepsilon\omega^2}{c^2}$. Note that for a given *k*, *K* will depend on the medium via its dependence on ε. These solutions to the wave-equation tell us that each component of the electric field propagating in the positive z direction must be of the form:

$$f(x,z,t) = C_1 \exp(K_{i.m}x + ikz - i\omega t) + C_2 \exp(-K_{i.m}x + ikz - i\omega t) \quad (2\text{-}9)$$

The terms C_1 and C_2 are constants to be determined for a given geometry, frequency and materials system. The subscripts on K indicate whether they are in the metal (m) or insulator (i). We are now in a position to define the electric field in the x direction (E_x) for regions 1, 2 and 3 of Figure 2-6. In the solution of these equations, we will take the angular frequency (ω) to be positive and real. The terms k and $K_{i,m}$ are complex, however the real part is taken to be positive.

$$E_{1x} = \exp(K_m x + ikz - i\omega t) \quad (2\text{-}10)$$

$$E_{2x} = B_1 \exp(K_i x + ikz - i\omega t) + B_2 \exp(-K_i x + ikz - i\omega t) \quad (2\text{-}11)$$

$$E_{3x} = C \exp(-K_m x + ikz - i\omega t) \quad (2\text{-}12)$$

To generate equations above, terms were dropped which diverge at $x = \pm\infty$. The region of Figure 2-6 for each electric field term E is denoted by the numerical subscript while the second subscript describes the direction of the electric field. Finally, electric field at $x = 0$ in region 1 was normalized to unity. Once E_x has been specified, Gauss's Law now uniquely determines E_z in each region.

$$E_{1z} = \frac{iK_m}{k} \exp(K_m x + ikz - i\omega t) \quad (2\text{-}13)$$

$$E_{2z} = \frac{iK_i}{k} \left[B_1 \exp(K_i x + ikz - i\omega t) - B_2 \exp(-K_i x + ikz - i\omega t) \right] \quad (2\text{-}14)$$

$$E_{3z} = -\frac{iK_m}{k} C \exp(-K_m x + ikz - i\omega t) \tag{2-15}$$

To eliminate the constants B_1, B_2 and C, we now employ the continuity of E_z and D_x at x=0 and x=d.

$$K_i \left(B_1 - B_2\right) = K_m \tag{2-16}$$

$$\varepsilon_i \left(B_1 + B_2\right) = \varepsilon_m \tag{2-17}$$

$$\varepsilon_m C \exp(-K_m d) = \varepsilon_i \left[B_1 \exp(K_i d) + B_2 \exp(-K_i d)\right] \tag{2-18}$$

$$-K_m C \exp(-K_m d) = K_i \left[B_1 \exp(K_i d) - B_2 \exp(-K_i d)\right] \tag{2-19}$$

This generates a system of four equations and four unknowns (B_1, B_2, C and k). Simple algebra may then be used to generate the final dispersion relation. Here we are interested in the mode in which the induced charges are anti-symmetric with respect to spatial inversion about a plane through the center of the device (i.e., the plane which lies in the center of region 2). A second mode exists in which the charge is symmetric with respect to this inversion, but this mode cannot achieve large wave-vectors and therefore is of no relevance to this dissertation. Putting everything together, we arrive at

$$e^{-K_i d} = \frac{\varepsilon_m K_i + \varepsilon_i K_m}{\varepsilon_m K_i - \varepsilon_i K_m} \tag{2-20}$$

Equation (2-20) may then be solved by various methods. For this work, numerical techniques were employed using Mathematica 5.0.0.0. The first step in the solution was to recast Equation (2-20) as

$$\left|\varepsilon_m K_i + \varepsilon_i K_m - e^{-K_i d}\left(\varepsilon_m K_i - \varepsilon_i K_m\right)\right| = 0 \tag{2-21}$$

The left-hand side of Equation (2-21) is real and non-negative. For a fixed frequency, K_i and K_m are defined by the real and imaginary components of k through $K_{i,m} \equiv k^2 - \frac{\varepsilon_{i,m}\omega^2}{c^2}$. With a real and fixed ω, a minimization routine was then run on the left hand side of Equation (2-21) to separately vary both components of the complex k. A local minimum in the right hand side of Equation (2-21) could easily be rejected by discarding any answers greater than 10^{-6}. To rapidly arrive at the global minimum, various techniques were used to determine appropriate starting values for the components of k in Mathematica's 'FindMinimum' routine. For instance, the imaginary component of ε_m tends to only be a small perturbation to the dispersion relation. It can, therefore, be discarded and the minimization routine is then run over only the real part of the wave-vector. This rapidly converges to a global minimum and yields an excellent starting point for the minimization over the complex dielectric constants ε_m. It is noted that there are more mathematically interesting methods of solving the dispersion relations[74,75], however our simple numerical minimization routine for solving k at fixed ω will be crucial when determining higher order perturbations and loss mechanisms in later chapters.

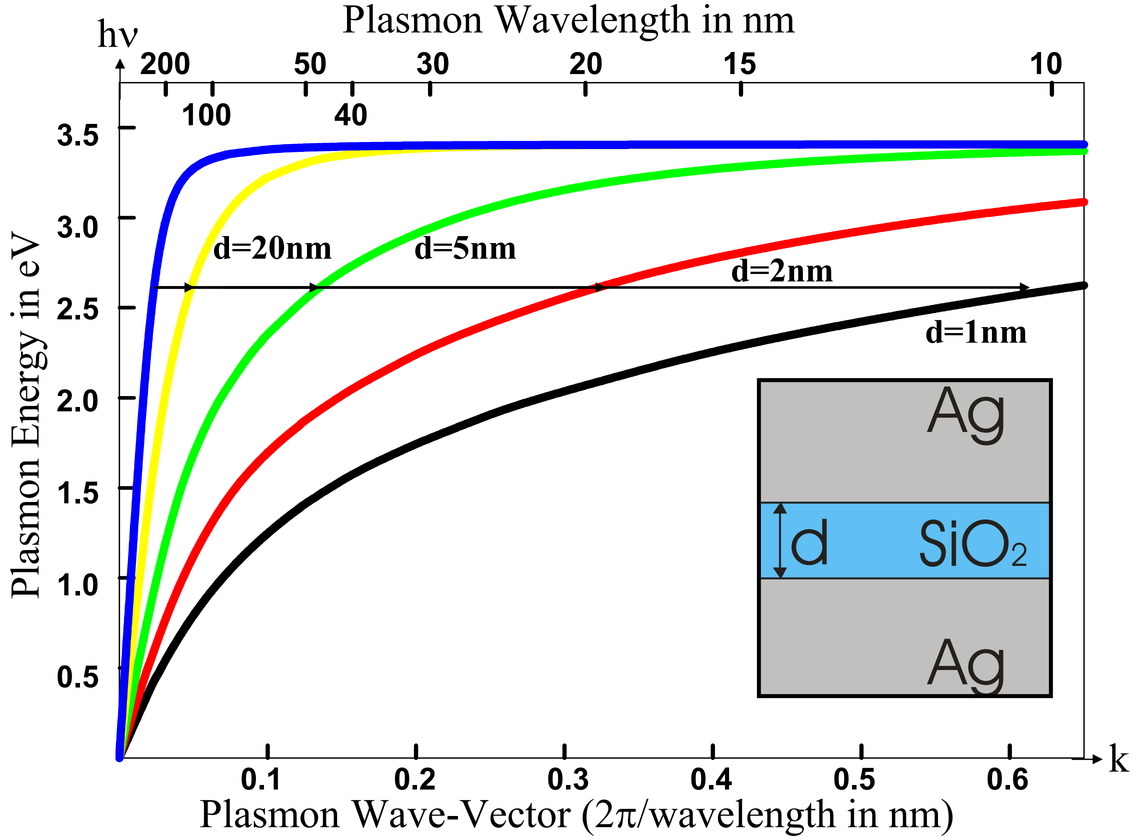

Figure 2-7: Dispersion relations of Ag-SiO_2-Ag plasmons of various oxide thicknesses

The dispersion relations for the Ag-SiO_2-Ag double sided plasmon are plotted in Figure 2-7. This plot shows the plasmon (or photon) energy on the ordinate axis in electron Volts, derived from Planck's constant times the frequency. The abscissa enumerates the real component of the plasmonic wave-vector in units of 1/nm. Note that the dispersion relation is entirely dependent on the thickness of the dielectric, with the lowest wave-vector curve (shown in blue) indicating an infinitely thick dielectric. Thinner SiO_2 layers have large wave-vectors at any given frequency. This suggests that by tapering the thickness of the SiO_2 layer, the wave-vector can be made very large. In fact, by tapering to 1nm and using 476nm free space photons, *X*-ray wavelengths may be achieved in the plasmon!

While the large wave-vectors of surface plasmons are very promising, the propagation lengths are not. Calculated as the 1/*e* propagation length of the plasmonic energy due strictly to dissipation in the silver, the losses are shown in Figure 2-8. Note that most plasmons in this anti-symmetric mode have propagation lengths less than 500nm. As we shall demonstrate in the next chapter, this problem may be surmounted by rapidly tapering to the very thin oxide. For most applications, there is no need to propagate the nano-focused mode over long distances. Instead, the significant figure of merit is the efficiency of energy delivery in focusing to the nanoscale. There is still plenty of room within the slab mode plasmon properties to achieve greater than 50% coupling efficiency.

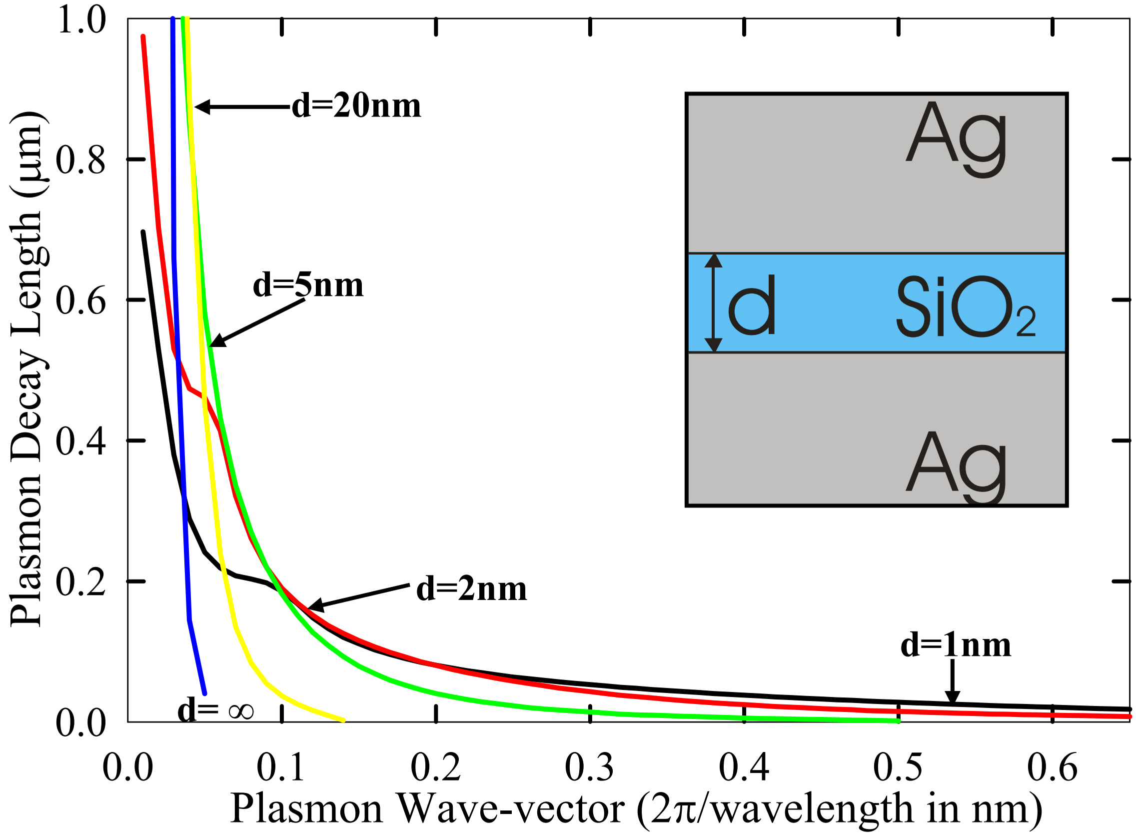

Figure 2-8: Plasmonic decay length versus wave-vector at various oxide thicknesses

2.4 Three-Dimensional Confinement in a Slab Geometry

Although the MIM structure is plainly 1 dimensional, this geometry can achieve full three dimensional focusing down to nanoscale dimensions. This is attained via three properties of the double sided surface plasmons evident in Figure 2-7. Departing from the light-line, the dispersion relation has a knee as the *k*-vector becomes very large for moderate photon energies. In fact, the plasmon wavelengths become so small that they enter the *X*-ray wavelength regime but with optical frequencies. Such small wavelengths allow us to create a nanoscopic line image in our slab geometry using conventional focusing techniques. The limitations on the spot size of a line image are much looser than that of a two-dimensional image[76] and are limited to the plasmon wavelength (λ_p) divided by two. The key is that the limitations of the free space photon wavelength are now replaced by the extraordinarily short plasmon wavelength.

The slab mode also achieves confinement in the longitudinal dimension. The optical energy density is enhanced along the direction of propagation by the reduced group velocity. The slope of the dispersion relation, equal to the group velocity, decreases as the wave-vector becomes very large. From simple energy conservation considerations, this causes the field to compress along the direction of propagation.

Finally, there is compression of the field in the transverse direction. This we will call the 'skin depth', and represents the rapid exponential decay of the field into the metal. This effect is most prominent at large wave-vectors. The simple wave equation, as shown in Equation (2-8), dictates why the skin depth must become very small. At large wave-vectors, the term representing the light line is negligible and $K \approx k$. Because the term K is the rate of exponential decay into the medium, the skin depth is then $1/K$. under the large-k approximation, this is equal to the plasmon wavelength (λ_p) divided by 2π and is therefore forced to become very small as the k vector becomes very large.

At this point we must digress to address the issue of the classical skin depth (or penetration depth[55]) in high frequency electronics. The nomenclature tends to be a point of confusion and so will be discussed here explicitly. The result can be derived several ways and here we use the scheme illustrated by Figure 2-9. As shown in the figure, radiation is impinging normally onto a metallic half-space. The solutions of Maxwell's equation dictate that the metal will setup charges and currents to cancel the field. At high frequencies, however, the conductivity is finite and the field has some penetration into the metal.

This exponential decay of the field normal to the interface has a decay length equal to[77]

$$\delta = \frac{\lambda_0}{2\pi\left|\sqrt{-\varepsilon_m}\right|} \tag{2-22}$$

In Equation (2-22), λ_0 is the free space radiation wavelength and ε_m represents the relative dielectric constant of the metal. At RF and Microwave frequencies, this term tends to be dominated by its imaginary component and δ is known as the collisional skin depth. At optical frequencies, however, ε_m is dominated by its real part and δ is called the collisionless skin depth. A cursory examination of Equation (2-22) for a visible photon impinging on silver yields a penetration depth of approximately 25nm. This, however, has no relevance to the limitations of the skin depth for surface plasmons. As this calculation assumed zero momentum along any direction tangential to the interface, this has little bearing on the plasmonic case of exceedingly high momentum in the plane of the interface.

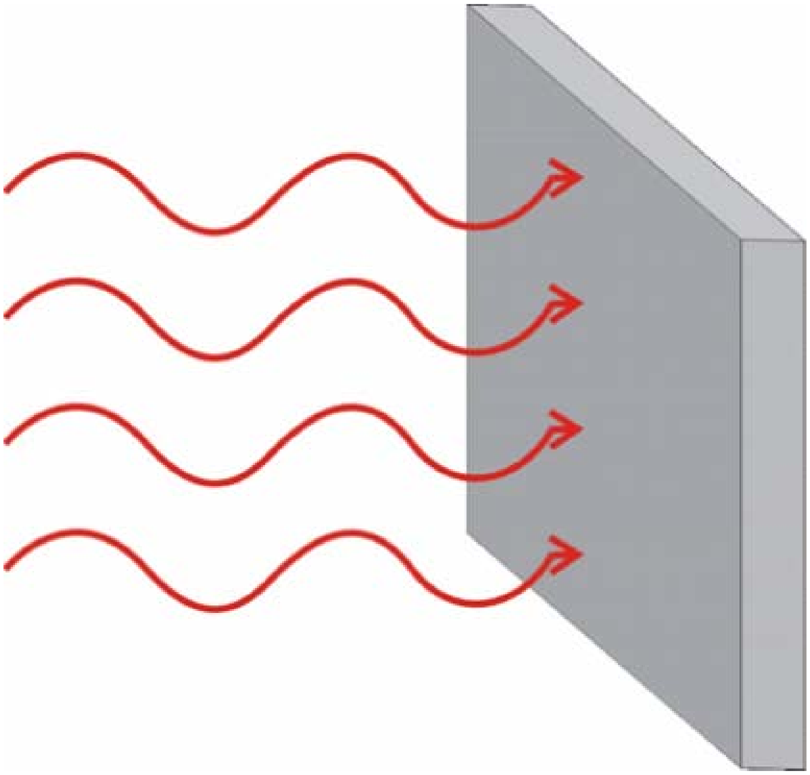

Figure 2-9: Scheme for generation of the classical skin depth

2.5 Plasmon Properties at Large Wave-Vector

Surface plasmons can be focused to the nanoscale because of they can achieve very large wave-vectors. It is essential, then, to analyze the dispersion relations in this high-impact regime. We begin again with the full dispersion relation for the MIM geometry.

$$e^{-K_i d} = \frac{\varepsilon_m K_i + \varepsilon_i K_m}{\varepsilon_m K_i - \varepsilon_i K_m} \qquad (2\text{-}23)$$

$$K_{i,m}^2 \equiv k^2 - \frac{\varepsilon_{i,m}\omega^2}{c^2} \qquad (2\text{-}24)$$

As k becomes very large, Equation (2-24) simplifies considerably and $K_{i,m} \approx k$. After cancellations, this reduces Equation (2-23) to:

$$e^{-kd} = \frac{\varepsilon_m + \varepsilon_i}{\varepsilon_m - \varepsilon_i} \tag{2-25}$$

It must be noted that the losses already become prohibitively large before we enter the sub-nanometer regime where quantum mechanical calculations would become necessary. Selvedge effects, which account for the charge discontinuity at the metal-insulator interface, have been ignored, however the losses due to electron transport effects will be discussed at length in Chapter 5.

Emphasis must be given to our fortuitous length scale regime. Lengths on the order of tens of nanometers would require the more complicated retarded plasmon dispersion relation of Equation (2-23). The description of sub-nanometer plasmon wavelengths, on the other hand, would demand complicated quantum mechanical calculations which rely heavily on models and detailed knowledge of the surface properties. Between these extremes lies the elegant simplification shown in Equation (2-25)

Once the material properties are mapped out and the dispersion relation is cast in the simple form of Equation (2-25), the design parameters begin to present themselves. This stems from the fact that the plasmon properties become linear functions of the dielectric film thickness (d) in the high-k limit. Inspection of Equation (2-25) tells us that choosing the optical excitation frequency (laser line, arc-lamp, etc) fixes the right hand side via the frequency dependence of the dielectric constants. This allows Equation (2-25) to be recast as

$$k\,d = f(\omega) \tag{2-26}$$

where $f(\omega)$ is some scalar function of frequency. The significance of this equation is liable to be lost in its simplicity. It is telling us that all of the important design parameters of the surface plasmons in the MIM structure become simple functions of the gap thickness (*d*) in the high-*k* limit. Clearly, the real and imaginary components of the *k*-vector grow inversely with *d*. The constant of proportionality (*f*) for the real and imaginary parts of $k\ d$ are given in Figure 2-10 and Figure 2-11 respectively. This illustrates that the plasmon wavelength is directly proportional to the film thickness. As the film grows thinner, the plasmon wavelength and decay length both decrease linearly with *d*. In this large *k*-approximation, the ratio of the real to imaginary components of *k* is therefore fixed and independent of thickness. This implies that loss per plasmon wavelength is a function of frequency and materials only, and this constant of proportionality is plotted in Figure 2-12. Note that the imaginary component of the wave-vector is much smaller than the real component across the frequency band of interest, justifying the use of Equation (2-1)

The form of Equation (2-25) also allows for a simple formulation of the group velocity. Taking the differential of both sides of Equation (2-25) with respect to ω, we arrive at the group velocity. A bit of manipulation yields

$$\mathrm{v}_g = d\,\omega M \tag{2-27}$$

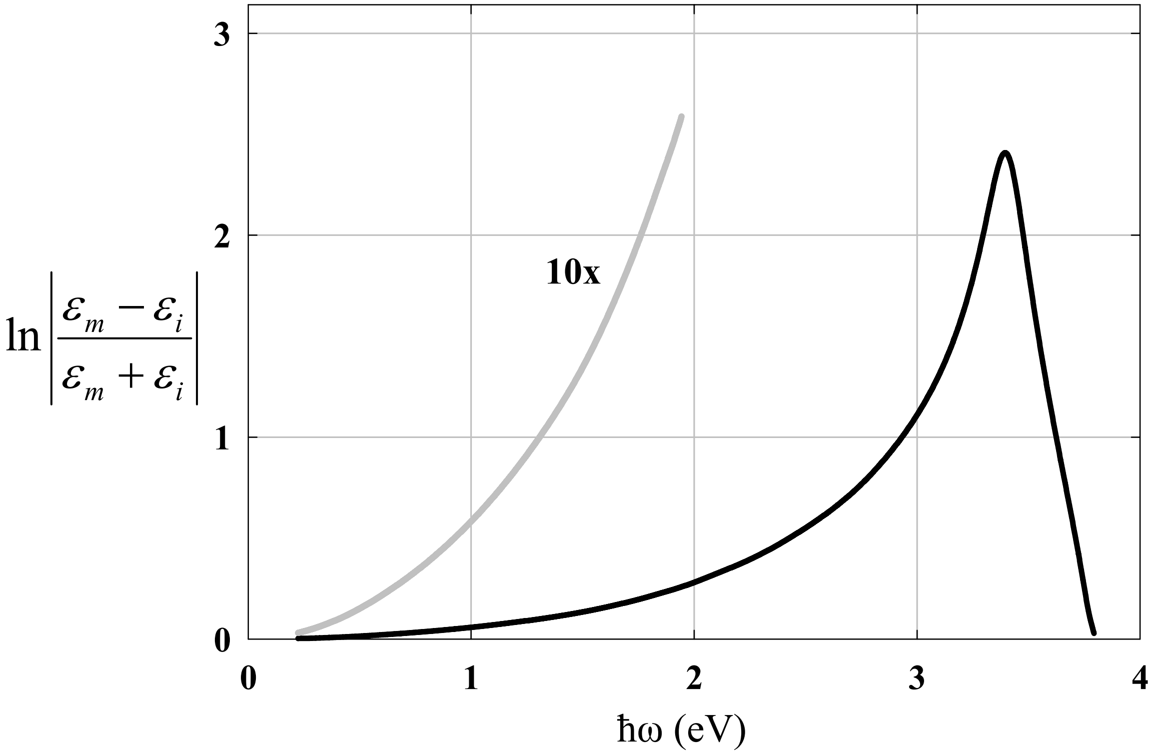

Figure 2-10: Relation for the real part of *kd* for Ag-SiO$_2$-Ag in the high-*k* limit

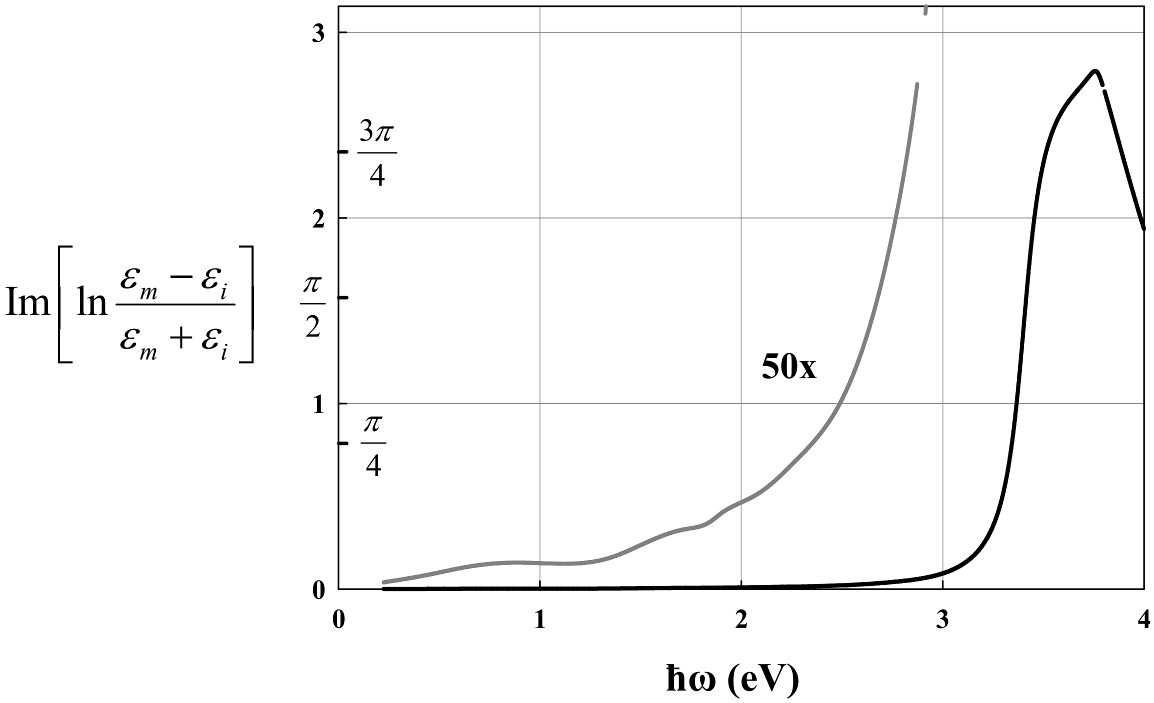

Figure 2-11: Relation for the imaginary part of *kd* for Ag-SiO$_2$-Ag in the high-*k* limit

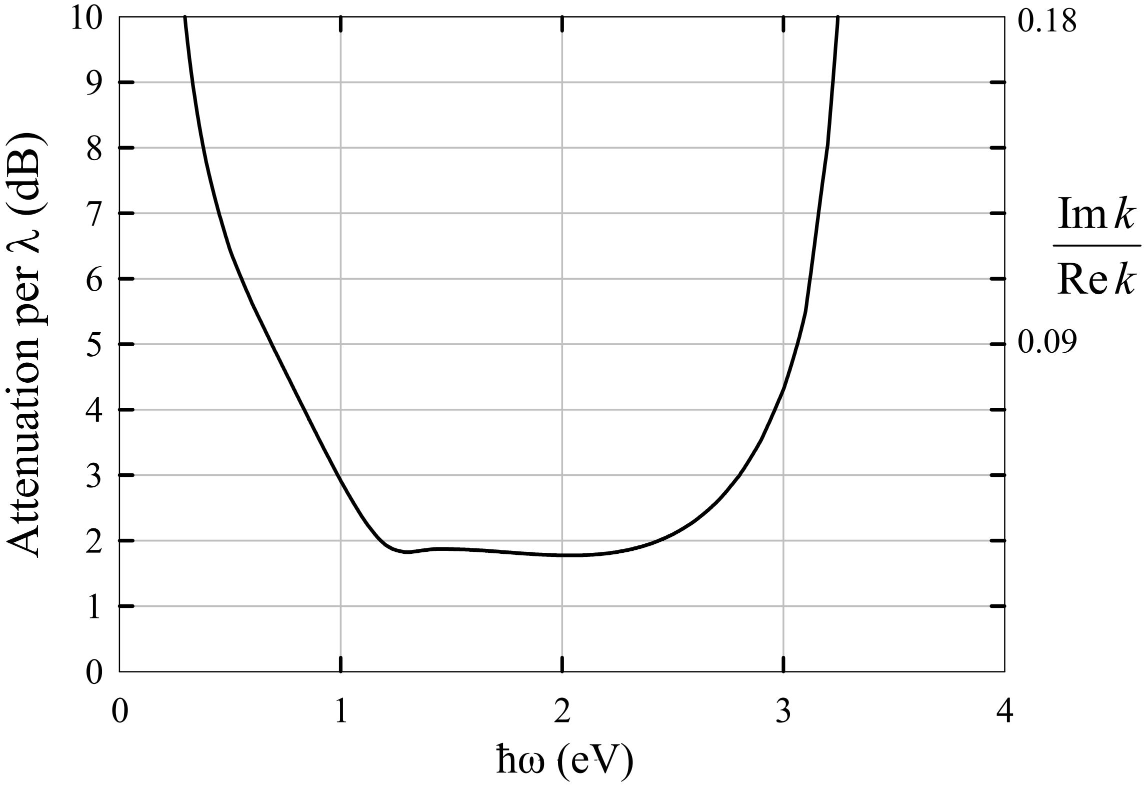

Figure 2-12: Attenuation per plasmon wavelength at large wave-vector

The quantity *M* in Equation (2-27) is dimensionless and is defined below

$$M \equiv \mathrm{Re}\left[\frac{(\varepsilon_m+\varepsilon_i)(\varepsilon_m-\varepsilon_i)}{2\varepsilon_i\left(\partial(\omega\varepsilon_m)/\partial\omega-\varepsilon_m\right)}\right] \tag{2-28}$$

A plot of *M* for the Ag-SiO$_2$-Ag geometry is shown in Figure 2-13 as a function of frequency. Like the other plasmon properties discussed above, the group velocity is simply a linear function the dielectric thickness for large *k*.

As was discussed in Section 2.3, the three-dimensions of optical confinement are achieved by tapering the oxide thickness in the double-sided MIM plasmon. This occurs through a reduction in group velocity, reduction in the plasmonic skin depth, and the reduction in plasmonic wavelength. At high wave-vector, we clearly see that these effects all scale *linearly* with the dielectric thickness. Equation (2-26) demonstrates that $\lambda \sim \frac{1}{\mathrm{Re}\{k\}} \sim d$. Of course, since $K \approx \mathrm{Re}\{k\}$ in this regime, the skin depth also must scale linearly with *d*. Therefore, a taper in a MIM plasmonic waveguide will yield an energy density enhancement of $\left(d_{initial} / d_{final}\right)^3$ when losses are neglected and at large wave-vector.

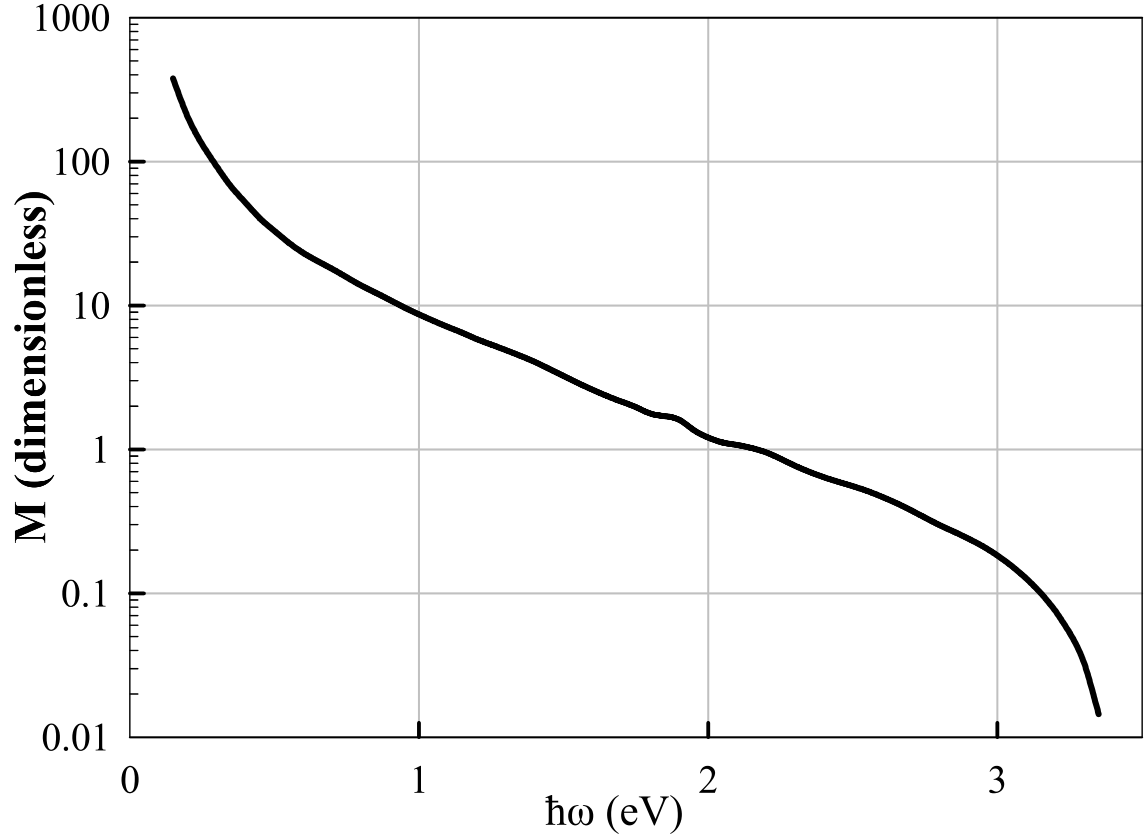

Figure 2-13: Dimensionless quantity M versus optical energy

With these pieces in place, significant conclusions immediately become apparent. We start with the definition of modal $Q \equiv Q_{mod}$

$$Q_{\mathrm{mod}} \equiv \frac{\omega U}{dU/dt} = \frac{\omega U}{\frac{dU}{dx}\frac{dx}{dt}} \tag{2-29}$$

The term ω is the input frequency. We now define a decay length (Λ) which represents the propagation length over which the energy decays by e^{-1}. This allows us to recast $\frac{dU}{dx}$ as $\frac{U}{\Lambda}$. The term $\frac{dx}{dt}$ represents the velocity at which energy propagates down the channel, which is very definition of the group velocity v_g. Putting this all together and manipulating yields

$$\mathrm{v}_g \frac{Q_{\mathrm{mod}}}{\omega} = \Lambda = \frac{1}{2k_{im}} \tag{2-30}$$

The second equality comes about because the power decay length must be equal to $\frac{1}{2k_{im}}$ by the assumptions given in Equation (2-9). As shown above, both v_g and $1/k_{im}$ are linear functions of thickness in the high-k regime. This implies that the modal Q must be independent of film thickness. It must be a function only of material parameters and input frequency.

With the development of one more piece, the expression for modal Q may be greatly simplified. We need to find a simple expression for the decay length. Starting with Equation (2-25), we know that k_{im} is given by

$$k_{im} = \frac{1}{d}\operatorname{Im}\left[\ln\left[\frac{\varepsilon_m - \varepsilon_i}{\varepsilon_m + \varepsilon_i}\right]\right] \tag{2-31}$$

Taking the imaginary part of a natural log amounts to finding the phase of the complex quantity inside the brackets. We have defined the insulator as being lossless, and thus having only a real dielectric constant. The expression for k_{im} may be reduced to

$$k_{im} = \frac{1}{d}\arctan\frac{2\varepsilon''_m\varepsilon_i}{\left(\varepsilon'_m - \varepsilon_i\right)\left(\varepsilon'_m + \varepsilon_i\right)} \tag{2-32}$$

Finally we make the approximation that arctan $\theta \approx \theta$, which is true in the case such that the plasmonic loss is low enough to make Equation (2-3) applicable.

$$k_{im} = \frac{1}{d}\frac{2\varepsilon''_m\varepsilon_i}{\left(\varepsilon'_m - \varepsilon_i\right)\left(\varepsilon'_m + \varepsilon_i\right)} \tag{2-33}$$

We may now recast Equation (2-30) by substituting the expressions found in Equations (2-27), (2-28) and (2-33). With some simple manipulation and cancellation, this yields

$$Q_{\text{mod}} = \frac{\dfrac{d\left(\omega\varepsilon'_m\right)}{d\omega}}{2\varepsilon''_m} - \frac{\varepsilon'_m}{2\varepsilon''} \tag{2-34}$$

Again, the real and imaginary parts of the dielectric constant of the metal are represented by the primed and double primed quantities, respectively. Like the loss per wavelength, the modal *Q* is a constant at large wave-vectors. Note also that although many propagation parameters depend very strongly on the dielectric constant of the insulator and its thickness, the modal *Q* has no dependence on either of these terms. This remarkable result, plotted in Figure 2-14, result underscores the critical importance of the conductor and frequencies used in plasmonic focusing devices. This is illuminated by analyzing the terms in Equation (2-34). The first term is simply Q_{mat} as given by Equation (2-5) and takes dispersion into account. The second term is equivalent to the first in the case of a non-dispersive medium. Both terms are of the same order of magnitude, which explains why Q_{mod} is approximately twice Q_{mat}.

One can arrive at Equation (2-34) by another method. Starting with the explicit definition of modal Q given in Equation (2-3) and again assuming that the H field contains no energy in the high-k limit, we may solve for Q_{mod}. Because the dispersion relations tell us the exact form of the electric field, it is feasible to carry out the spatial integrations of both E_x and E_z. After a good deal of algebra, manipulation and substitutions, we arrive at the same simple formula given above. Both of these methods converge to the same result, even though the second method makes the explicit assumption that the magnetic energy is zero, while the first makes no such restrictions. The simple frequency dependence implies that the spatial mode profile merely changes its geometric scale linearly with dielectric thickness. Analytical solutions as well as simulations bear this conclusion out. It tells us that in the high wave-vector regime, changing the thickness of the dielectric simply scales the transverse plasmon mode profile.

The reader should note that Figure 2-14 is very similar to the plot of the material Q of silver, which is illustrated in Figure 2-1 and in greater detail in Figure A-1. This demonstrates the significance of material Q in determining the modal properties. It is important for the reader to note that although this shows a maximum Q_{mod} of ~45, much higher modal Q may be achieved at low wave-vectors where Equation (2-34) does not apply and most of the energy is in the dielectric.

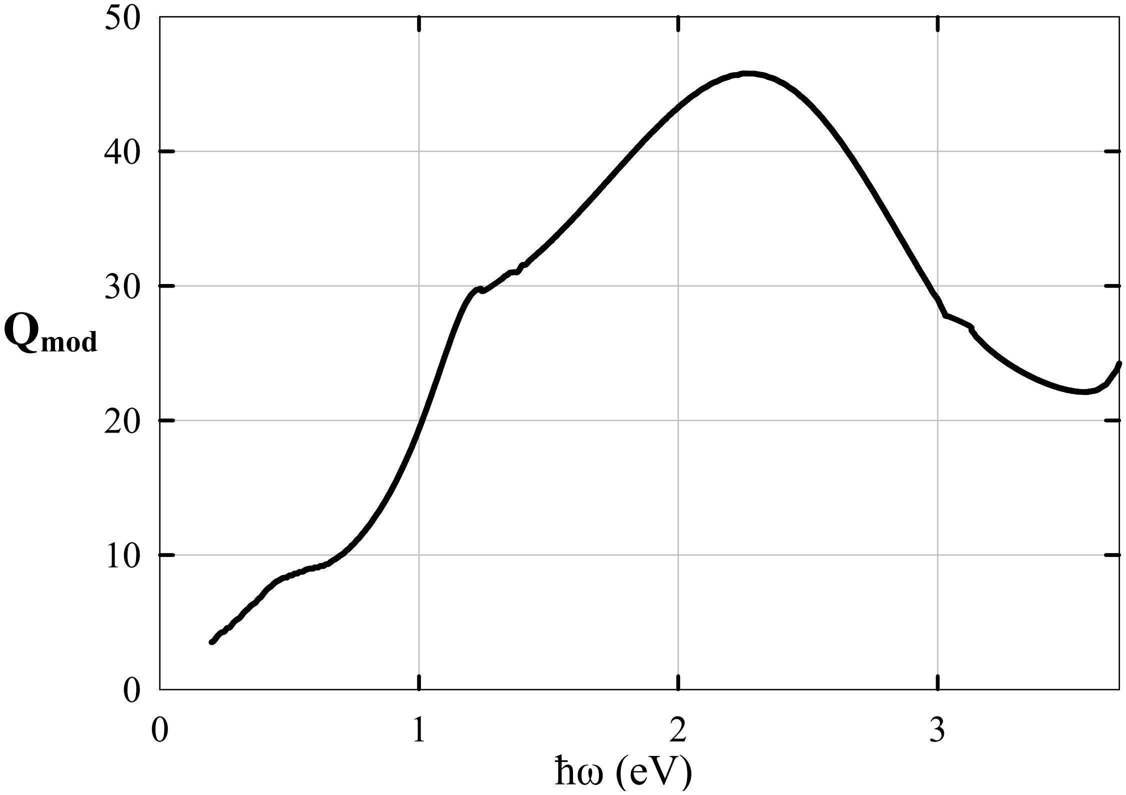

Figure 2-14: Modal Q_{mod} as a function of frequency

2.6 The Ideal Taper at Large Wave-Vectors

Surface plasmons have the remarkable capacity to confine visible photons to dimensions on the order of nanometers. As is evident in Figure 2-8 and Figure 2-15, surface plasmons can be intolerably lossy, particularly at very large wave-vectors and for thin insulators. Note that the plasmon energy propagates less than 1μm for oxides less than 10nm thick. This is an exceedingly short length. The propagation characteristics are much more favorable near the light-line, where the group velocity is large, thereby reducing the interaction per unit length of the field energy with the intrinsic loss mechanisms of the metal. Ideally, then, the most efficient focusing structure would begin with a thick, low-loss plasmon wave-guide. The next step would be a coupler between a thick plasmon channel and a very thin channel. The design of this coupler for minimum absorption or scattering is pivotal for efficient coupling to the nanoscale.

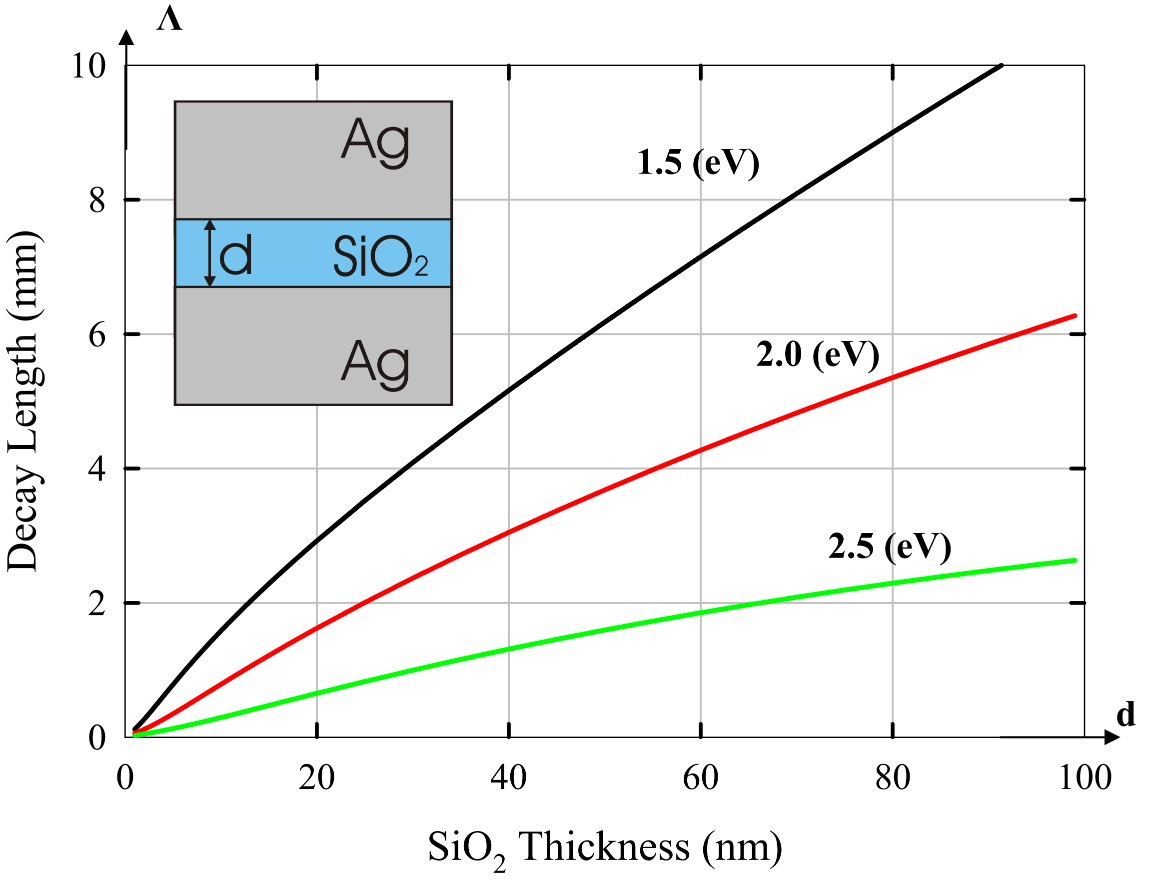

Figure 2-15: Plasmon decay length versus oxide thickness at constant photon energies for the Ag-SiO_2-Ag slab geometry

The remarkable analytical simplifications of Section 2.5 provide intuition on how to create this nano-coupler and focus the field in the MIM (micro-strip) geometry. For clarity, the problem is treated two-dimensionally. We envision a taper, of some profile to be determined, which begins in a thick, low-loss slab channel and terminates in a slab geometry with a very thin insulator. Minimizing the absorption losses must be the first consideration. To that end, the region of high *k*-vector and tight focusing must be kept as short as possible because it is also the region of the greatest attenuation. This means a minimized length of the thinnest portion of the dielectric.

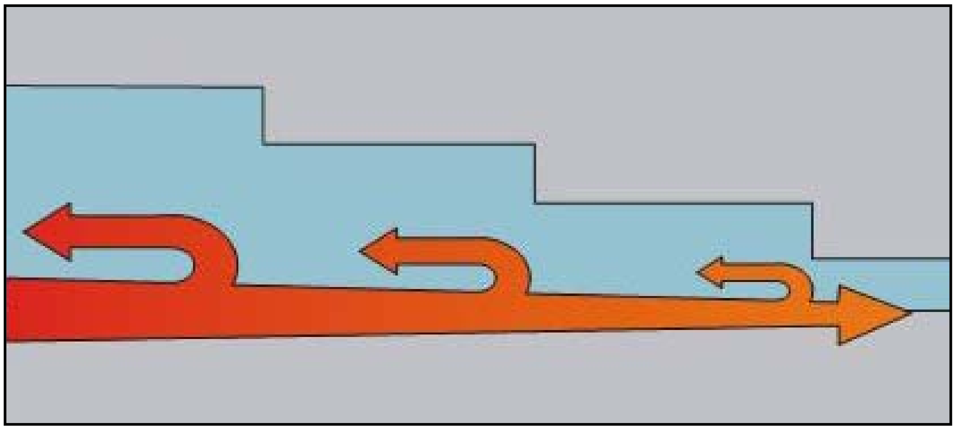

Figure 2-16: Illustration of the scattering losses from a non-adiabatic taper

Maximizing power throughput also means an efficient transition between the low loss, thick part of the device, and the thin focal region. One imagines some arbitrary transition profile of the dielectric to achieve this. From the adiabatic criterion, scattering can be neglected if δλ/λ << 1. This suggests a gradual taper. The design space is constrained on the other side by dissipation effects, which demand a rapid transition. At this point, the simple dependence of the plasmon parameters on *d* with large wave-vector gives us a solid foundation for designing this taper. We know that the loss/λ is fixed with a given frequency. The adiabatic criterion tells us scattering losses are governed by δλ/λ.

Therefore, a value of δλ/λ which is constant across the taper will give us a constant value of scattering losses per plasmon wavelength. It is then logical that the profile with balance between a constant scattering loss per wavelength and a constant absorption loss per wavelength will yield the best throughput.

Determining the spatial profile of the oxide thickness now hangs on determining the functions which yield a constant δλ/λ. This is a simple exercise because of the discussion above. We know that

$$d = f\left[\omega\right]\lambda \tag{2-35}$$

where $f\left[\omega\right]$ is a scalar function of frequency and λ is the plasmon wavelength. Taking the differential and writing *d* as thickness for clarity we have

$$\frac{d(thickness)}{dz} = f\left[\omega\right]\frac{d\lambda}{dz} \tag{2-36}$$

If we then set $dz = \lambda$, we arrive at a simple proof that the adiabatic criterion is constant for a linear taper. This design will then allow us to equalize the scattering losses along the length of the taper, preventing excessive losses at any one point and creating a constant transition. To the first order, then, a linear taper is the best transition to the nanoscale. These fundamental design principles present themselves thanks to the simplicity of Equation (2-25).

This chapter has laid the foundations for the design of an optimized plasmonic focusing structure. It has suggested a suitable geometry for confining visible photons to dimensions less than 10nm. The numerical details of the device, however, cannot be described through analysis alone and must be determined through computational simulations. The following chapter outlines the computational details of the design of the plasmonic lens and its overall system specifications.

CHAPTER 3 DESIGN AND SIMULATION

Part of the inhumanity of the computer is that, once it is competently programmed and working smoothly, it is completely honest.

-Isaac Asimov

This chapter begins with the basic design of a linear taper in a two-dimensional slab geometry. Numerical techniques are then employed to optimize the throughput of this structure, accounting for both absorption and scattering losses. These results are then generalized to a three-dimensional focusing structure. The overall throughput and electric field enhancements are then calculated, as well as the final focal spot of the plasmonic lens.

3.1 Numerical Methods

From the analysis developed in Chapter 2, a linear taper is the best trade between scattering losses and resistive losses in the metal. While the analysis of Chapter 2 is useful in forming a theoretical framework, this does little to actually determine the details of an optimized transition to the nanoscale. Based on the discussion at the end of the previous chapter, we restrict our attention to a linear taper. To accurately determine the optimum slope and its throughput, we need some way of estimating the back-scattering as a function of slope as well as the absorption in a non-uniform slab geometry. In the case of an adiabatic taper or quasi-adiabatic taper, many mathematical tools exist[78,79]. The changes in thickness and wavelength are then small compared to the wavelength of the plasmon, and the linear taper can be treated as a series of small, coherently summed perturbations. Back-scattering may be accounted for by employing perturbation theory and the implementation of overlap integrals between the forward propagating and backward propagating waves as the thickness slowly changes. Large scale numerical simulations have established the accuracy of this method[80]. The resistive losses, too, may be determined by numerically integrating the instantaneous losses over the course of the taper.

Instead of treating the linear taper as a perturbation to the slab geometry, a more exact treatment can analytically solve for the modes in a wedge geometry[81,82]. These modes reduce to simple analytic expression and better represent the evolution of power across the taper. They will also more accurately represent the absorption losses, as the wedge mode has a different shape than the perturbed slab mode.

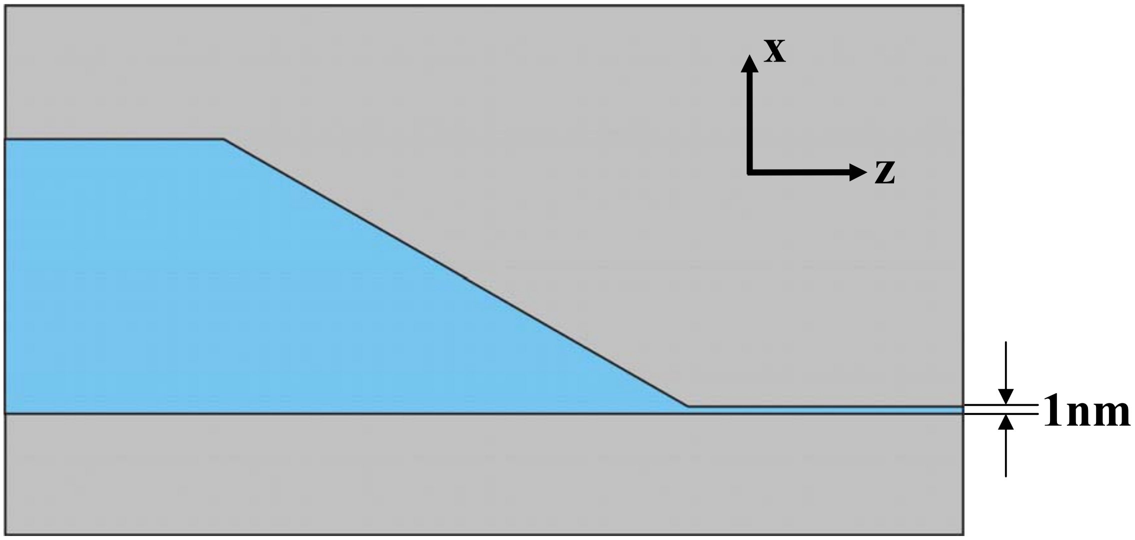

Figure 3-1: Geometry of the linear taper to be optimized

The problem, however, comes at the interfaces of the straight channel with the wedge mode. For adiabatic tapers of small opening angle, perturbation theory may be applied. For sharp bends and rapid transitions, though, the modes in each section interact with each other, form resonances, and are strictly non-adiabatic. This case does not lend itself to the mathematical simplicity of perturbation theory. Solving for the relevant parameters of the taper, then, necessitates a full electromagnetic simulation. To this end, a two-dimensional finite-difference time-domain (FDTD) code was written in C to determine the temporal evolution of a known input field across the device. An example of this code is given in Appendix B. There are many excellent references available on FDTD simulations[83,84], so only a brief overview is given here. The technique begins with a basic staggered, or ‘leap-frog’ meshing[85]. Because the surface plasmons are TM modes, this yields a two-dimensional matrix as shown in Figure 3-2. Every *H*-field component is spatially surrounded by four *E*-field components. Maxwell’s curl equations are then solved in time, again using a leap-frog technique.

$$\frac{\partial E}{\partial t} = \frac{1}{\varepsilon} \nabla \times H \tag{3-1}$$

$$\frac{\partial H}{\partial t} = -\mu \, \nabla \times E \tag{3-2}$$

This means that in the equations above, first Equation (3-1) is solved for *E* using *H* as a source. Time is then incremented one-half step, and Equation (3-2) is solved for *H* using *E* as a source. The technique then continues as such.

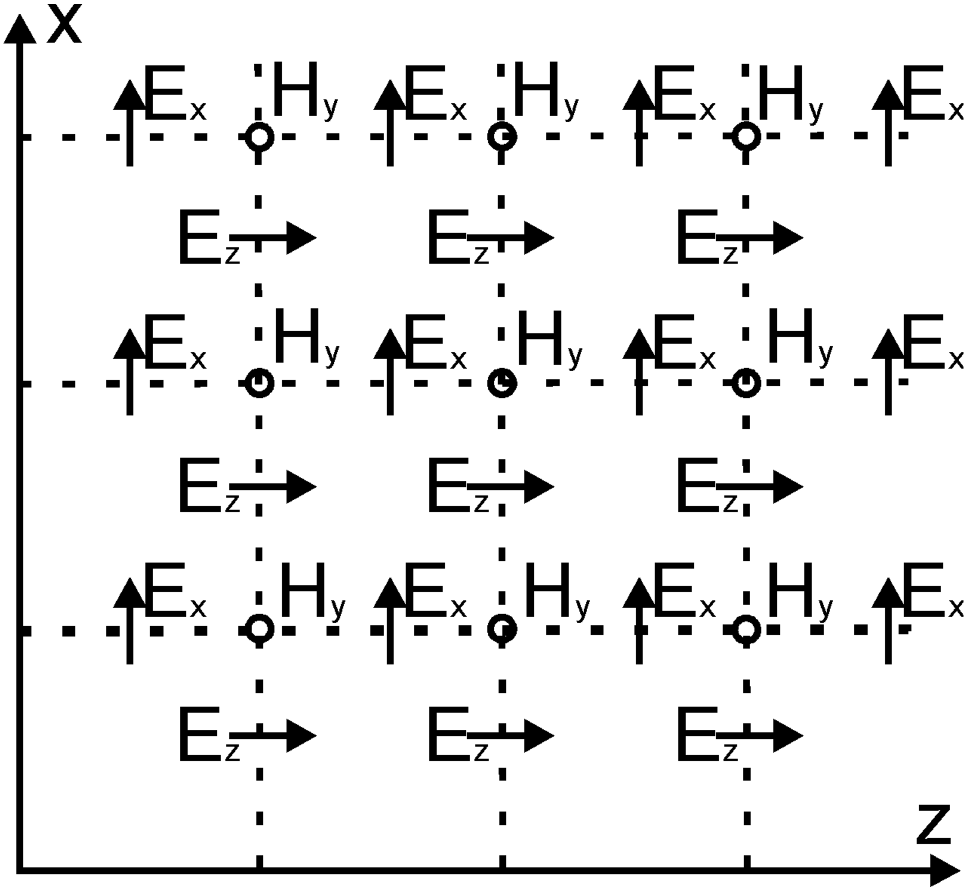

Figure 3-2: Spatial mesh for FDTD of TM plasmon modes

While such an FDTD algorithm was successfully implemented to model surface plasmons in our slab geometry employing Perfectly Matched Layer boundary conditions, the taper demands a certain subtlety. Because the wavelength is rapidly changing, the length scales of the mesh must likewise be changed. Accurate computation requires approximately 10 mesh points every wavelength. The wavelength is a dynamic and rapidly changing quantity, therefore efficient meshing requires an adaptive grid which changes with the taper geometry. The process of redefining the grid with every change in geometry becomes incredibly time consuming and computationally inefficient.

To efficiently converge to solutions as the taper slope was changed, Finite Element software known as FEMLab was used. This software allowed for a graphical interface for local mesh control and rapid display of results for various relevant electromagnetic quantities. Finite Element methods, however, do not operate in the time domain. To solve for the TM plasmons of interest, we used the In-Plane TM Wave application mode, which solved the Helmholtz Equation shown below

$$\nabla \times \left(\varepsilon_r^{-1} \nabla \times H \right) - k_0^2 \mu_r H = 0 \tag{3-3}$$

The quantities ε_r and μ_r are the relative permittivity and permeability respectively, and k_0 represents the free space scalar wave-vector equal to ω/c. This application mode operates only in the frequency domain. As has been emphasized throughout this text, the dispersive properties of the silver are crucial to the plasmon propagation characteristics. Nonetheless the results reported in this chapter were achieved strictly with monochromatic inputs.

3.2 Numerical Results for the Optimum Linear Taper

With these numerical methods in hand, we now return to the problem of taper optimization. We began with a basic geometry: a 50nm thick slab channel leading into a linear taper, terminating at 1nm thick straight channel as shown in Figure 3-3. These thicknesses were not chosen arbitrarily. The final SiO_2 thickness was chosen to be 1nm because gate oxides of this thickness are now repeatably fabricated for the semiconductor industry. Such an oxide yields a transverse mode size of only 2.6nm with 476nm photons (measured at $1/e$ of intensity). The thickness of the input side was chosen as 50nm because such plasmons lie close to the light line, and therefore have manageable losses. As in all of the calculations in this chapter, the input free-space optical wavelength was chosen to be 476nm, corresponding to a photon energy of 2.6eV.

The computational boundaries of this two-dimensional geometry were surrounded by absorbing Perfectly Matched Layers (PMLs). These layers absorb incoming energy without reflection by increasing the imaginary component of μ_r at the same rate as the imaginary component of ε_r. This serves to absorb energy without changing the impedance, thereby minimizing reflections at the boundary. Optimal results were obtained by increasing these imaginary components at a rate which increased with the cube of distance. The electromagnetic input was the modal profile of a 50nm SiO_2 thickness in the Ag-SiO_2-Ag slab plasmon mode.

For this taper, then, the length was sequentially incremented and the loss was computed between the power flow down the 50nm straight channel and that coupled into the 1nm straight channel. The input power is defined as the optical power which arrives at the left hand side of the taper, propagating in the 50nm channel in the positive *z*-direction. Because of the complications involved with back scattering, this power cannot simply be determined by numerically integrating the Poynting vector at the input to the taper. To overcome this obstacle, the power was calculated at a point several microns in away from the input to the taper. Even this calculation was non-trivial. First, the ratio of the amplitude of the forward propagating wave in relation to that of the backward propagating wave was needed. Because the input is monochromatic, these waves create a standing wave pattern. The modulation depth of the standing wave E^2 field then allows for the determination of the ratio of these waves. Once this is known, a correction to the Poynting vector can be made which will yield the power propagating in the forward direction. Because the 50nm channel has known propagation characteristics, the loss can be accounted for and the power arriving at the taper can be determined. A similar procedure is then used to determine the power which couples into the 1nm plasmon mode at the output of the taper.

After distinguishing between forward and backward going waves, the results were surprisingly good, as plotted in Figure 3-4. Simulations show that a 70nm transverse mode (in 50nm thick SiO_2) can be coupled to a 2.6nm transverse mode (in a 1nm SiO_2 slab dielectric waveguide) with only approximately 2dB of loss. The numerically calculated power flow is shown in Figure 3-5. Even more interesting than the low loss, the minimum occurs for an angle of 30°, which is a very steep taper. This means that resistive losses are so great that efficient coupling must be accomplished over very short length scales. If one integrates the dynamic wave-vector across the taper, one finds that the taper is approximately 0.9 wavelengths long. Clearly $\delta\lambda/\lambda$ is not much less than 1. Nonetheless, the back-scattering losses in the taper are low, at approximately 1dB. For this reason we call the taper quasi-adiabatic. The very rapid transition means that the perturbative methods outlined earlier in this chapter would never have yielded the profile of the optimum taper. In fact, a gentle taper (with an opening of less than 5°) shows the very poor throughput in a transition to a 1nm channel. This is precisely the reason that the adiabatically tapered metallic pin described in Chapter 1 showed such poor enhancement when first order resistive losses were taken into account. These results hint that the throughput of the pin, too, could be greatly enhanced by optimization of the opening angle. The computational results also show that the majority of the back-scattering occurs near the sharp corners of the model. Because nano-fabrication affords us little control over such features and the loss is already very low, no attempt was made to improve throughput by rounding the corners.

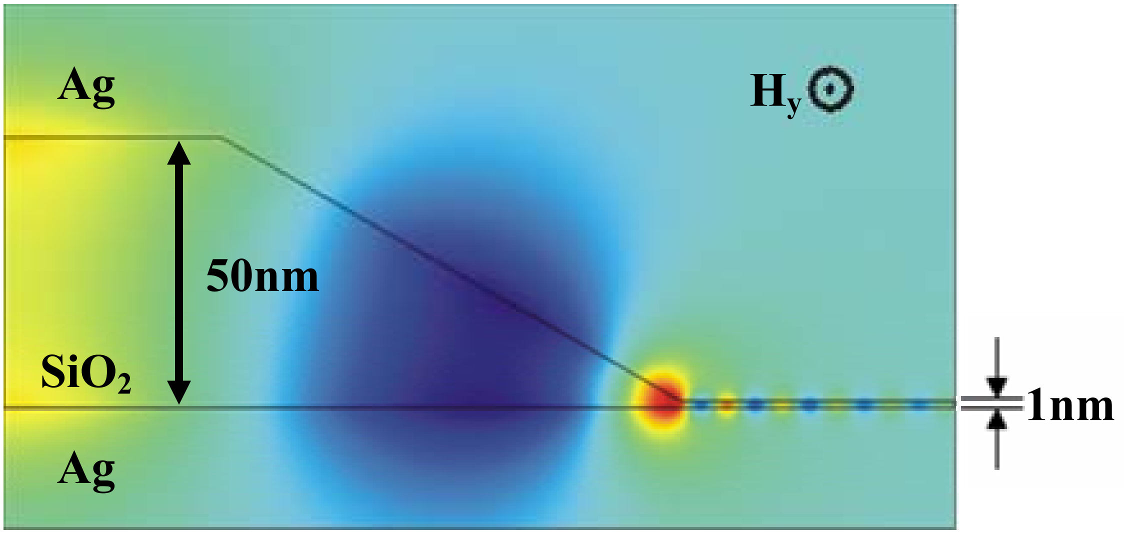

Figure 3-3: The auxilliary magnetic field in the optimized linear taper

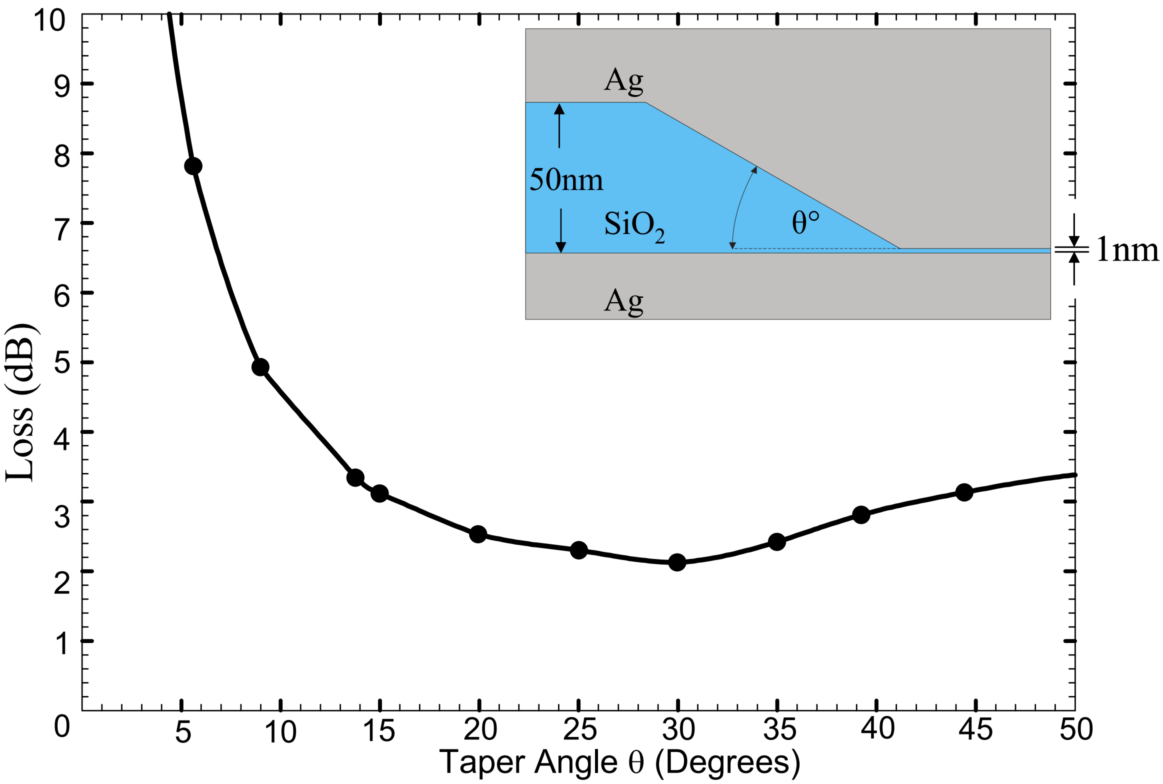

Figure 3-4: Loss across the taper at various angles

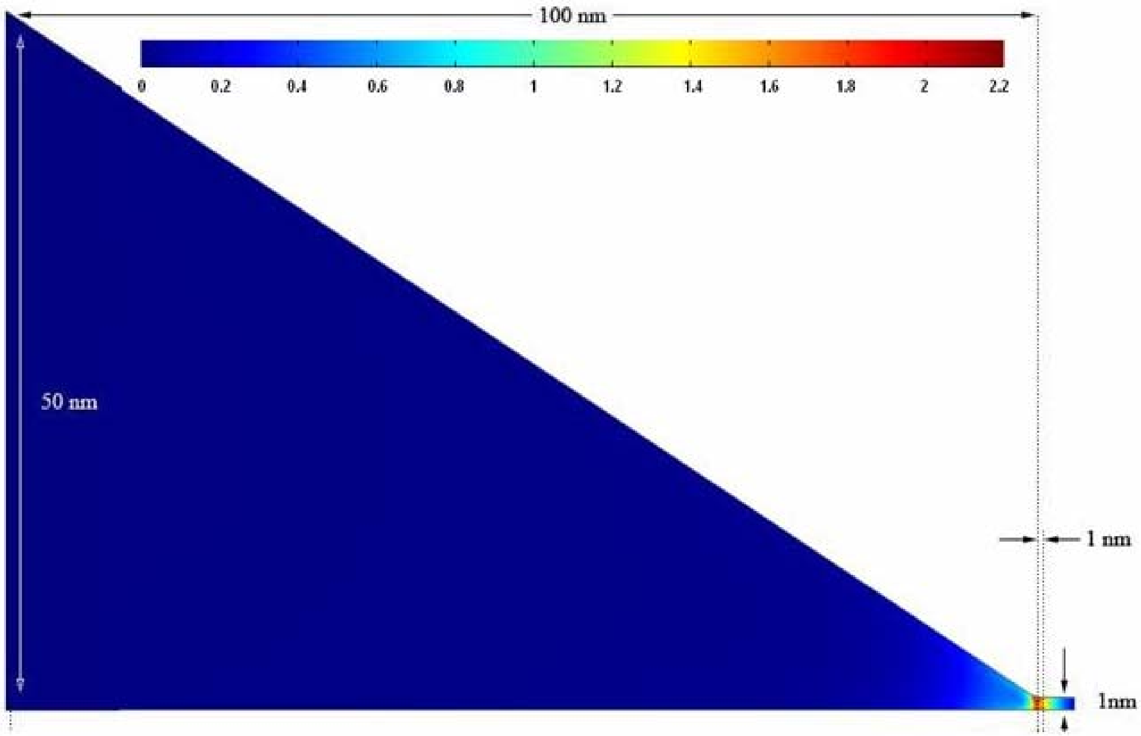

Figure 3-5: The Poynting vector across the taper

After accounting for backscattering and absorption, this two dimensional focusing structure achieves an energy density enhancement of approximately 350. At this point we must be very specific about what this number entails. Of the power arriving at the taper from the 50nm channel, this is the relative energy density compared to the field propagating forward in the 1nm channel. This factor of 350 comes from the concentration of energy along two dimensions: the reduction of velocity along the direction of propagation (the *z*-dimension) and the compression of the mode in the transverse dimension (the *x*-dimension) by the metal plates. Thus we have enhancement from the change in velocity and skin depth. The reader is reminded, however, that finite element simulations are incapable of incorporating dispersion, thus equating phase velocity with group velocity. As can be seen from even a cursory examination of the dispersion relations, the group velocity is always lower than the phase velocity in these slab structures. In the case of the 1nm channel and 2.6eV photons, the group velocity is approximately 3.5 times slower than the phase velocity. The energy density enhancement should thereby be scaled by 3.5. Dispersion can easily be incorporated by repeating the simulation at a series of discrete frequencies to determine the phase shift and loss of each monochromatic term. Fourier analysis may then be applied to this linear system to determine the compression of pulses and other input signals. Within the realm of the assumptions and loss mechanisms used, an enhancement of 350 is certainly a lower limit.

There is a great deal of field concentration at the sharp tip at the bottom of the taper. This, however, is a static enhancement which does not propagate forward in the 1nm SiO_2 mode and therefore has not been considered in our calculation. For certain applications, such as inducing local optical non-linearities, this energy can be used, and thus a higher enhancement factor will follow. This compels us to define an appropriate figure of merit for this type of nano-focusing device. Surely the size of the focal spot is significant, but this completely ignores efficiency. Here we present an alternative figure of merit

$$F \equiv \frac{c\varepsilon E_{\max}^2}{P} \tag{3-4}$$

In the above, P represents the input power into the focusing device, c is the speed of light, and εE^2 is the peak electric energy at the focus. The figure of merit represents the energy focusing power of a lens. F has units of 1/area, representing 1/spot size, but it also accounts for compression in the direction of propagation. For instance, in free-space, $1/F$ represents the smallest area to which a beam may be focused. In a lossless dielectric on the other hand, $1/F$ is the minimum area times the index of refraction of the medium. This gives weight to the slowing of the waves which obviously increases the energy density. The higher the value of F, the better the focusing power. A plot of our figure of merit for the taper of Figure 3-5 is given in Figure 3-6. The abscissa represents the channel thickness at various points on the ideal 30° taper. Because the numerical simulations are two dimensional, the figure of merit has units of inverse length rather than inverse area.

As described in Chapter 2, the E^2 is enhanced by a factor of $(1/d)$ for each dimension of focusing in the large-k limit. In the case of the MIM wedge, the focusing is two dimensional, thus the E^2 enhancement should scale with $(1/d)^2$. Thus we expect the figure of merit to have a square law dependence on channel thickness. A line representing perfect square law dependence is shown in Figure 3-6. The deviation of the actual E^2 from this trend is due to two factors. The first is the loss, which serves to reduce F. The second factor is that the entire taper is not in the regime of large wave-vectors. At a 50nm insulator thickness, the wave-vector lies close to the light line, and many of the approximations which led to the square-law dependence break down.

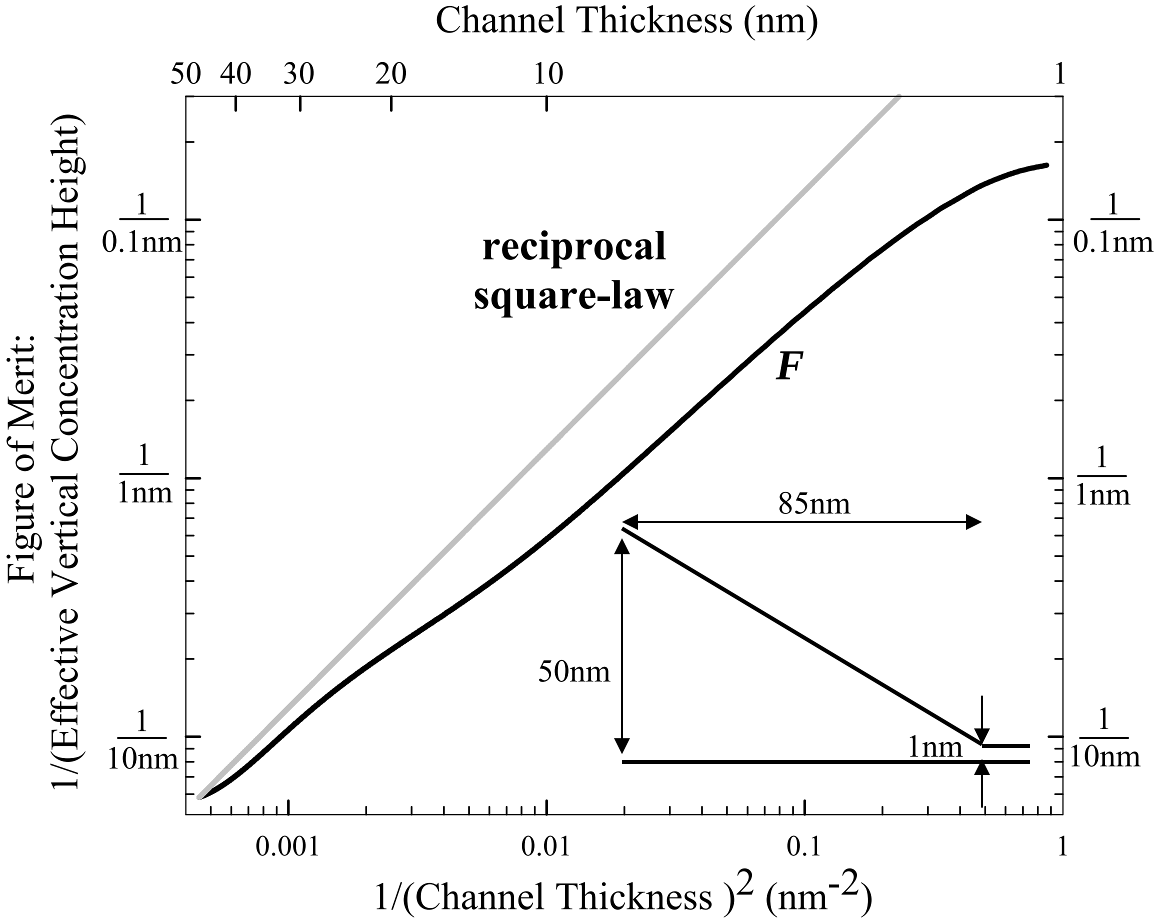

Figure 3-6: Figure of merit for the plasmonic beam as it propagates across the taper

3.3 A Three-Dimensional Focusing Device

To take advantage of the third dimension of focusing, the two-dimensional wedge structure is no longer appropriate. Instead we have developed a geometry analogous to the standard immersion lens. In this design, only a two-dimensional slice of the device resembles a wedge. In three dimensions, the device is the linear taper, which was analyzed previously, revolved about the focal point. Creating a dimple lens, it makes a tightly focused point image. The layout is illustrated in Figure 3-7. This technique differs from conventional immersion lens microscopy, however, in that the effective refractive index is changing continuously toward extraordinarily high values at the center of the dimple. The 1nm thick SiO_2 at the focus allows a 10nm plasmon wavelength for 2.6eV source photons. Conventional imaging principles[76] tell us that this would permit a ~5nm line image in the lateral dimension (see Figure 3-8). The key to this design is that the plasmon wavelength is reduced only where it need be. As the beam approaches the center, the focal structure creates an effective aperture which attenuates the high spatial frequencies. Because the plasmons are linearly increasing their wave-vector as they approach the spot, the loss of the large spatial frequencies is countered and the device is able to achieve a tight focus with low losses.

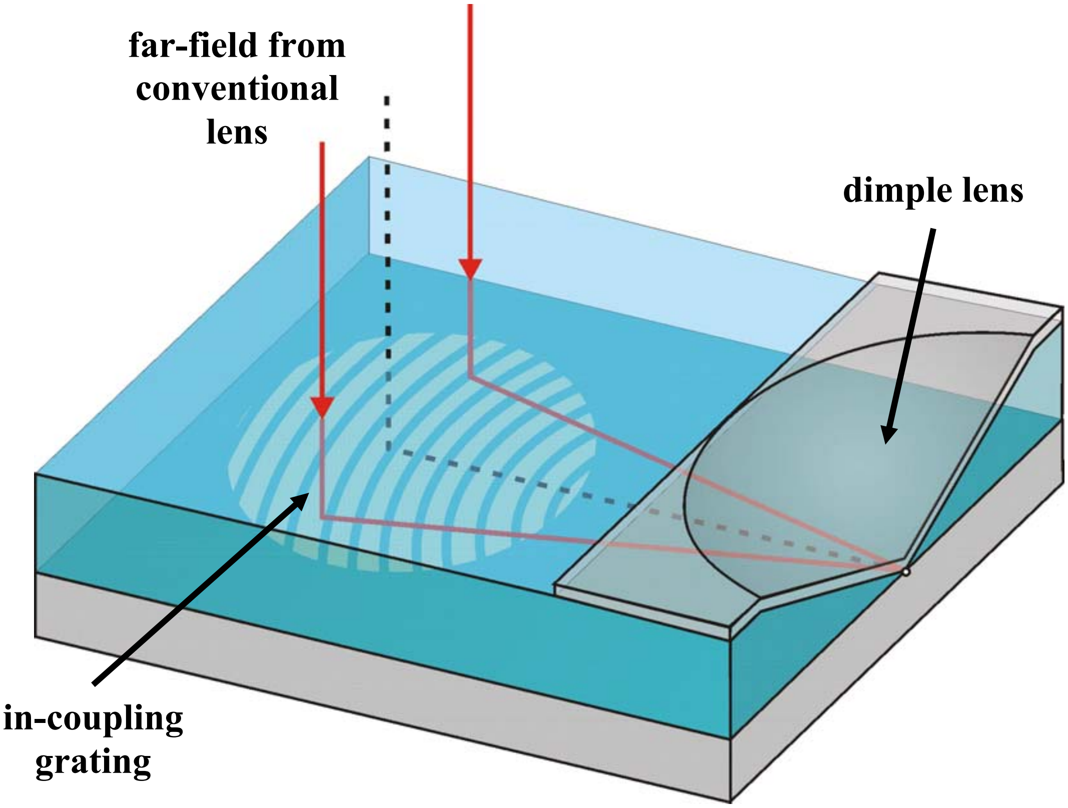

Figure 3-7: Three dimensional structure with dimple lens

Besides the cylindrical symmetry of the third dimension, Figure 3-7 has several differences from the two dimensional structure simulated in the previous section. Its two dimensional cross-section resembles the tapered structure of Figure 3-9. Most importantly, it has a grating structure to couple a free-space optical beam into the single-sided plasmon mode. Because of the wave-vector mismatch, clearly some structure is necessary to generate the requisite momentum to couple to plasmons. In this case, we have chosen to work with gratings. Preliminary optimization calculations have shown grating efficiencies greater than 55% for the case of lossless silver. This is still an ongoing optimization project, and higher efficiencies are predicted.

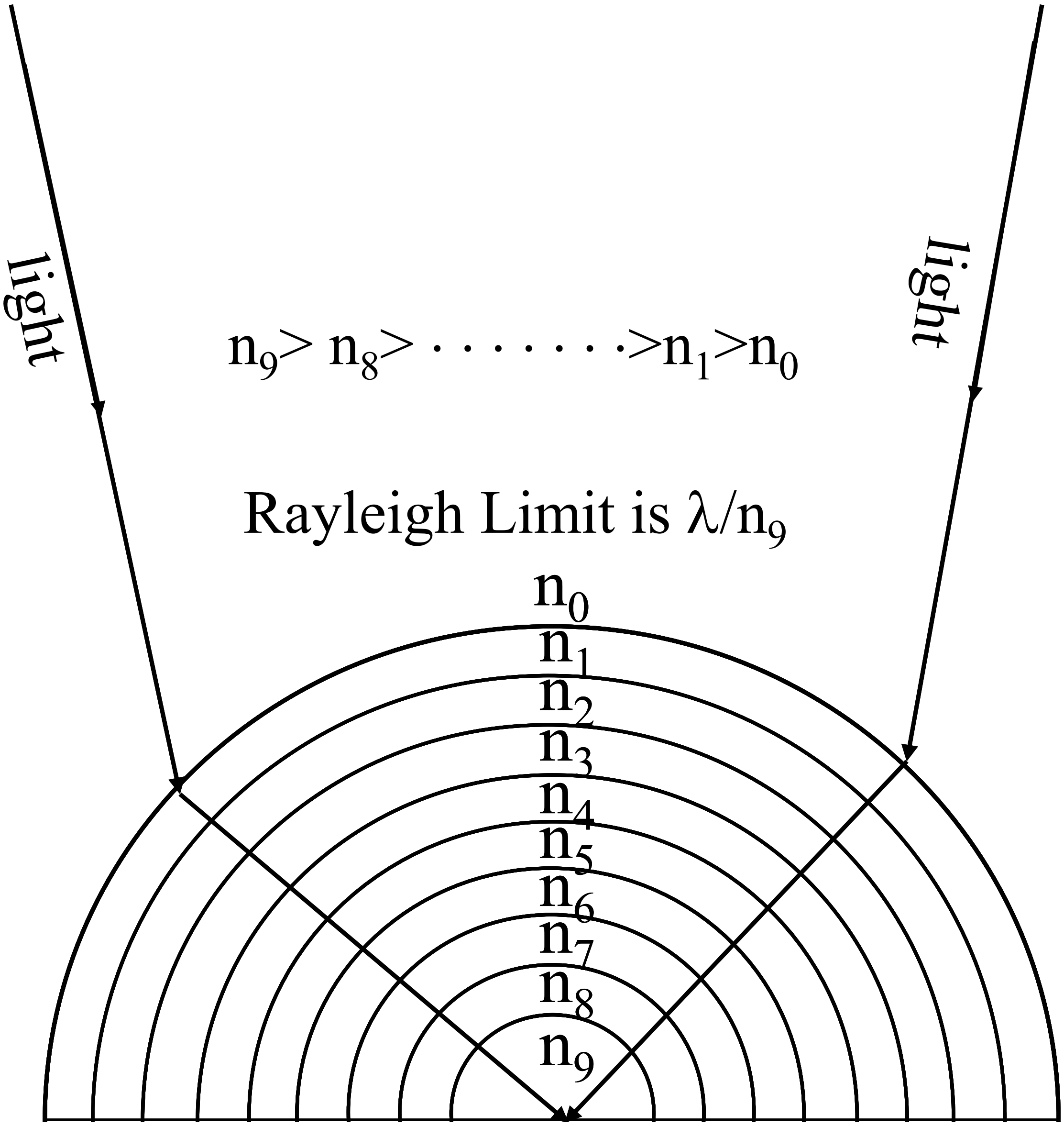

Figure 3-8: Illustration of effective index change in plasmonic lens. This represents a top-down view of Figure 3-7.

For completeness, we are compelled to mention that grating couplers are not the only form of efficient coupling. Various sources in the literature have reported high efficiencies by using end-fire coupling[86,87], which entails firing a free-space optical beam normally onto the left hand facet of Figure 3-9. This is well suited to our geometry because we are initially launching large, single-sided plasmons, which have fair overlap with an appropriately focused free-space beam. Preliminary numerical simulations in FEMLab have yielded coupling efficiencies of 35%. While our calculations suggest that it is less efficient than the grating coupler, there are situations where end-fire coupling is desirable, such in broadband plasmonic focusing devices.

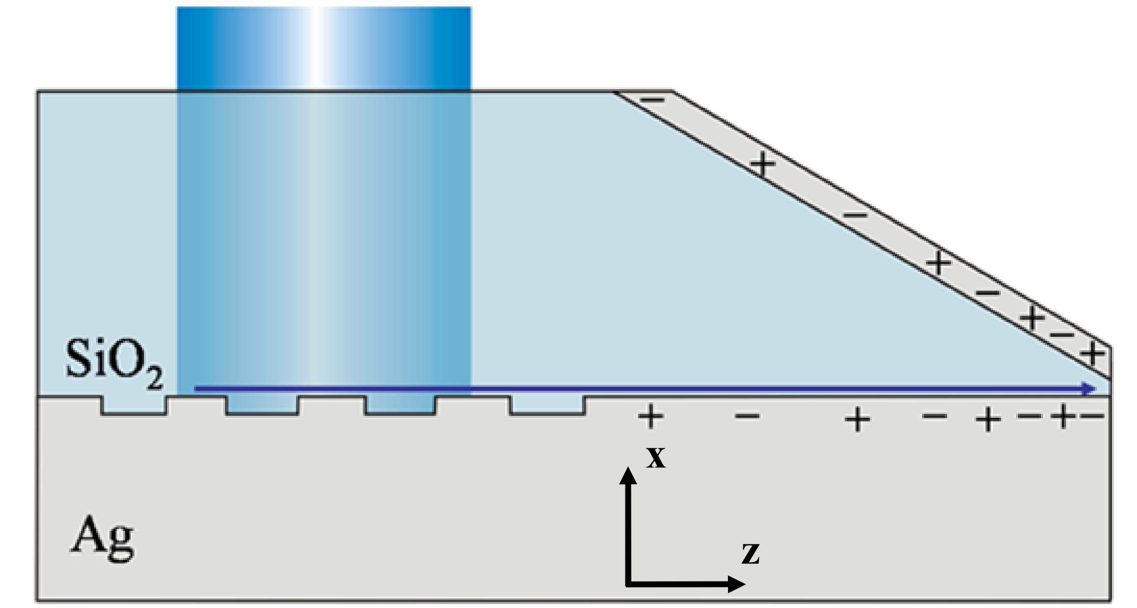

Figure 3-9: Cross section of plasmonic focusing device

The coupling from the free-space photon to a single-sided plasmon has a significant effect on the taper optimization. Instead of a 50nm double-sided plasmon channel feeding the taper, its input now consists of a single SiO$_2$/Ag interface. The taper must efficiently couple between the single sided plasmon to the double sided plasmon, eventually down to a 1nm dielectric gap. A series of two-dimensional simulations we carried out to account for the geometry illustrated in Figure 3-9 and the inset of Figure

3-10. For this optimization, there was some ambiguity as to the height at which the taper beings. The fields of the 2.6eV single-sided plasmons in SiO_2 decay by 1/*e* at 77nm away from the interface. Initial taper heights of both 100 and 200nm (on the ‘input’ side of the taper) were evaluated, however, both showed the effects of scattering off this feature. Because of this, the initial thickness was fixed at 400nm. The terminal channel thickness was kept at 1nm. Using methods identical to those of the previous optimization, the taper angle was varied and the power throughput was calculated.

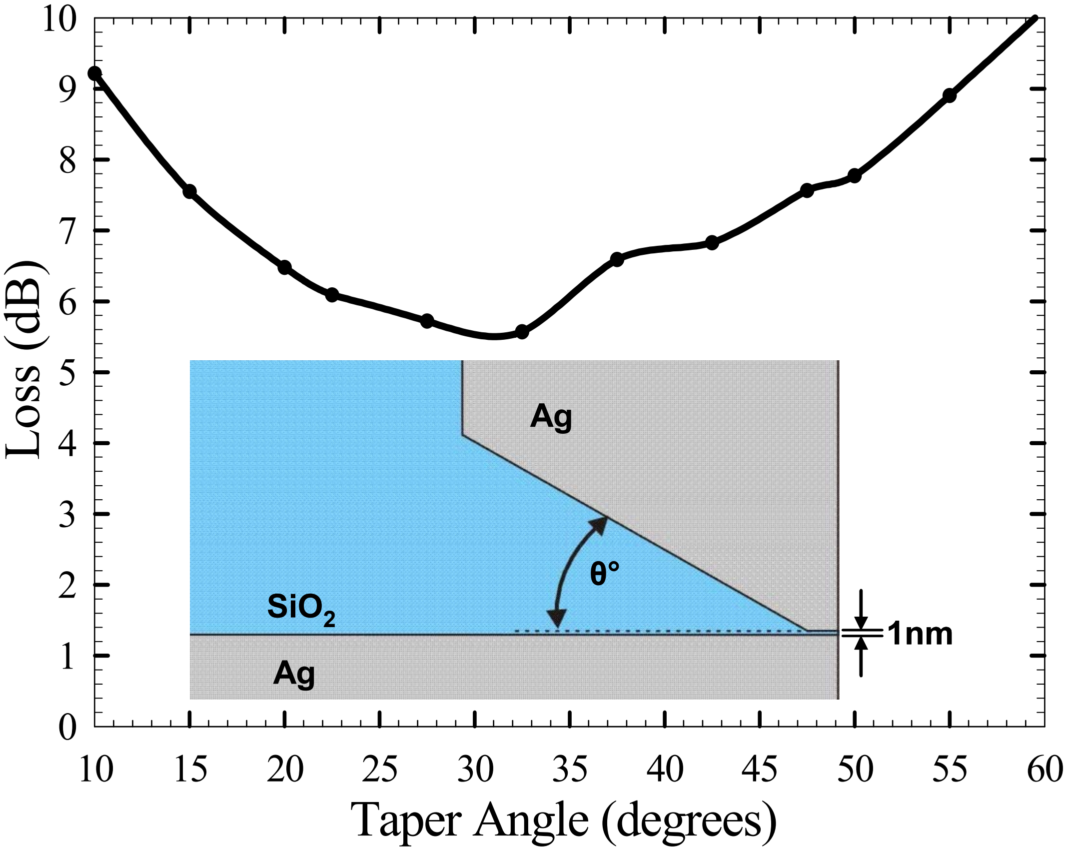

Figure 3-10: Throughput optimization for the transition from the single-sided plasmon to the 1nm channel

The results of the optimization are illustrated in Figure 3-10 and agree well with the results from the 50nm to 1nm taper. Again the greatest throughput occurs at approximately 30°. The minimum loss of 5.5dB, however, is substantially larger than the previous optimization which was as low as 2dB. Not only is this unsurprising, but is completely expected. The additional loss is a result of symmetry considerations. In the single sided plasmon, there is only one mode which propagates. In the MIM structure, however, there are both symmetric and anti-symmetric modes. Definitions of these modes are contradictory in the literature, so here we refer to the anti-symmetric mode as that which has an anti-symmetric charge profile about the center of the channel. It is this mode which has been the subject of all of our previous calculations. The geometry does permit a second, symmetric mode. Because the single sided plasmon can be decomposed into a weighted summation of both of these modes, it undergoes additional loss as part of its energy couples to the symmetric mode. Spatial overlap concepts suggest that the single sided plasmon is an equally weighted sum of both symmetric and anti-symmetric modes, which would neatly explain the 3dB differential between the results. This anti-symmetric mode does not couple to large wave-vectors at the focus and therefore its energy is lost in the transition to the double sided plasmon. This decomposition is illustrated in Figure 3-11 which plots E_z (the E-field component tangential to the interface) for the anti-symmetric mode, symmetric mode, their summation and the single sided mode for the Ag-SiO_2-Ag structure stimulated with 2.6eV photons. In these plots, the gap width is 400nm. Note that Figure 3-11 shows plots of the actual field distributions for the full solution to Maxwell's equations in these geometries, they are not drawings.

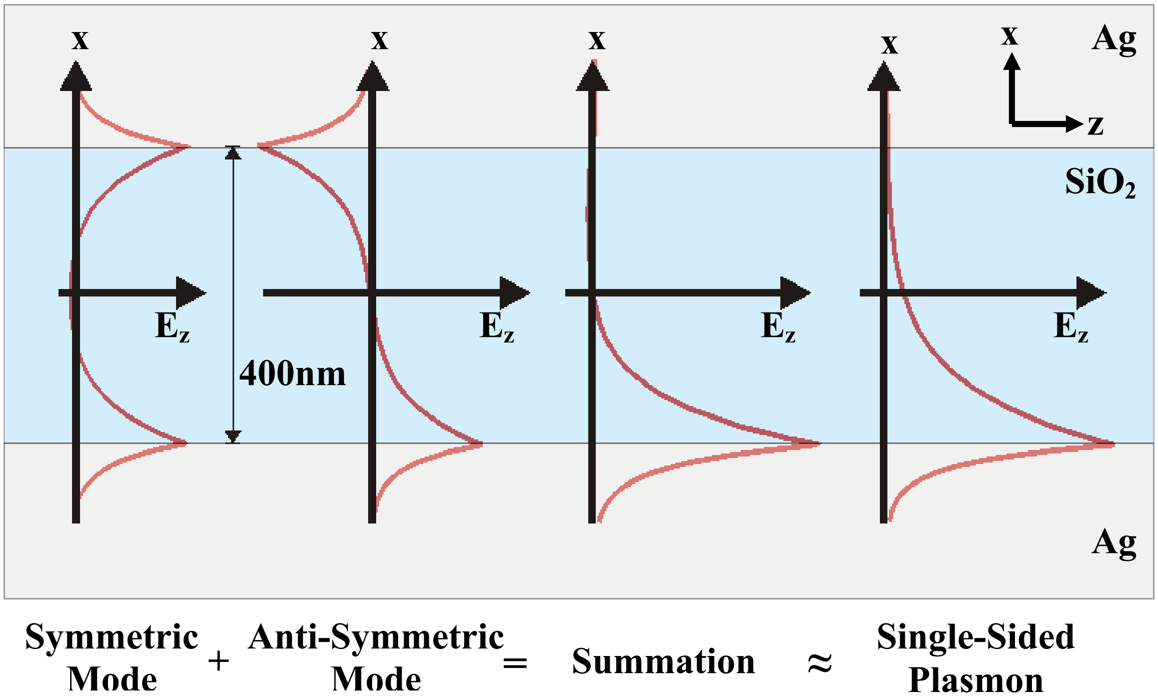

Figure 3-11: Shows both the symmetric and antisymmetric modes for a 400nm SiO2 thickness for 2.6eV plasmons. The summation of both modes approximates the single sided plasmon.

3.4 A New Class of Immersion Lens

The immersion lens formed by the conical dimple is unlike a standard immersion lens. Over the length of the taper, the effective index changes continuously by more than an order of magnitude. This creates very unusual behavior for plasmonic wave-fronts impinging on the lens. To illustrate this behavior, we have modeled the system using ray optics. First the plasmonic lens was reduced from a three dimensional geometry to a two-dimensional imaging system. In the slab mode geometry, the insulator thickness uniquely determines the wave-vector. This allowed us to replace all features in this dimension (previously referred to as the *x*-direction in all plots) with a scalar effective refractive index. This refractive index is determined from the slab mode dispersion relations by dividing the plasmon wave-vector (*k*) by the free-space wave-vector (ω/c). Once a two dimensional map of the effect index was created, we then calculated the path of the rays. Because the plasmonic lens has circular symmetry, the formula of Bouguer[9] can be used. This reduced the problem of determining the path of a ray to the solution of

$$\frac{dr}{d\theta} = \frac{r}{c}\sqrt{n^2 r^2 - c^2} \tag{3-5}$$

where c is a constant determined from the slope and position of the incoming ray. Figure 3-12(a) and (b) show the results of these calculations for rays impinging on the taper with various degrees of misalignment. From elementary optics, we know that the light is bent toward the region of high index. In our design, the circular profile and dramatic change in index conspire to force rays to the focal spot. Of course, rays incident normal to the lens focus properly on the center. Highly misaligned rays, too, are compelled to the center by this strong refraction, much as a ball rolls down a hill or light is trapped in a black hole. It is also a well known result of electromagnetics that it is energetically favorable for the field to concentrate in the higher index regions of a system[88]. Considering this result in another manner, the magnification of the plasmon lens is so high that even rays of large initial misalignment find a path which takes them directly to the focal spot. Any misalignment from the optic axis will be reduced by a factor equal to the huge ratio of the effective indices.

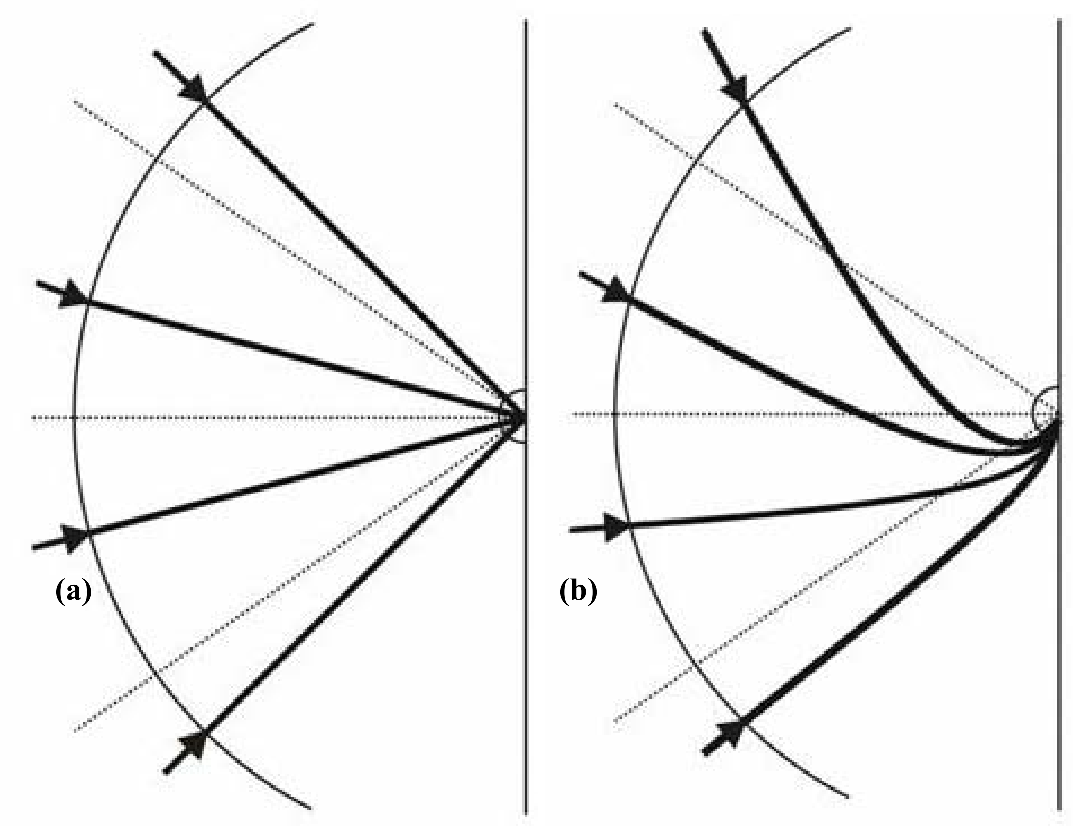

Figure 3-12: Ray tracing of aligned (a) and misaligned (b) rays across the taper

This unexpected feature shows the dimple lens to be self-correcting in addition to the other properties for which it was specifically optimized. Because of the small scales to which we are focusing, this self-correction is a necessity. Had this not been the case, any misalignment between the curved gratings and the plasmon lens would have resulted in a useless focusing device. The other aspect of this feature is that it prevents the lens from achieving image formation of anything more complex than a single spot. Creating multiple pixels at the output is not an option with such large focusing in this lossy medium. It is useful to note that although the taper has the ability to correct for some misalignment, it does not have the corrective powers to accommodate a plane wave input rather than a cylindrical input. Simulations with parallel rays show that parallel rays do not converge on the focus efficiently because the corrective power simply is not strong enough. For this reason, curved gratings must be used for in-coupling the free space beam, thereby properly orienting the rays toward the focus before they arrive at the conical plasmonic dimple lens.

The ray refraction model is a tool to establish a sense of this novel focusing lens. The attentive reader, however, will note that the entire taper is less than 1 wavelength long and clearly outside the bounds of the validity of ray optics. To solve this problem, two-dimensional wave simulations were undertaken. Again the calculations were reduced to a top view in two-dimensions by employing the effective index. It must be noted that the field vectors of surface plasmons will have very different vector distributions in comparison to the cylindrical optical waves in a two dimensional geometry. The plasmon will have fields both in and out of the plane of Figure 3-13, with vector distributions unique to these plasmons. To account for this, the 2-d wave simulation was done using TM modes, such that the *E*-fields are in-plane. This will then give us a worst-case estimate of the plasmonic focusing. The results of this simulation, plotted in Figure 3-13, demonstrate the focusing power of the lens, creating a spot size of 7nm. Further simulations also show that the design is, in fact, tolerant to deviations from perfect focusing.

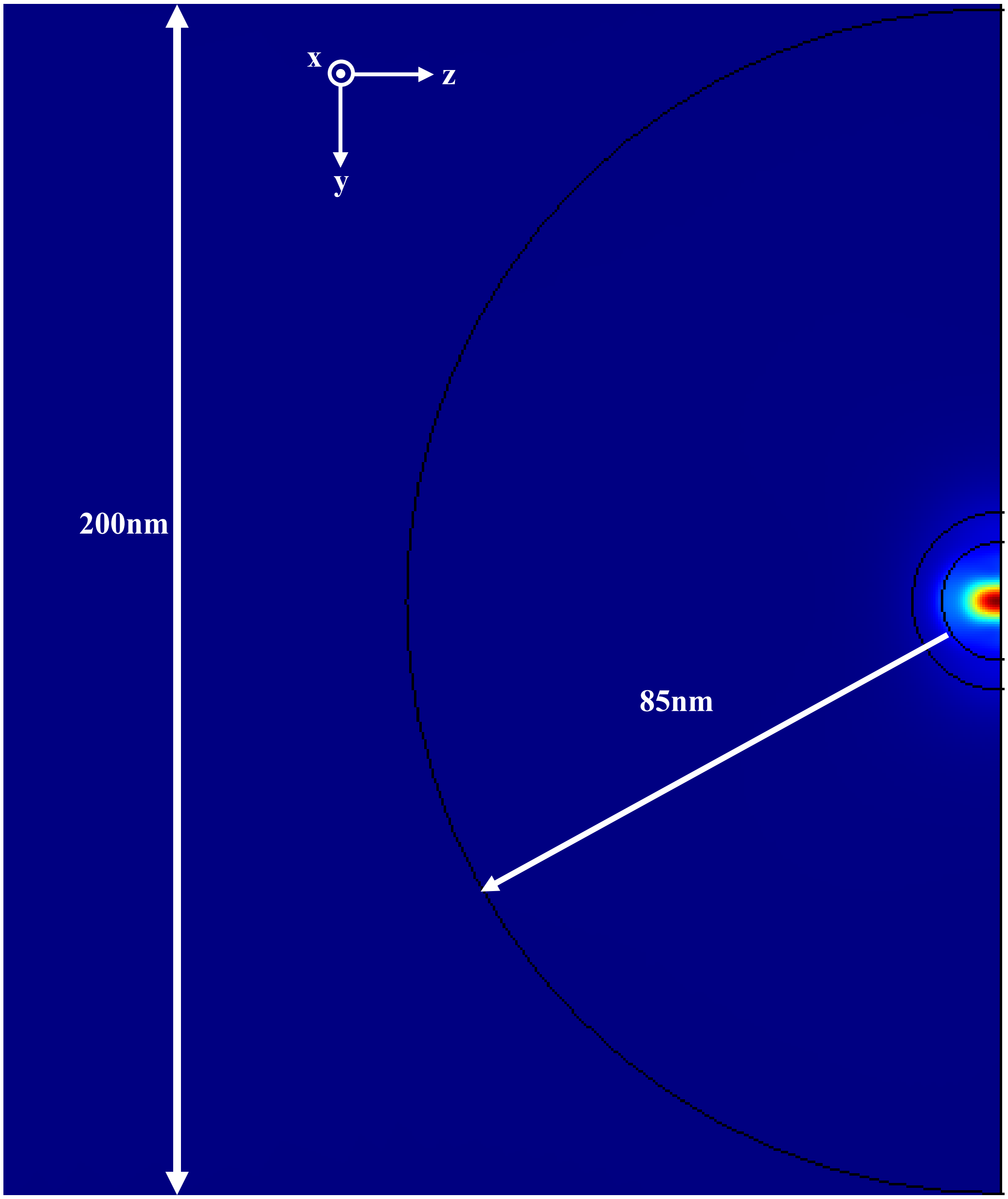

Figure 3-13: 2-d wave simulation of dimple immersion lens showing energy density.

3.5 Total Enhancement Factor and Throughput

The preceding sections have developed enough of the details of the device to determine the total E^2 enhancement factor of the focusing lens. We begin with a free space optical beam at a wavelength of 476nm which is focused down to a 1μm diameter spot. This was chosen because it is a convenient limit of most long-working-distance microscope objectives. The focused beam impinges on a grating, creating a single-sided plasmon beam, 1μm in width. Energy conservation arguments show that the square of the peak *E*-field in the plasmon is enhanced by a factor of 66 compared to that of the free-space beam. We will also assume a grating efficiency of 0.1 to be conservative. As the beam propagates across the taper, it picks up an additional E^2 enhancement of 340 as it is slowed down and confined to the 1nm plasmon channel. This accounts for the scattering and absorption losses. The beam also achieves a geometrical enhancement of 140 from the spherical focusing, as it goes from a width of 1μm down to 7nm as shown in Figure 3-13. Finally the E^2 is enhanced by a factor of 2 because, at the large-k limit, all of the energy is in the electric field and none is in the magnetic field. Putting all of these numbers together yields a total E^2 enhancement of 6×10^5 in a spot size of approximately 3nm by 7nm (see Figure 3-14). The assumed losses are 5.5dB from the taper and 10dB from the grating coupler. Of course, the losses can be improved significantly with more efficient in-coupling.

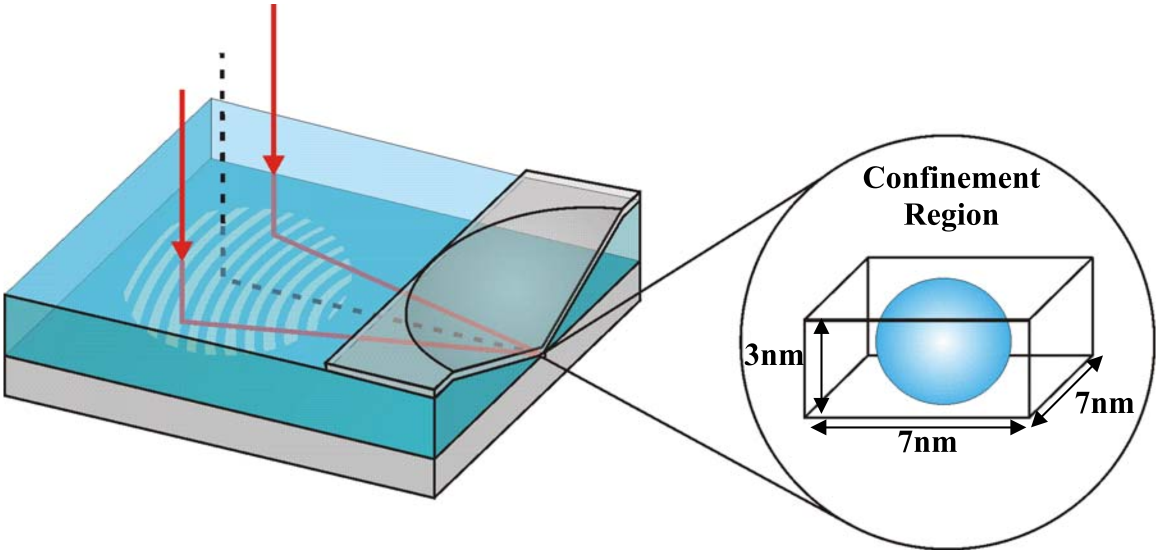

Figure 3-14: Illustration of final spot size

CHAPTER 4 THE TRANSMISSION LINE MODEL

A hidden connection is stronger than an obvious one.

-Heraclitus

This chapter presents a transmission line model for surface plasmon propagation in the Metal-Insulator-Metal (MIM) structure. While providing intuition as to the characteristics of these plasmonic modes, this model will also demonstrate the availability of very high transmission line impedance. In fact, it will be shown through fundamental arguments that efficient propagation cannot be achieved unless the plasmonic waveguide impedance becomes increasingly large. Fortunately the optical frequency modes have exactly these characteristics. The transmission line model also rationalizes the two-dimensional simulations of Chapter 3 as applied to the three-dimensional focusing structure. Finally, by reducing the results of the electrodynamic field equations to distributed parameter circuit components, plasmonic circuit design may then fall into the realm of ordinary circuit engineering. The critical difference is that there is extra inductance due to the inertia of the electron at optical frequencies, referred to as kinetic inductance.

4.1 Optical Impedance and Kinetic Inductance

Although all electromagnetic energy propagation is fundamentally a question of fields and waves[89], it is expedient in the design of electrical components to distill the complex field relations down to simple lumped parameters. This then breaks the complicated spatial description of fields and potentials into isolated components. What was once an infinite summation of the terms in a basis set converges to a few numbers representing energy storage or impedance in circuit theory. The coupling between various elements, too, may be reduced to distributed combination of inductors, capacitors, and resistors. Separating these functions and clarifying the inter-relationships between various pieces then allows for the necessary intuition to design useful devices out of these novel structures[90]. In addition to this, the highly developed techniques and optimization methodology of conventional circuit theory may then be applied to this burgeoning new field of study. Also, the need to communicate our findings to a larger audience and to compare these results with other technologies compels the analysis of surface plasmons in a transmission line model.

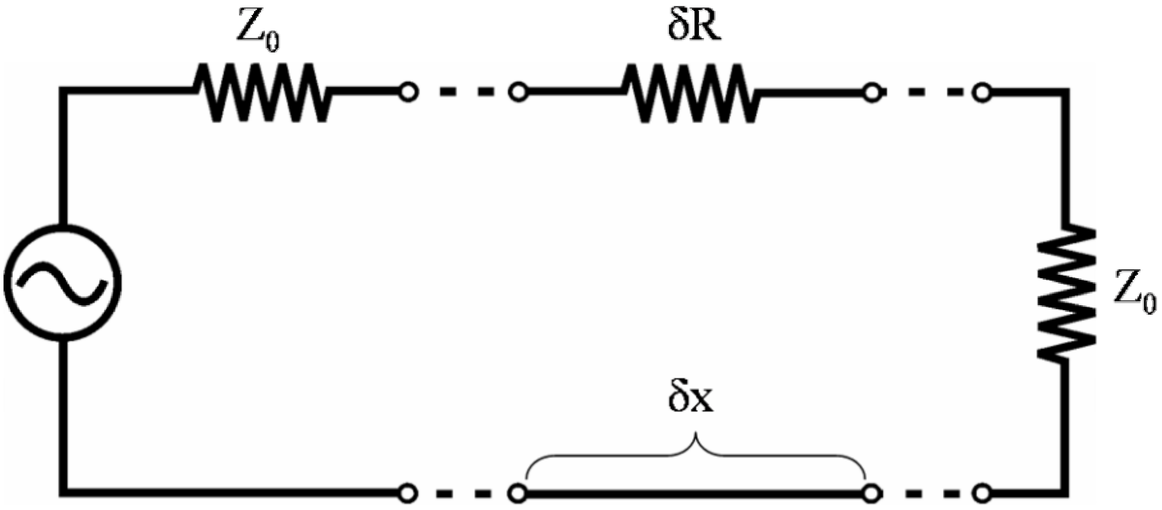

Figure 4-1: Circuit model for a lossy transmission line

Beyond intuition and design tools, the transmission line model is essential for extending the reach of our previous calculations. It is, in fact, of great use to our analysis. Because this model can represent a three dimensional waveguide, it can bridge the gap between a three dimensional focusing structure and the two dimensional calculations described earlier. The analysis contained in Chapters 2 and 3 was strictly rigorous only for slab plasmons with translational symmetry in the *y*-dimension. The numerical simulations which determined the efficiency of the taper were also for structures with no variation in along this direction. This begs the question as to what happens when the plasmons are focused in the *y*-dimension to less then 10 nanometers. Certainly these tightly focused modes may no longer be modeled as having negligible variation.

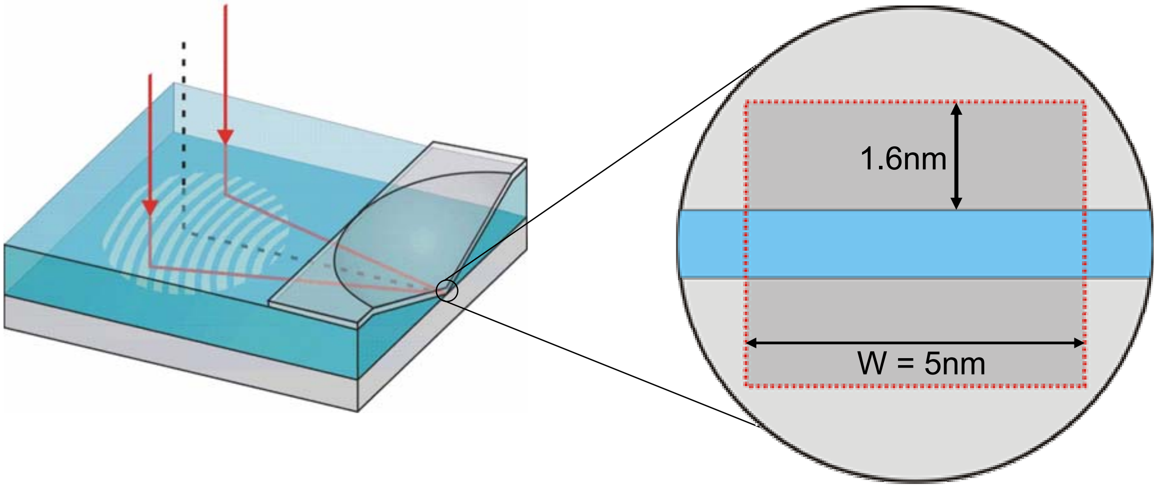

Figure 4-2: Restricted current flow at focus of plasmonic lens creating very large resistance

To begin the development of the theory of plasmonic transmission lines, the material parameters must be recast from complex dielectric constants into circuit parameters. To define the optical impedance, we return to two equivalent forms of Maxwell's Equations. The first is the general case of Ampere's Law, while the second equation is explicitly for the fields in matter. At optical frequencies, we assume that the free current is zero and that the permeability is equal to that of free space.

$$\begin{aligned} \nabla \times H &= J + \varepsilon_0 \frac{\partial E}{\partial t} \\ \nabla \times H &= \frac{\partial D}{\partial t} \end{aligned} \tag{4-1}$$

In the case of optical plasmons, the term *J* represents the bound current. We may then define a resistivity ρ such that $J = {}^{E}\!/_{\rho}$. The two equations above can be reconciled (in the frequency domain) only if

$$\frac{E}{\rho} - i\omega\varepsilon_0 E = -i\omega\varepsilon_0\varepsilon_m E \tag{4-2}$$

$$\rho = \frac{-i}{\omega\varepsilon_0(1-\varepsilon_m)} \tag{4-3}$$

Again, ε_m is the relative dielectric constant of the material and ω is the angular frequency of the optical wave. In the RF and microwave regime, the frequencies are much smaller than the reciprocal of the electron relaxation time in most metals. ε_m can be approximated as purely imaginary. This leads to the purely real resistivity to which we are accustomed. This is illustrated best by the Drude model for the dielectric constant of a free electron gas. Although silver is not strictly a Drude metal at optical frequencies, it can be well approximated as a Drude metal in the terahertz and RF range.

$$\varepsilon_{Drude} = 1 - \frac{\omega_p^2}{\omega(\omega + {}^{i}\!/_{\tau_{relax}})} \tag{4-4}$$

This illustrates not only why the resistivity is dominated by the real component at low frequencies, but also why it is approximately a constant in that range.

At optical frequencies, however, the interband transitions force us to revert to the empirically determined values of ε_m. In this high frequency regime, the dielectric constant is complex and is dominated by its real part. Because the dielectric constant is mostly real, this creates a large imaginary component of the resistivity, representing a kinetic inductance. Physically this represnts the mass of the electrons as they oscillate at such rapid frequencies. The complex resistivity as a function of frequency is tabulated in Table A-1 of Appendix A.

As is known from classical electrical engineering considerations[90], the resistance of a conductive element is equal to the resistivity (ρ) times length divided by area. Although the optical impedance is dominated by the kinetic inductance, the resistance can become very large at very small length scales. This is because the resistance grows reciprocally with length scale as we approach the nanoscale. This problem is very pronounced at the focus of our plasmonic lens and at optical frequencies. Here the 2.6eV plasmons are compressed down to a SiO_2 thickness of 1nm. In this case, the mode is focused down to a 7nm width and 1.6nm height (as shown in Figure 4-2). The top and bottom conductor act in series, making the resistance per unit length approximately 22kΩ/μm. This series resistance is incredibly large and could cause the plasmonic propagation to be very lossy.

The key to overcoming this gargantuan loss and redeeming our previous calculations is found in the formalism of the transmission line. Figure 4-1 illustrates the equivalent circuit of a lossy transmission line. Consider each infinitesimal unit of length as a simple voltage divider. The lossy line will have a resistance of δR*δl, where δR is resistance per unit length, and δl is the incremental distance. The Thevenin Equivalent circuit[91] is an ideal voltage source with a series resistance δR*δl, feeding into a resistor equal to the transmission line impedance (Z_0). In the limit of an infinitesimal length, the voltage drop across the lossy resistor goes to $\frac{V_0 \delta R \delta l}{Z_0}$. Clearly this loss can be made negligibly small by making Z_0 large. Therefore, to maintain the integrity of our assumptions in Chapter 3, the transmission line impedance must grow reciprocally with the transmission line width at the same rate as the series resistance. The analysis developed below shows that the tapered plasmonic transmission lines have a precisely divergent wave impedance of this form. This is not only a necessity for efficient propagation but it also vindicates the excellent efficiencies projected in Chapter 3.

4.2 Characteristic Impedance of the MIM Geometry

Application of the transmission line model of the MIM structure rests on the magnetostatic approximation (also known as quasi-static approximation[3]). This allows the electric field to be written strictly as the gradient of the scalar potential (V) which then rationalizes expressing the voltage as a path integral of the electric field. For this approximation to be valid, the fields must be approximately irrotational and essentially magnetostatic. Mathematically, this is expressed as

$$\nabla \times E = 0 \qquad (4\text{-}5)$$

This is more general than the electrostatic approximation[92] because it applies to transmission lines longer than the free-space wavelength. Clearly such an approximation is not valid in the regime of the dispersion relation near the light line. In that case, a large portion of the electromagnetic energy is carried by the magnetic field, which is varying with time at optical frequencies. Thus the small-*k* plasmons are not in the regime of magnetostatics.

The region of large *k*-vector, on the other hand, has very little energy in the magnetic field. As *k* breaks away from the light line, the term describing the exponential decay into each media simplifies, as discussed in Chapter 2

$$K^2 \equiv k^2 - \frac{\varepsilon\omega^2}{c^2} \approx k^2 \tag{4-6}$$

The field quantities for forward traveling waves may then be decomposed into the terms:

$$E_x = B_{1x}e^{kx+ikz} + B_{2x}e^{-kx+ikz} \tag{4-7}$$

In the above equation, B_{1x} and B_{2x} represent field amplitudes in the x direction. We then write a similar equation for E_z

$$E_z = B_{1z}e^{kx+ikz} + B_{2z}e^{-kx+ikz} \tag{4-8}$$

We now examine only the first term in Equations (4-7) and (4-8). B_{1z} may be found in terms of B_{1x} by a simple application of Gauss's Law.

$$\nabla \cdot D = 0 = \nabla \cdot E = \frac{dE_x}{dx} + \frac{dE_z}{dz} \tag{4-9}$$

$$B_{1z} = iB_{1x} \tag{4-10}$$

Likewise for the second term, Gauss's law yields

$$B_{2z} = -iB_{2x} \tag{4-11}$$

Once these coefficients are known, the curl of the electric field is then computed directly. It is found to be identically zero in this 'large-*k*', or short length scale approximation. Because $\nabla \times E = -{}^{\partial B}\!/\!{}_{\partial t} \approx 0$ and the magnetic field is oscillating at optical frequencies, this implies that the amplitude of the magnetic field is negligible in this wave-vector range. Thus justifies the formalism of Chapter 2 and implies that the field is both electrostatic and magnetostatic, greatly simplifying the analysis.

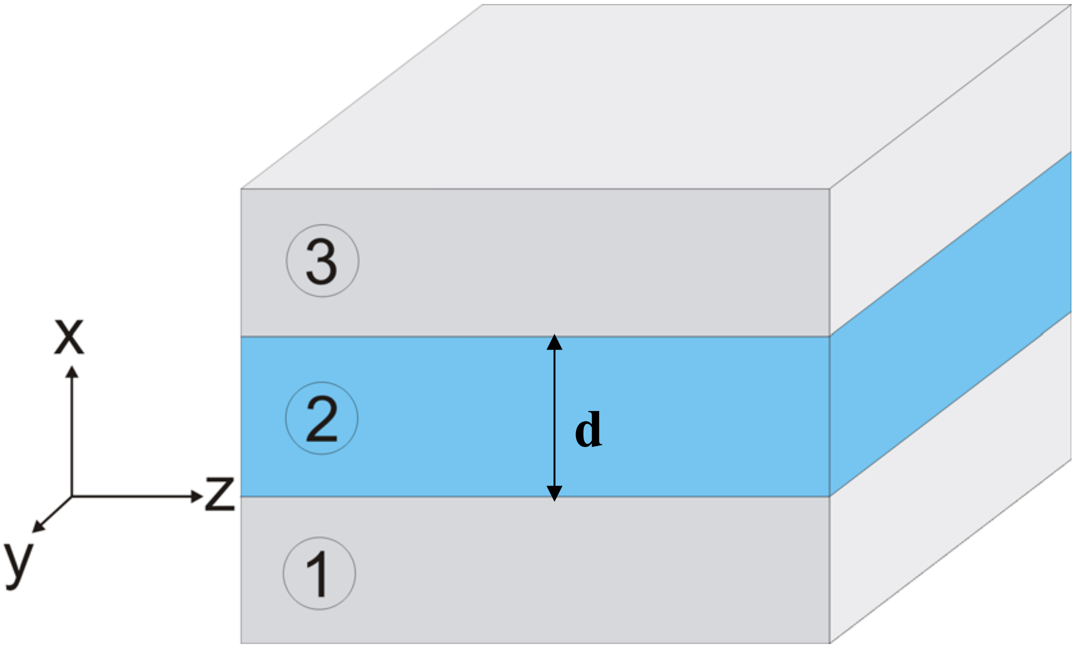

Figure 4-3: Geometry of MIM structure. Propagation is along the z direction.

The fact that the magnetic field becomes negligible at these large wave-vectors can be a cause for confusion among some readers. For monochromatic plane waves propagating through free space, the energy of the electric and magnetic fields are equal. In this case, the wave is exchanging energy between these two fields harmonically, analogous to the exchange of kinetic and potential energy for a mechanical pendulum. Obviously, this exchange mechanism is absent for the large wave-vector plasmon. Instead of conserving instantaneous energy through exchange with the magnetic field, the large-k plasmons exchange energy between the E_x and E_z fields, which are precisely 90° out of phase.

Once the fields enter the quasi-static regime, it is appropriate to apply circuit models. There are then many methods of calculating the transmission line wave impedance. The most straight-forward and exact calculation is achieved by solving for the ratio of voltage to current directly from the field relations. While rigorous, this method does little to establish intuition. In that regard, two other methods are presented which make more approximations but yield deeper insight. These will employ simple parallel plate models from conventional electrostatics and basic energy flow concepts.

We begin with an explicit statement of the fields in the three layers of the material stack (see Figure 4-3). The interface of materials 1 and 2 is defined as $x = 0$, and the z-axis is defined as the direction of plasmon propagation. The fields in each medium are derived from the wave equation and Gauss's law, unique to within a scale factor. The electric fields in medium 1 are:

$$\begin{aligned} E_x &= Ae^{kx+ikz} \\ E_z &= iAe^{kx+ikz} \end{aligned} \tag{4-12}$$

In medium 2:

$$\begin{aligned} E_x &= B_1 e^{kx+ikz} + B_2 e^{-kx+ikz} \\ E_z &= iB_1 e^{kx+ikz} - iB_2 e^{-kx+ikz} \end{aligned} \tag{4-13}$$

In medium 3:

$$\begin{aligned} E_x &= Ce^{-kx+ikz} \\ E_z &= -iCe^{-kx+ikz} \end{aligned} \tag{4-14}$$

In the equations above, A, B_1, B_2 and C are field amplitudes to be determined. Because the electric field is irrotational, the voltage between the plates can then be calculated directly from the E_x in medium 2.

$$V = \int_0^d E \cdot dx = \int_0^d \left(B_1 e^{kx} + B_2 e^{-kx} \right) dx \tag{4-15}$$

$$V = 2\int_0^d B_1 e^{kx} dx = \frac{2B_1}{k}\left(e^{kd} - 1 \right) \tag{4-16}$$

Because the integral over the B_1 and B_2 terms is symmetric for this plasmon mode, B_2 is eliminated. B_1 is then eliminated using considerations introduced in Chapter 2, finally yielding

$$V = \frac{A}{k}\left(\frac{\varepsilon_m}{\varepsilon_d} + 1 \right)\left(e^{kd} - 1 \right) \tag{4-17}$$

The current (I) may then be found by integrating the current density in the metal plate of medium 1. The width of the mode in the y-direction is represented by W. Ohm's law in the metal can be written as

$$\frac{I}{W} = \int_{-\infty}^{0} J_z dx = \int_{-\infty}^{0} \frac{E_z}{\rho} dx \tag{4-18}$$

where $\rho \equiv \rho(\omega)$ is the predominantly reactive plasmonic resistivity derived previously.

$$\frac{I}{W} = -i\omega\varepsilon_0(\varepsilon_m - 1)\int_{-\infty}^{0} E_z dx$$

Substituting the expression for E_z given above and integrating we obtain

$$I = \frac{WA\omega\varepsilon_0\left(\varepsilon_m - 1\right)}{k} \tag{4-19}$$

Once voltage and current are known, solving for the transmission line impedance (Z_0) is, by definition, the ratio of the two.

$$Z_0 \equiv \frac{V}{I} = \frac{1}{W\omega\varepsilon_0\varepsilon_d\left(\varepsilon_m - 1\right)}\left(\varepsilon_m + \varepsilon_d\right)\left(e^{kd} - 1\right) \tag{4-20}$$

Notice that the waveguide impedance Z_0 diverges as W goes to 0, implying a good plasmonic transmission efficiency.

Basic Transmission Line Theory can also be used to derive the dispersion relations $k \equiv k(\omega)$ in the large-k limit. We begin with a simple derivation which links the transmission line impedance with the wave-vector. First we have the mathematical form of the voltage drop across a length of conductor with series impedance per unit length defined as Z' (**not** the transmission line impedance).

$$\frac{dV}{dz} = -Z'I \tag{4-21}$$

For the sake of clarity, we will only consider forward propagating waves. In this case, we know that all of the fields have the functional z-dependence of e^{ikz}.

$$ikV = -Z'I \tag{4-22}$$

By the definition of transmission line impedance described above, we also know that $Z_0=V/I$. Putting both of these equations together, we arrive at the well known relation[90]

$$iZ'/k = Z_0 \tag{4-23}$$

We may then derive the series impedance per unit length by simply dividing the resistivity by the effective cross-sectional area of the mode, as described above.

$$Z' = \frac{2ik}{\omega\varepsilon_0(\varepsilon_m - 1)W} \tag{4-24}$$

Z' is primarily inductive due to the electron inertia. We now have two equations for Z_0, Equation (4-20) and Equation (4-23). Equating these and manipulating yields the large wave-vector dispersion relations.

$$e^{kd} = \frac{\varepsilon_m - \varepsilon_d}{\varepsilon_m + \varepsilon_d} \tag{4-25}$$

The reader will note that this is exactly the dispersion relation obtained from Maxwell's equations in the large-k approximation of Chapter 2. Therefore we have an independent derivation of the dispersion relations from the transmission line model in the electrostatic regime. Finally, substituting the dispersion relation into the expression for Z_0 gives

$$Z_0 = \frac{2ik}{\omega\varepsilon_0(1-\varepsilon_m)W} = \frac{\lambda_0}{W}\frac{377\Omega}{\pi(1-\varepsilon_m)} \qquad (4\text{-}26)$$

4.3 Alternative Derivations of Plasmonic Transmission Line Impedance

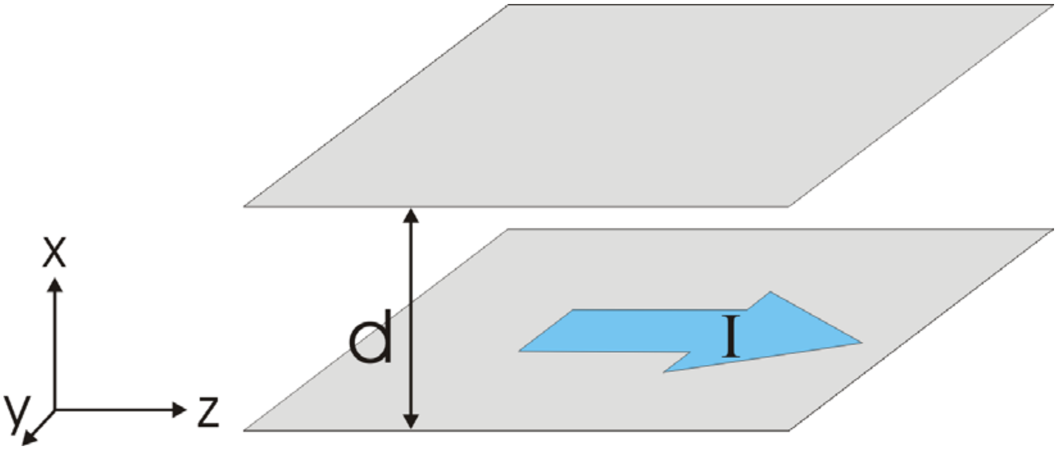

Figure 4-4: Parallel plate geometry

While exact in the electrostatic limit, the above derivation can be approximated through simplifications based on a parallel plate model of the plasmonic transmission line. We begin with the parallel plate geometry shown in Figure 4-4. The plates act as a conventional capacitor with negligible fringing fields. In such a case, the electric field between the plates is in the *x* direction and is a fixed constant. The voltage is then equal to the plate spacing (*d*) times the constant electric field (E_x). The current flowing through the plates is found from Ampere's Law to be $H_y \times W$. To find the transmission line impedance, we now only need a relation between H_y and E_x. Using Ampere's Law again, we find

$$\frac{E_x}{H_y} = \frac{k}{\omega \varepsilon_0 \varepsilon_d} \tag{4-27}$$

$$Z_0 = \frac{V}{I} = \frac{d}{W}\frac{E_x}{H_y} = \frac{d}{W}\frac{k}{\omega \varepsilon_0 \varepsilon_d} \tag{4-28}$$

Equation (4-28) can be cast in familiar form by finding an approximation for *k*. This is accomplished by Taylor expanding the dispersion relation about $\varepsilon_d/\varepsilon_m$. This is appropriate for most frequencies below 3eV. As shown in Chapter 2 and Appendix A, it is these photon energies below 3eV which have the largest *Q* and most favorable propagation characteristics.

$$k = -\frac{1}{d}\ln\frac{\varepsilon_m + \varepsilon_d}{\varepsilon_m - \varepsilon_d} \approx -\frac{2\varepsilon_d}{d\varepsilon_m} \tag{4-29}$$

Substituting this approximation for *k* into our expression for Z_0 yields a surprisingly accurate result.

$$Z_0 = \frac{\lambda_0}{W}\frac{377\Omega}{\pi\left|\varepsilon_m\right|} \tag{4-30}$$

Equation (4-30) approaches Equation (4-26) asymptotically as $\varepsilon_m \to -\infty$ when the photon energy goes to zero, and is very close to the proper result at 2.6eV.

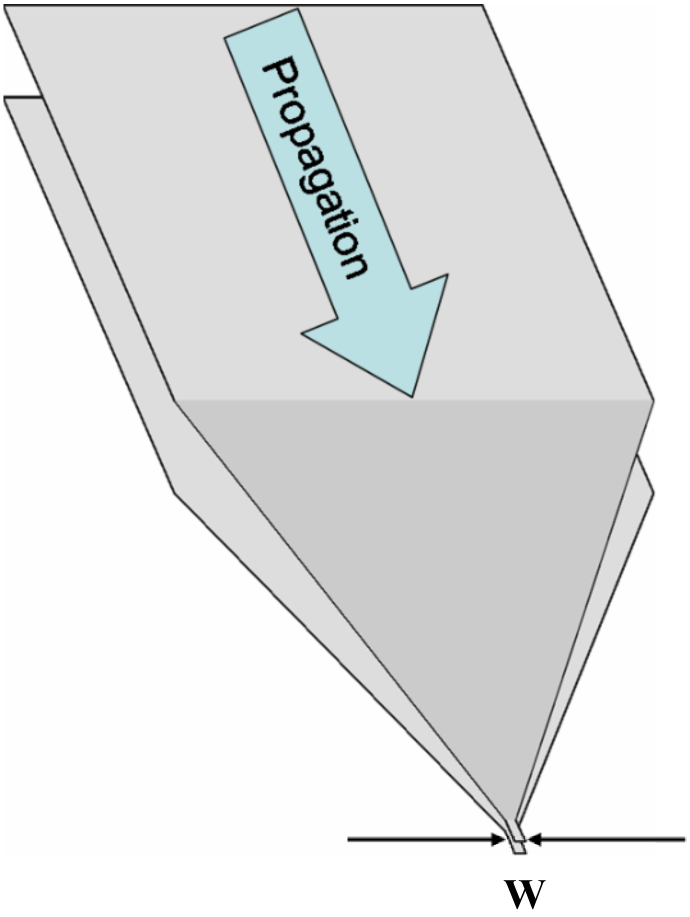

Figure 4-5: Three dimensional focusing structure cast as parallel plates

The simple parallel plate waveguide is a standard in electrical engineering pedagogy. Nonetheless, these simple modes generate a transmission line impedance very close to that derived from the exact plasmonic fields. These complicated plasmon modes, with frequencies and dispersion relations very different from conventional waveguides, still follow basic engineering principles. To give the reader one more bout of intuition, we present a third derivation for the transmission line impedance which invokes neither Gauss's nor Ampere's Law. Assuming only that the electric field is a constant between the parallel plates, this derivation uses basic energy equivalence concepts. Elementary circuit concepts state that the power in a circuit element is equal to V^2/Z_0. Conservation of energy tells us that the flux through a bounded area is equal to

$$P = Energy\ Density \cdot \mathrm{v}_g \cdot Area = \frac{V^2}{Z_0} \tag{4-31}$$

We are analyzing the case of monochromatic input, so the group velocity is equal to the phase velocity.

$$\mathrm{v}_g \approx \mathrm{v}_p = \frac{\omega}{k} \tag{4-32}$$

In the electrostatic regime and with an infinite parallel plate geometry, the energy density is simply the electrostatic energy density in the dielectric medium. The cross sectional area is taken as the width times the insulator thickness.

$$EnergyDensity \cdot Area \approx \varepsilon_0 \varepsilon_d E^2 W d \tag{4-33}$$

Finally, the voltage is taken as the field times the insulator spacing ($V=Ed$). Putting this all together and manipulating gives

$$Z_0 = \frac{d}{W} \frac{1}{\varepsilon_0 \varepsilon_d \mathrm{v}_p} \approx \frac{\lambda_0}{W} \frac{377\Omega}{\pi |\varepsilon_m|} \tag{4-34}$$

In the final expression, the approximation for k is employed, as was done in the case of the parallel plate capacitor. Upon inspection of the three derivations of impedance, it is clear that all three are equivalent. All of the relations presented above, then, are applicable at the desired frequencies of operation of our plasmonic lens.

4.4 Ramifications and Discussion

Through both intuitive and rigorous means, we have shown that the transmission line impedance of the MIM structure can be made very large. This impedance diverges reciprocally with the width (W) of the plasmonic wave-guide. For the novel plasmonic lens described in this thesis, the impedance can be made *several times larger than* the impedance of free space at the focus. This is the source of several effects which are crucial to plasmonic devices. First and foremost, this enhances the throughput of the channel. Clearly the resistive impedance of the channel increases as more current is focused into a smaller area. From an initial evaluation, then, this would seem to preclude any kind of efficient focusing of the surface plasmon waves. Fortunately, the transmission line impedance increases at the exact same rate. This keeps the overall loss independent of the focusing and strictly a function of channel thickness. Plasmonic losses can therefore be kept manageable for a short taper.

These results also confirm the assumptions made in Chapter 3 which used geometric arguments to generalize the two-dimensional simulations to the full three-dimensional device. Transmission line theory tells us that focusing the beam has no effect on the efficiency since both Ohmic resistance and waveguide impedance diverge together. In light of work with plasmonic wires[36], this should come as no surprise. This geometry, described in Chapter 1, consists of a thin metallic cylinder surrounded by a dielectric. For this mode, the symmetry of the problem allows for an exact analytical solution for the propagation losses due to absorption. In these modes too, the series resistance becomes exceedingly large as the radius of the wire is made very small. This, however, is exactly compensated by the transmission line impedance of the wire in exactly the same manner as in the focused parallel plate geometry outlined in this chapter. Since it has an exact three-dimensional analytical solution, the plasmonic wire is proof of the potential for reasonable coupling efficiency to the nanoscale.

The second important result of the large wave-guide impedance is in impedance matching. Many applications, from microscopy to lithography, require efficient coupling between the tightly focused plasmons and the free space near-field. Delivery of energy between these modes requires an impedance transformer, from the 50 Ohms of an antenna to the much higher impedance of the nanoscale. The greater the transmission line impedance, the greater the voltage that can be generated at the nanoscale.

The reader is warned to interpret the language of impedance carefully. With proper selection of channel thickness and focal spot, the plasmonic waveguide can be made to match the impedance of free space (377Ω). This does not mean that the focused plasmon will couple efficiently to free space. At the focus of the plasmonic waveguide, the energy acts as a source for generating optical energy in free space. When decomposed into a basis set of plane waves, though, the spatial frequencies involved will be far beyond the light line for the same considerations outlined in Chapter 1. Thus, all of the wave-vectors will be large in the focal plane, leaving only imaginary wave-vectors along the direction of propagation. Regardless of the impedance, these tightly confined modes can only efficiently couple to the near-field.

CHAPTER 5 ADDITIONAL LOSS MECHANISMS

The trouble with life isn't that there is no answer, it's that there are so many answers.

-Ruth Benedict

This chapter presents an overview of the higher order loss mechanisms. Specifically, we examine the effects of surface roughness, Landau damping and non-local electron conduction on the propagation parameters of the surface plasmons. Of these effects, the non-local electron conduction at the small length scales of the focused plasmons proves to be the most problematic, providing a fundamental limitation to the plasmonic propagation.

5.1 Surface Roughness and Landau Damping

Surface roughness can play an important role in limiting the efficiency of the taper lens structure. To address this issue, Atomic Force Microscopy (AFM) scans were taken of electron-beam evaporated silver and SiO_2 films that will be necessary for the planned plasmonic lens device. A sample line scan of a silver film is shown in Figure 5-1, showing a correlation length of approximately 100nm.

Closed form expressions have previously been derived in the literature for plasmon scattering and out-coupling due to roughness effects[93,94]. These expressions break down, however, as the plasmon wavelength becomes very small. Because we are interested primarily in short plasmon wavelengths this analysis does not suffice and numerical simulations were required. To accomplish this, the empirical surface profile data was used in the same FEMLab simulations as described in Chapter 3 using an interface known as CANVAS[95] which was developed in-house. After the simulations were complete, they showed only a minimal reduction in throughput efficiency. The reader is reminded that all of the numerical simulations were done in two dimensional space only. The scattering due to surface roughness which these models can describe, then, is only the back-scattering. While our results suggest that this effect is negligible, it is advised that full three-dimensional simulations be done before completely ruling out scattering in all other directions.

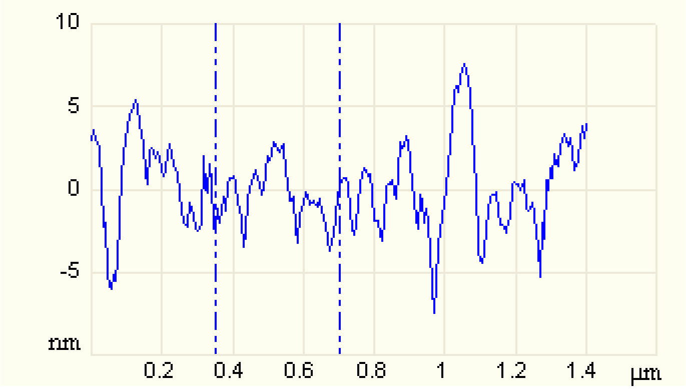

Figure 5-1: AFM line scan of e-beam evaporated silver

Likewise, Landau damping is also ignored, as the phase velocity of the surface plasmon in much larger than the electrons Fermi velocity. Landau damping arises from the non-local optical conductivity. At the thinnest portion of the taper, the phase velocity is still more than four times greater than the Fermi velocity. Because of this discrepancy, the Fermi electrons cannot travel along the crests of the plasmon field long enough to change the dynamics of propagation. Intuitively, this explanation enables us to dismiss Landau damping factors, and the analysis of Section 5.3 bears out this conclusion.

Another non-local effect, known as the anomalous skin effect, cannot be dismissed so easily. While the phase velocity is significantly larger than the Fermi velocity in our structure, the group velocity comes very close to the Fermi velocity at the focus of our lens. Clearly this should have important effects on the propagation characteristics which are not described by the local, bulk dielectric constant. It is the subject of this chapter to evaluate this loss mechanism. We will demonstrate that it provides a limit to efficient nano-focusing when the plasmon group velocity is of the order of the Fermi velocity.

5.2 Non-local Conductivity, an Overview

There is an overwhelming amount of experimental evidence[96,97,98,99] which demonstrates that the dielectric constant of a metal can no longer be equated with that of the bulk material at very large wave-vectors. As is known in solid state physics, the dielectric constant is not only a function of frequency, but of wave-vector as well. The formulation of the dielectric permittivity for the general case in an isotropic medium is given below[100].

$$\vec{D}(\vec{x},t) = \int d^3\vec{x}' \int \varepsilon(\vec{x}',t') E(\vec{x}-\vec{x}',t-t') dt' \qquad (5\text{-}1)$$

This convolution in space and time can be reduced in Fourier space for the case of harmonic fields to

$$\vec{D}(\vec{k},\omega)=\varepsilon(\vec{k},\omega)\vec{E}(\vec{k},\omega) \tag{5-2}$$

Because optical wave-vectors tend to be much smaller than the relevant length scales of optical media (such as the lattice spacing, mean free path, etc), the wave-vector dependence is typically dropped and Equation (5-2) reduces to the standard frequency dependence. In the case of our plasmonic focusing device, the wave-vector becomes so large that the plasmonic wavelength reduces to well below the mean free path. An initial look at this problem would be to simply include the wave-vector dependence, known as spatial dispersion or non-local permittivity, of the permittivity into the dispersion relations, as in reference 101. Unfortunately, these results to not agree with experiment because they only apply to the bulk[63] and do not take the effects of the surface into account. The proximity of free surfaces causes additional electron scattering and fundamentally changes the electron dynamics from those of the bulk medium. Electromagnetic confinement, even in the absence of free surfaces, can present additional losses owing to the anomalous skin effect. This is due to the large spatial gradients of the electric fields near the surface. These fields change at lengths much smaller than the electron's mean free path, as will be explained below. Thus the most immediate effect of large wave-vectors is to increase the small imaginary component of the dielectric constant (ε_m'') of the metal. There is also an effect of large wave-vectors on the real part of the dielectric constant (ε_m') however we expect this effect to be less noticeable than on ε_m''.

Approaches to calculating the non-local dielectric constants at large wave-vectors come in two camps. The first uses quantum mechanical approaches such as the density functional theory and the random phase approximation, typically within the bounds of the jellium model. These approaches are excessively complicated and notoriously inaccurate. They depend so critically on assumed interactions and length scales that even the sign of the slope of the dispersion relations can be qualitatively incorrect. These kinds of analyses are most applicable to the large plasmonic wave-vectors generated in electron energy loss experiments[102] which are much greater than those achieved in our plasmonic focusing structure.

For these reasons, we have chosen a second, semi-classical approach for predicting the relative dielectric constant ε_m at large wave-vectors. The principal effect is on the imaginary component of the permittivity owing to the surface scattering and the anomalous skin effect. The concept of the anomalous skin effect is illustrated in Figure 5-2 and revolves around the mean free path of the electrons. Although this number is seldom referenced for silver, estimates derived from electron mobility put the mean free path between 20nm and 50nm. This number is large compared to both the classical penetration depth into the metal (~25nm for 2.6eV photons) as well as the plasmonic skin depth, which can be made as small as 1.6nm in our geometry. The very large free path of the electrons leads to the anomalous skin effect[77] which can be explained as follows: as the electrons scatter through the positive ionic background in Brownian motion, they can very easily travel outside the reach of the plasmonic skin depth. When they leave the region of the plasmon, they take electromagnetic quiver energy with them. Alternatively, the electrons can collide with the surface which also causes energy loss. Both of these circumstances create a decrease of the effective mean free path[103,104].

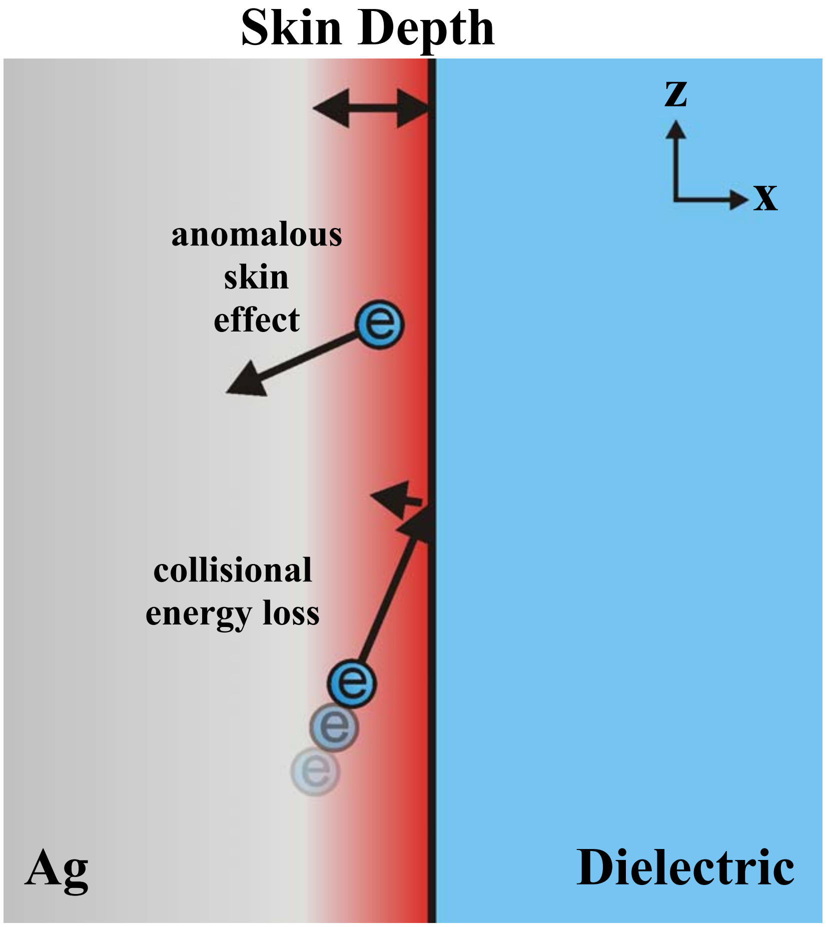

Figure 5-2: Classical electron scattering picture with diffuse reflection from the surface

5.3 A Phenomenological Model for Diffuse Scattering

The field-current relationship explicit in Ohm's law breaks down when the field penetration into the conductor becomes smaller than the mean free path of the electrons. In the case of a surface plasmon, this breakdown can be attributed to two new sources of loss. The first is the collisions with the surface. Historically, surface scattering events tend to be handled with a scalar known as the 'Fuchs parameter' *p*, which designates the percentage of electrons which undergo specular scattering at the surface[105]. The remaining electrons are assumed to undergo diffusive scattering. It is the purpose of this analysis to determine an upper bound on loss due to these processes, so a Fuchs parameter of zero is assumed, thereby all scattering is assumed to be diffuse. When an electron collides with the surface, then, it will lose all of its momentum memory and become a thermalized electron.

In the anomalous skin effect, electrons simply leave the electromagnetic field of the plasmon before undergoing a collision event. When they leave, they take energy from the plasmon with them. Conservation of charge then pulls another thermalized electron into the field region. This creates a process symmetrical with surface scattering with respect to the amount of energy lost.

Collisions with the surface and collisions with an effective boundary at the skin depth of the plasmon replace the energetic electrons with their thermalized counterparts. The half space of metal then acts as a thin film with a thickness equal to the skin depth of the surface plasmon. The scattering events of this effective thin film create a loss mechanism with its own effective electron lifetime much shorter than the bulk momentum relaxation time. This allows us to define a Quality factor[106] (Q_{ASE}) for this process

$$Q_{ASE} \equiv \omega \tau_e \tag{5-3}$$

In Equation (5-3), ω is the frequency of the plasmon, and τ_e is the effective momentum relaxation time due to these additional loss processes. These extra losses will only become significant when the skin depth is much smaller than the mean free path of the electron. From the analysis developed in Chapter 2, we know that this will only occur at large wave-vectors. The skin depth can then be approximated as 1/*k*, where *k* is defined as the plasmon wave-vector.

The effective mean free path for this process may now be determined with one further assumption. As the skin depth grows very small, most of the electrons will be beginning their trajectories from the effective scattering barriers. That is to say, as the effective mean free path of this 'anomalous skin effect' becomes much smaller than the bulk mean free path, the scattering is much more likely at a boundary than at some other point in within the skin depth. We may then calculate the electron mean free path assuming that all 2π Steradians are equally likely for the direction of travel of the thermalized electron.

$$\ell_{mfp} = \int_{\tan^{-1} k\ell_0}^{\pi/2} \frac{1}{k \sin\theta} \cos\theta \, d\theta \qquad (5\text{-}4)$$

The limits of integration are taken from the angle normal to the boundary to a minimum angle such that the bulk mean free path becomes the limiting factor. For most cases of interest, numerical integration gives us a mean path of approximately 2/*k*. The effective lifetime is $2 / \mathrm{v}_F k$ which leads to a *Q* factor:

$$Q_{ASE} = \omega \frac{2}{k\mathrm{v}_F} \qquad (5\text{-}5)$$

where Q_{ASE} is associated with diffuse surface collisions and the anomalous skin effect, while v_F is the Fermi velocity at the surface of the Fermi sphere.

Chapter 2 defined a Quality factor for bulk silver material (Q_{mat}) at large wave-vectors based on the electrodynamics of dispersive media, and the results are tabulated extensively in Appendix A. These two Quality factors may then be combined to yield an effective imaginary component of the relative dielectric constant (ε'').

$$\varepsilon''_{total} = \varepsilon''_0 + \frac{Q_{mat}}{Q_{ASE}} \varepsilon''_0 \tag{5-6}$$

The reader must note that as ε'' becomes large, this creates a change in the skin depth, which changes Q_{ASE}, which again changes the imaginary component of epsilon. To account for this, we use an iterative method, in which the new version of epsilon was put into the dispersion relation, creating a new version of epsilon, and so forth. In all cases this method converged to a solution in less than 10 iterations. The results of these ε'' calculations were then fit to a function of dielectric thickness and used in the simulation of the best-case linear taper described in Chapter 3. To remind the reader, this taper began in a 50nm channel and terminated in a 1nm channel, with a transmission loss of 2.2 dB. With the additional losses from surface collisions and the anomalous skin effect, this loss becomes approximately 4.6dB across the taper, which is a surprisingly favorable result. This is, of course, an upper bound on loss. Even in these extreme conditions, however, these excess loss mechanisms only contribute 2.4dB to the total loss of the device. If the actual loss mechanism were to be found close to this upper bound, the taper could be re-optimized and losses would be even further reduced.

5.4 The Limit of Nano-Focusing

The phenomenological model given above creates a simple way for us to estimate an upper bound on efficient focusing. The calculations in the previous section used a self-consistent iterative method for determining the change in the complex propagation constants due to the anomalous skin effect. It was seen that while these additional losses had a non-zero effect on the real component of the propagation constant *k*, this effect was negligible. It is therefore justified to assume that the real part of *k*, and by extension the properties which depend on *k*, are approximately unchanged by the effects of diffuse surface scattering and the anomalous skin effect.

These assumptions give us the foundation by which we may determine the limit of efficient focusing. In the case of very large losses due to these non-local effects, Q_{ASE} will dominate the intrinsic Q of the bulk material Q_{mat}. The total Q of the metal is then well approximated by Q_{ASE}. We may then use Equation (2-34) for the modal Q (Q_{mod}) from Chapter 2, together with Equation (5-6) to determine Q_{mod} in the limit of extreme anomalous skin effect and surface scattering.

$$Q_{\mathrm{mod}} = Q_{ASE}\left(1+\frac{|\varepsilon'|}{2\varepsilon'' Q_{mat}}\right) \tag{5-7}$$

The terms ε' and ε'' represent the real and imaginary components of the bulk dielectric constant of the metal.

The plasmon oscillation becomes untenable when it dissipates more energy in one optical cycle than 2π times that which is stored at resonance. This is the condition at which $Q_{mod} < 1$. The second term in the brackets is approximately 0.5 in the spectral region of interest, and is between 0.2 and 1.2 across the entire spectrum. The surface plasmon oscillation, therefore, breaks down when the Q_{mod} is equal to one.

$$1 = Q_{\mathrm{mod}} \approx 1.5 Q_{ASE} = \omega \frac{3}{k \mathrm{v}_F} \tag{5-8}$$

Rearranging the terms we have

$$\mathrm{v}_F = 3\frac{\omega}{k} \tag{5-9}$$

Thus it becomes very inefficient to propagate surface plasmons when the phase velocity reduces to one third of the Fermi velocity. We may recast Equation (5-9) with the help of Equations (2-25) and (2-27).

$$\mathrm{v}_F = \mathrm{v}_g \times \frac{3}{M \ln\left(\dfrac{\varepsilon_m - \varepsilon_i}{\varepsilon_m + \varepsilon_i}\right)} \tag{5-10}$$

The quotient in Equation (5-10) is between 2 and 15 across the plasmon spectrum for large wave-vectors. This paints a simple dynamic picture of these loss mechanisms. If the group velocity becomes sufficiently small, the electrons will carry the quiver energy away faster the energy can arrive. At such a point, the oscillation is no longer sustainable and therefore this process limits the achievable wave-vectors and by extension, the minimal spot size.

5.5 An Exact Model for Specular Scattering

The case of specular scattering from the surface cannot be treated in such a simple manner as that of diffuse scattering. For a basic framework for understanding the effect of such behavior on the propagation parameters, we begin with the methodology of

Reuter and Sondheimer[77], used to analyze the anomalous skin effect in the case of the optical response of a metallic surface to normally incident radiation. The strategy is to simultaneously solve Maxwell's Equations (as was done previously on their own) with the linearized Boltzman transport equation given below.

$$\frac{\partial f}{\partial t} - \frac{e}{\hbar} E \bullet \nabla_k f + v \bullet \nabla_r f = -\frac{f - f_0}{\tau} \qquad (5\text{-}11)$$

τ is the electron relaxation time. The term *f* represents the electron distribution function, while f_0 represents the equilibrium electron distribution (the Fermi function). Therefore, $f - f_0$ is equal to the deviation from equilibrium caused by the oscillating plasmon field. If the fields create a small perturbation, we are justified in assuming that these deviations will have the same temporal and spatial distributions as the plasmon itself.

The work of Reuter and Sondheimer is justified, with the realm of its own assumptions, only for optical incidence such that the electric field lies in the plane of the surface. Kliewer and Fuchs[107] extended the theory to the case of non-normal incidence, such that the electric field has components normal to the surface. Because the large wave-vector surface plasmons have electric field components evenly split between the transverse and longitudinal direction, it is this theory which is applicable to the plasmonic case. This extension of the theory for normal incidence is non-trivial. Field components normal to the surface create charge fluctuations which are not effectively screened by the electrons. The reader is reminded that although the Thomas-Fermi screening length is much smaller than the length-scales of interest, it was derived in the zero frequency limit[12]. This concept no longer applies at optical frequencies where $\omega\tau \gg 1$. In this case, the normal electric field creates unscreened charge fluctuations which make $\nabla \bullet E \neq 0$.

This forces us to keep this term which is dropped in the standard formulation and write Maxwell's Equations as

$$\nabla^2 E - \nabla(\nabla \bullet E) + (1+\varepsilon_{IB})\frac{\omega^2}{c^2}E = -i\omega\mu_0 J \tag{5-12}$$

The term ε_{IB} represents the dielectric constant due to interband transitions. With judicious use of Fourier expansions, exploitation of the symmetry implied by specular boundary conditions, and the zero-temperature approximation (which states that f_0=1 for all energies below the local Fermi energy, and zero above it), we arrive at a closed form for the surface impedance.

$$Z = \frac{E_z(x=0-)}{H_y(x=0-)} = \frac{i\omega}{\pi c}\int_{-\infty}^{\infty}\frac{dk_x}{k_x^2+k^2}\left[\frac{k^2}{\left(\omega^2/c^2\right)\varepsilon_l} + \frac{k_x^2}{\left(\omega^2/c^2\right)\varepsilon_t - k_x^2 - k^2}\right] \tag{5-13}$$

In the equation above, k is the plasmonic wave-vector, while k_x represents the Fourier expansion coefficients in the direction normal to the surface. All of the directions are the same as those in Figure 5-2 and follow the standard used throughout this document. The longitudinal (ε_l) and transverse (ε_t) dielectric constants are defined below, where the term K is used as a shorthand for $(k^2 + k_x^2)^{0.5}$, and not as the transverse decay constant as in Chapter 2.

$$\begin{gathered}\varepsilon_t \equiv 1+\varepsilon_{IB} - \frac{3}{2}\frac{\omega_p^2}{\omega^2 + i\,\omega/\tau}\left(\frac{1-i\omega\tau}{\mathrm{v}_F\tau K}\right)^3 \times \\ \left[\frac{\left(\mathrm{v}_F\tau K\right)^2 + \left(1-i\omega\tau\right)^2}{2i\left(1-i\omega\tau\right)^2}\ln\left(\frac{\left(1-i\omega\tau\right)+i\mathrm{v}_F\tau K}{\left(1-i\omega\tau\right)+i\mathrm{v}_F\tau K}\right) - \frac{\mathrm{v}_F\tau K}{1-i\omega\tau}\right]\end{gathered} \tag{5-14}$$

$$\varepsilon_l \equiv 1+\varepsilon_{IB}+\frac{i3\omega_p^2}{\omega\tau\ +i}\left(\frac{1-i\omega\tau}{\mathrm{v}_F K}\right)^2 \times$$
$$\left\{\frac{\mathrm{v}_F K}{1-i\omega\tau}-\frac{1}{2i}\ln\left(\frac{1-i\omega\tau+i\mathrm{v}_F\tau K}{1-i\omega\tau+i\mathrm{v}_F\tau K}\right)\right\}\Bigg/\left\{\mathrm{v}_F\tau K-\frac{1}{2i}\ln\left(\frac{1-i\omega\tau+i\mathrm{v}_F\tau K}{1-i\omega\tau+i\mathrm{v}_F\tau K}\right)\right\} \tag{5-15}$$

These equations were derived to determine the reflectivity of metals under non-normal incidence. The surface impedance, however, is exactly what is needed to calculate the dispersion relations of the MIM plasmon when the electrons scatter from the surface specularly. As the spacing (*d*) in the MIM plasmons becomes very small, the dielectric still tends to act with its bulk dielectric constant. The bound electrons of the dielectric, of course, will not undergo extraneous scattering events due to the change in wave-vector. The boundary conditions derived from Maxwell's Equations tell us that E_z and H_y are continuous across the boundary. Because the surface impedance has been defined as the ratio of these quantities, then it must be continuous as well. Returning to the standard plasmon relations and assuming exponential decay of the fields in the dielectric, the surface impedance must be

$$Z=\frac{E_z(x=0+)}{H_y(x=0+)}=\frac{-i\left(k^2-{}^{\varepsilon_d\omega^2}\!\big/\!{}_{c^2}\right)^{1/2}}{\omega\varepsilon_d\varepsilon_0}\,\frac{1-e^{d\left(k^2-{}^{\varepsilon_d\omega^2}\!/\!{}_{c^2}\right)^{1/2}}}{1+e^{d\left(k^2-{}^{\varepsilon_d\omega^2}\!/\!{}_{c^2}\right)^{1/2}}} \tag{5-16}$$

The plasmon propagation parameters may then be determined numerically by finding the real and imaginary components of *k* which equate Equation (5-16) and Equation (5-13). It is precisely the crude minimization routines which were used to determine the dispersion relations of Chapter 2 which are necessary to solve these more complicated equations. There is still one piece of information necessary before we can turn the numerical crank on this problem. Equations (5-15) and (5-14) describe the silver in terms of a Drude metal with additional contributions from interband transitions. Fortunately, the exact physical picture for silver is a Drude metal with a plasma frequency of approximately 9eV whose character is drastically changed by the onset of interband transitions near 3.9eV, as is a similar case for all of the coinage metals[108]. To complete our numerical calculations with any accuracy, this information was used in conjunction with the experimentally derived dielectric constants of silver to solve for the necessary parameters. It must be noted that the contribution to the dielectric constant due to interband transitions in a function of frequency and must be treated as such.

The results of these calculations for the Ag-SiO_2-Ag geometry are plotted below. Figure 5-3 shows the change in decay length due to the calculations described in this section (the dotted line) compared to those simply using the bulk approximation for the dielectric constant of silver (the solid lines). All curves are for constant energy input photons. Note that the change in decay length is very small. Because this increased loss is almost imperceptible, there is little sense in using these numbers in another electromagnetic simulation to determine the effect of specular scattering on the ideal taper. The throughput efficiency of the 30° taper would be nearly the same as in the bulk approximation.

These results also give substance to our claim in Section 1.5 that Landau damping can be ignored in these problems. Landau's original discovery of this damping phenomenon came about because he treated the evolution of plasma oscillations as initial value problems in a similar electron transport model and allowed the propagation parameters to be complex, even in the case of a collisionless plasma. Note that in our case, we also allowed for complex propagation parameters. If Landau damping were to be significant it would have appeared in these results.

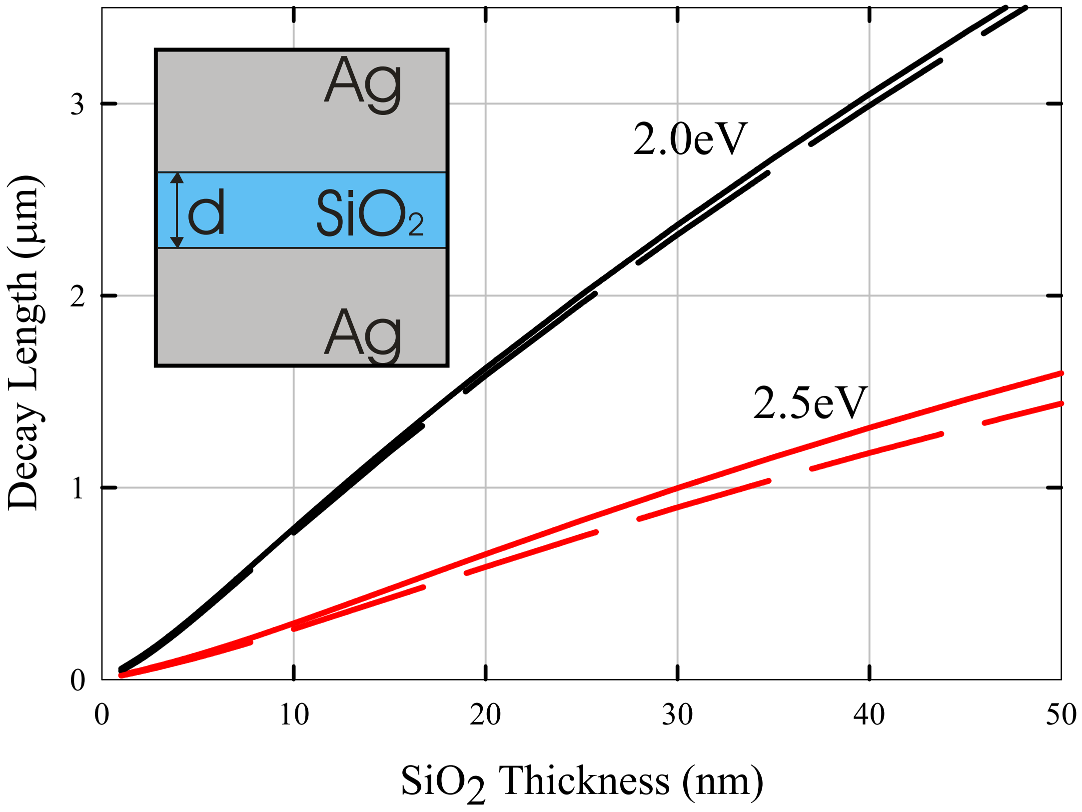

Figure 5-3: Decrease in the plasmonic decay length due to the accounting of the electron densities and specular scattering at the interface. The solid line denotes the use of the bulk dielectric constant, and the dashed line represents the electron behavior under the Boltzmann transport equation

Strictly examining loss does not tell the entire story. Figure 5-4 illustrates the dispersion relations using the techniques described above. Again the solid line shows the bulk approximation and the dashed lines show the calculations which take electron dynamics into effect. A comparison of these plots yields an unexpected result: the specular scattering and electron dynamics yield a reduced wave-vector. More pronounced than the change in decay length, this reduction in wave-vector helps to explain why the loss changes much less than expected. The reduced wave-vector creates a larger group velocity. This increased group velocity reduces the interaction time of the field with the loss mechanisms of the metal, thereby increasing the decay length. The downside to this is that it was the slow group velocity and large wave-vector that made this plasmonic lens so powerful! A reduction in these properties will reduce the overall enhancement factor. Because loss and enhancement are so intertwined with the plasmonic lens, the cutting corners in one tends to cut corners with the other.

This chapter has presented two limiting cases of electron scattering and its effects on MIM surface plasmons. As has been borne out with low frequency experiments, the electron scattering at an interface tends to be some combination of diffuse and specular scattering[109]. The calculations undertaken in this chapter have demonstrated that even in the worst case of completely diffuse scattering, the change in throughput of the taper geometry will only suffer by a few dB of loss. While not insignificant compared to absorption and scattering losses, these numbers do not undermine the overall efficiency of the design and they do uphold the notion that a rapid taper is an efficient transition from the micro-scale to the nanoscale.

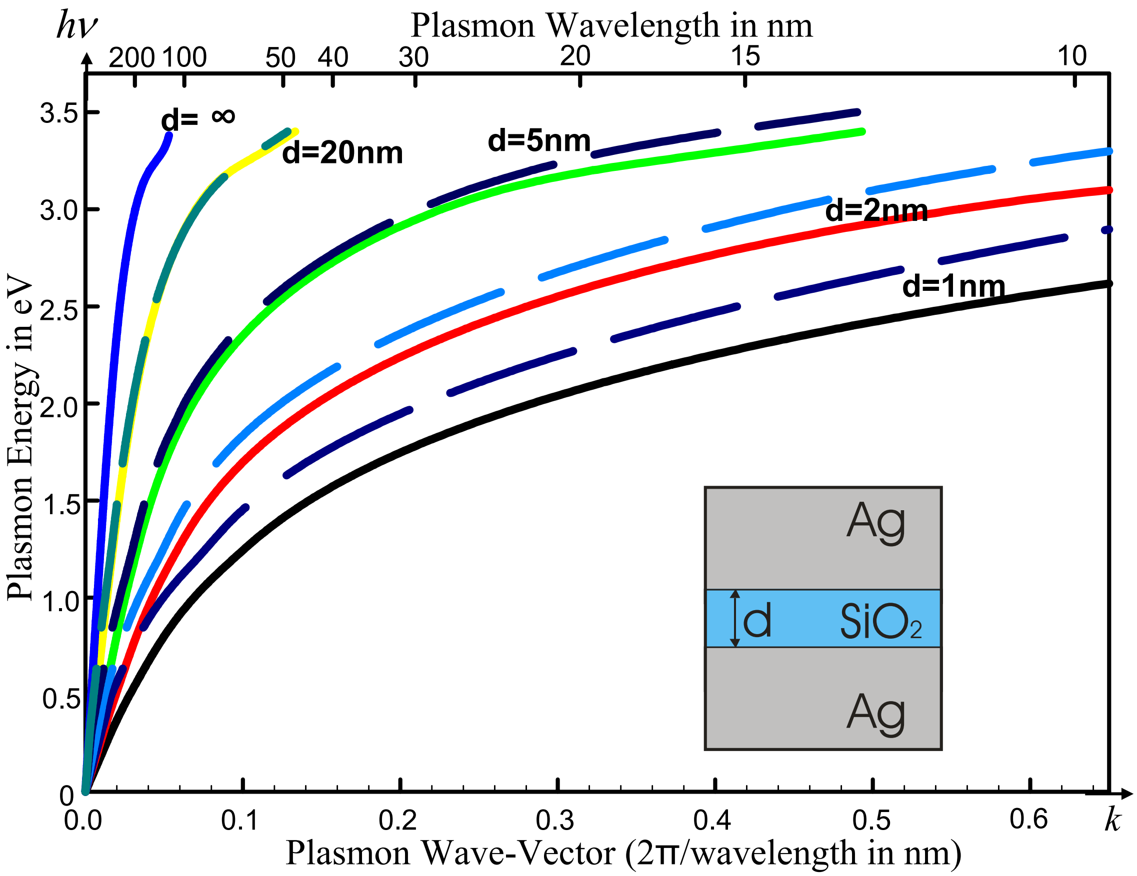

Figure 5-4: Dispersion relation comparing the bulk approximation (solid lines) to the calculation using the Boltzmann transport equation with specular scattering at the interface (dashed lines)

CHAPTER 6 THE FUTURE OF THE PLASMONIC LENS

It's a poor sort of memory that only works backwards.

-The Queen in Lewis Carroll's *Through the Looking Glass*

This thesis has demonstrated, through both analysis and numerical simulations, a plasmonic focusing scheme which can couple the large single-sided plasmon mode into the tightly focused MIM mode with only 5.5 dB of loss. If we include the full effects of the anomalous skin effect with diffuse electron scattering at the interface as well as 3dB of loss at the in-coupler (be it grating or end-fire), this yields a total loss of only 12dB. Even assuming the worst case electron scattering losses, our device has such astonishingly low loss even when focusing from a 1μm^2 spot of a microscope objective down to a 3nm by 7nm spot at the focus of the plasmonic lens. The promise of this technology is clearly ahead of the state of the art in tapered fiber probes which have approximately 30dB of loss in focusing to a 100nm diameter spot.

6.1 Experiment and Fabrication

The next step in the development of the plasmonic lens is experimental verification of these simulations. Such a plan has entails several serious fabrication challenges. To date, gratings have been fabricated and tested, as shown in Figure 6-1. Gratings were prepared by depositing 40nm of SiO_2 onto a glass slide. Electron beam lithography and dry etching were then used to create several straight gratings of various periods on the SiO_2. This step was followed by electron beam evaporation of silver onto the grating.

Evaluation of the various gratings was then achieved by characterizing the reflectance of monochromatic light at various linear polarizations. The normally incident illumination was from a fiber-coupled Kr-Ar laser operating at 488nm. The introduction of the fiber produced light of a random polarization. This output polarization was found to be very steady over time and used to the advantage of the experiment. The optical field which is polarized in the y-direction will not generate surface plasmons when illuminating a grating that has translational symmetry in that direction. This polarization was therefore used as a control beam and corrected for local changes in reflectance due to surface imperfections. The reflectivity of the beam of correct polarization and that of the control beam were measured at normal incidence to the grating and the ratio of the two is plotted for each grating period. Note the large dip in reflectance at the 280nm grating period, exactly where plasmons were expected from the simple dispersion relations. This demonstrates that gratings can be effectively fabricated for this device. In addition to the grating, the tapered dimple lens has also been successfully fabricated by using a de-focused electron beam to create the cylindrically symmetric exposure. After development and subsequent SEM exposure, the proper taper angle was created on an acceptably smooth surface. It now remains for the UCLA plasmonics team to put these pieces together and create an output facet so that the near field can be interrogated and measured.

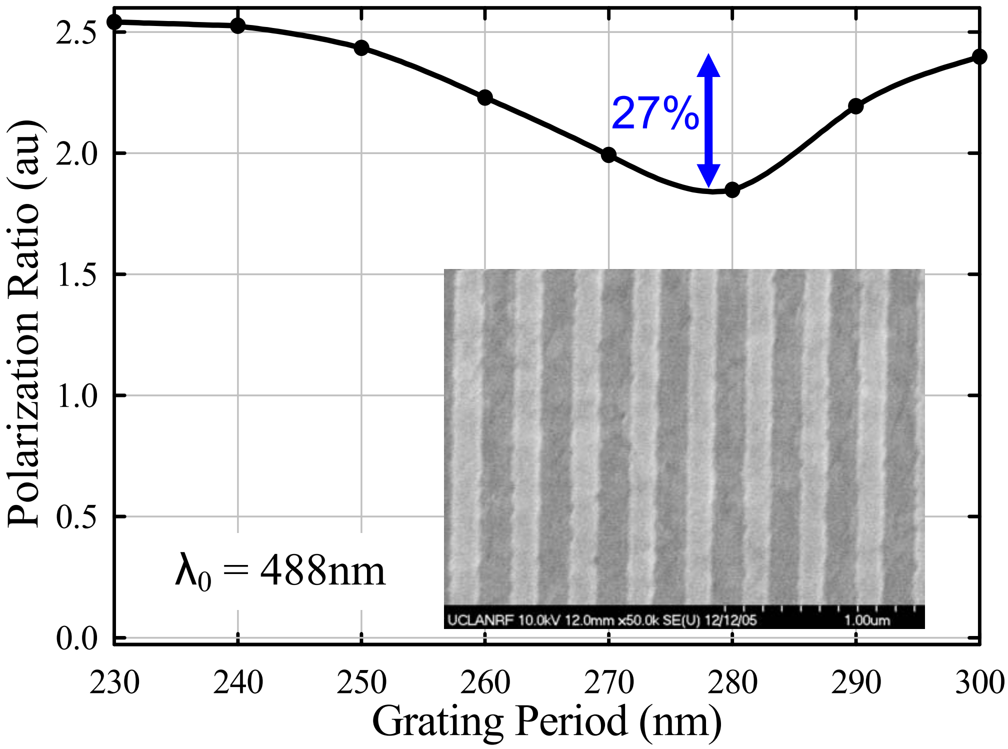

Figure 6-1: Plot of the reflection ratio of ths s to p polarization of light normally incident on gratings of verious periods. The inset shows an SEM image of one such silver grating.

6.2 Applications

Once the device is demonstrated, the applications are many and varied. The obvious range of applications begins with displacing all of the uses of the tapered fiber probe. With the plasmonic lens's increased throughput and greatly decreased spot size, there is no question as to which is the superior technology. There are a vast number of applications for tapered fiber probes which will immediately be advanced with the use of our device. From Near-field Scanning Optical Microscopy (NSOM) and optical lithography, to near-field optical memory storage, a significant breakthrough in efficiency will enable all of these applications. For a more complete list of biological and chemical applications, the reader is referred to Reference 49.

In addition to merely making an improved version of the tapered fiber probe, the plasmonic dimple lens will also enable an entire suite of new applications. The huge field enhancements can be used to achieve non-linear response from the dielectric material at low input powers. In the case of the plasmonic dimple lens described in the body of this thesis, the dielectric material is SiO_2. This is a symmetric molecule, so the second order susceptibility is zero[2]. Third order effects, however, are routinely seen in SiO_2 and are dominated by non-linear refraction. An increase in index of the insulator material can have dramatic effects on the plasmonic dispersion relations by down shifting the frequency at which k goes to infinity. By engineering the input powers and frequencies, this could be used to create an optically controlled optical delay line. This effect could also increase the dielectric constant so much as to push the plasma frequency below that of the optical beam. It could thereby make for an optical logic element or modulator. Such intense optical fields have also been shown to enhance electron tunneling across the dielectric gap of the MIM structure[110] or to generate hot electrons from the focus. Finally, there has been interest in these devices to compress the optical spot size a detector. Allowing for a much smaller detector area, this would greatly reduce dark current and therefore enable higher sensitivity.

6.3 Heat Assisted Magnetic Recording

In addition to the applications listed above, the plasmonic lens has the opportunity to make a large impact on future generations of hard disk technology. The need for focused energy comes about because standard hard disk media become unstable when the domains are made sufficiently small, an effect known as super paramagnetism. This means that the next generation will need more magnetically rigid media, however these would require untenable magnetic fields from the drive heads to write the bits. The solution to this comes in the form of directed light. A focused optical beam can locally heat the volume of the bit making it easier to re-write. By focusing an optical beam only onto the bit that is to be written, it dramatically lowers the requisite field of the write head. As the medium cools, it then stabilizes the data[111]. This is known in the industry as Heat Assisted Magnetic Recording (HAMR).

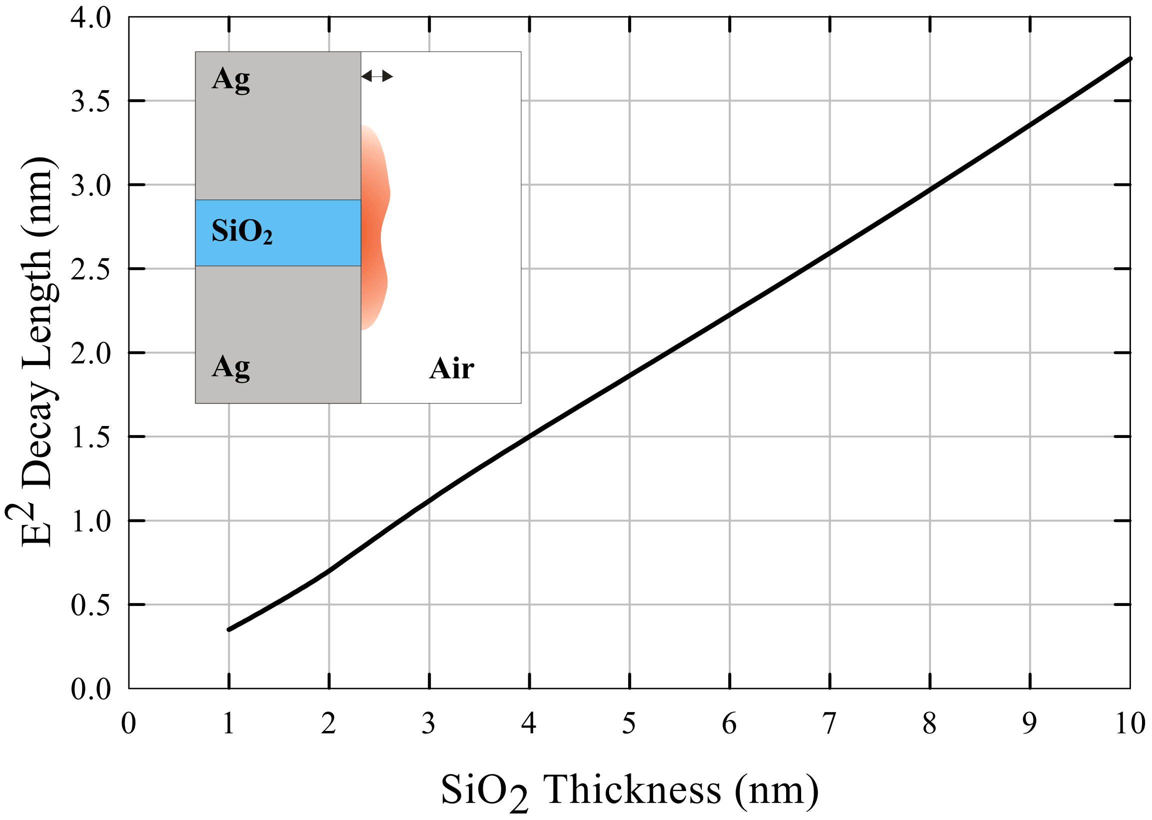

Figure 6-2: The decay length of the near field at the output facet of the plasmonic lens.

Although the plasmonic lens has been shown to efficiently focus light, the trick is getting the optical field out of the slab mode plasmons. Modern hard disks read and write by using the magnetic near-field of a magnetic dipole which requires the head to float tens of nanometers above the disk. The plasmonic lens likewise produces an AC electric dipole which couples only to the optical near field. Figure 6-2 illustrates the decay length of the near field for 2.6eV plasmons at various SiO$_2$ thicknesses. Because this decay length is non-exponential, we have defined it as the length normal to the out-coupling surface, at which the optical energy density has decayed by 1/*e*. For the 1nm terminal thickness described throughout this text, the plasmonic energy decays in just 0.35nm outside of the device. Intuitively, this is expected because the MIM geometry acts as a parallel plate capacitor, with energy only out-coupling through the fringing fields.

While the standard plasmonic lens will not exactly fit this application, there is a solution. The HAMR technique requires that optical energy be deposited in a thin film conductor, typically cobalt, which acts as a transducer changing the light to heat. Simulations using our 30° taper with a 10nm terminal thickness and a 10nm air gap to the cobalt showed only 10% efficiency in energy transfer. When the MIM geometry was changed to the converse IMI scheme, this number increased to 28%. Conceptually, the IMI technique should yield an improved throughput because instead of a capacitor, it creates an oscillating charge at the tip. This creates image charges[112] in the cobalt, which greatly facilitates the energy transfer. This is illustrated in Figure 6-3. Optimization of the plasmonic focusing geometry for the HAMR is an ongoing application and further developments are expected in the near term.

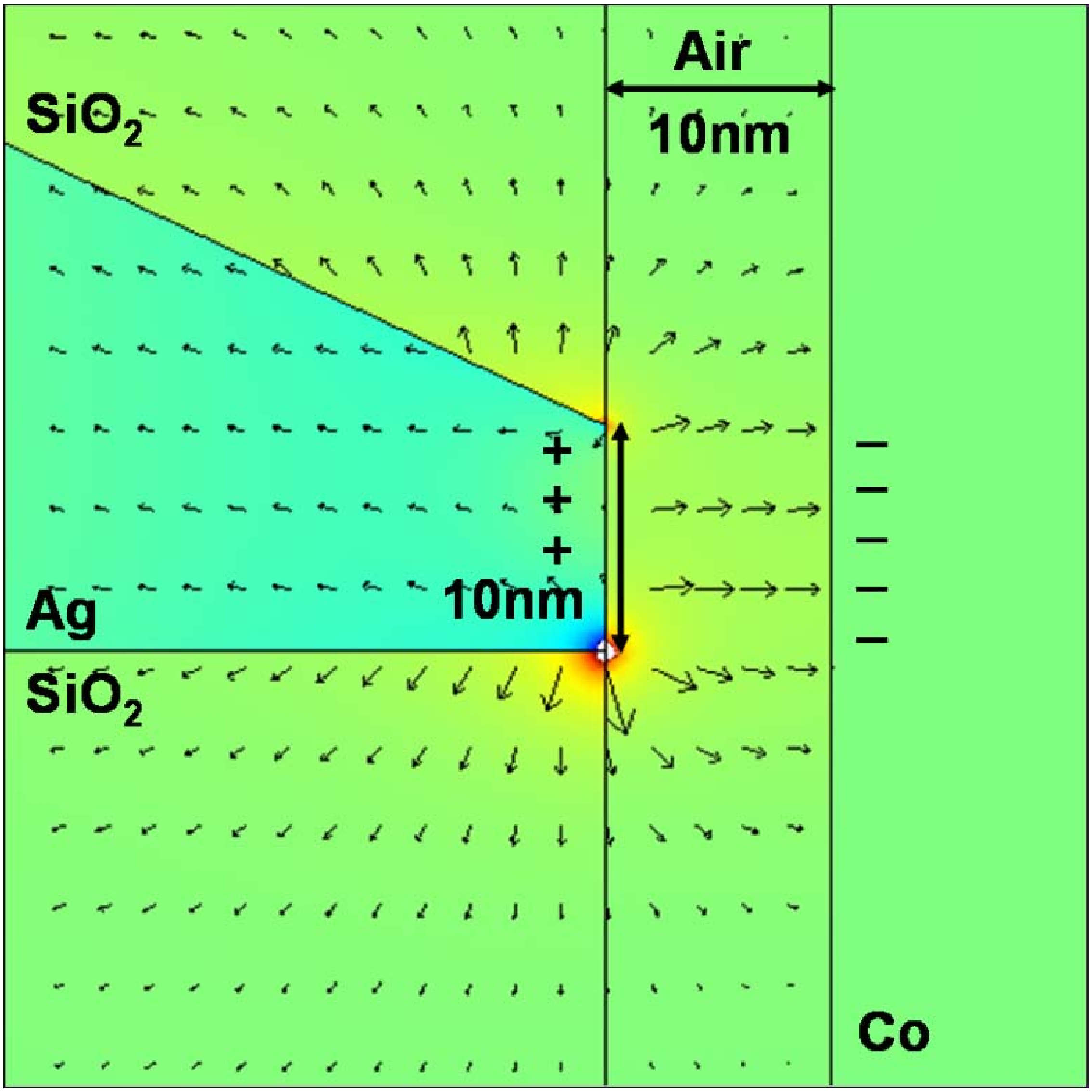

Figure 6-3: Simulation results of the IMI focusing scheme for HAMR. The arrows indicate direction and strength of the electric field and the color designates total energy density

6.4 Conclusions

This thesis has provided a first step. It has generated a feasible plan for focusing to the nanoscale, and designed the materials and processes to achieve this plan. We have identified and computed the dominant losses and analyzed the device for several applications. It is now up to the next student to put these concepts into practice. There is such vast potential in the plasmonic lens but it only depends on adequate fabrication tools to realize it.

Appendix A The Optical Constants of Silver

ħω (eV)	ε'	ε"	d(ωε ')/dω	Q_{mat}	Re[ρ(Ω cm)]	Im[ρ(Ω cm)]
0.2	-1623.42	418.964	1311.38	1.56503	5.54E-06	-2.15E-05
0.4	-438.142	61.5077	436.758	3.55043	5.82E-06	-4.16E-05
0.6	-196.065	20.1764	170.145	4.21645	6.38E-06	-6.23E-05
0.8	-116.129	9.00827	100.231	5.56326	6.08E-06	-7.90E-05
1	-75.0013	4.00022	79.8387	9.9793	5.14E-06	-9.77E-05
1.2	-51.0708	1.81331	55.1952	15.2194	4.15E-06	-1.19E-04
1.4	-37.2903	1.26983	42.8527	16.8734	4.60E-06	-1.39E-04
1.6	-27.5713	0.934328	38.0527	20.3636	5.32E-06	-1.63E-04
1.8	-20.5736	0.67703	32.7334	24.1743	6.01E-06	-1.92E-04
2	-15.505	0.497701	27.555	27.6823	6.80E-06	-2.25E-04
2.2	-11.805	0.381254	22.955	30.1046	7.86E-06	-2.64E-04
2.4	-9.07569	0.312172	19.0739	30.5504	9.53E-06	-3.08E-04
2.6	-7.03494	0.27778	15.9582	28.7245	1.23E-05	-3.56E-04
2.8	-5.48267	0.268454	13.5489	25.2351	1.70E-05	-4.10E-04
3	-4.27676	0.277045	11.7927	21.2831	2.46E-05	-4.69E-04
3.2	-3.21096	0.3172	12.8114	20.1946	4.14E-05	-5.50E-04
3.4	-2.20801	0.37474	14.9484	19.945	7.87E-05	-6.74E-04
3.6	-1.18101	0.429287	17.8648	20.8075	1.80E-04	-9.13E-04
3.8	-0.007865	0.496733	15.1258	15.2253	7.71E-04	-1.56E-03

Table A-1: The relevant optical constants of silver. The primes denote the real component and double primes the imaginary component of ε.

This appendix details the material properties of silver so that the reader is not required to return to the literature in order to make any detailed plasmonic calculations on their own. The information in Table A-1 quantifies the data points derived from a spline fit of experimentally measured data. These empirical values of the real and imaginary part of the dielectric constant are given in Figure A-1 and Figure A-2 respectively. Figure A-3 illustrates a larger view of the material *Q*-factor of silver derived from the methods outlined in Chapter 2. Finally, Figure A-4 is a plot of ${d\left(\omega\varepsilon'\right)}\big/{d\omega}$ versus frequency. This term replaces ε' in the standard relation for electrostatic energy density:

$$U = \frac{1}{2}\varepsilon' E^2 \tag{A-1}$$

In dispersive media, and especially in the case of good conductors, the tenets of basic thermodynamics require that:

$$U = \frac{1}{2}\frac{d\left(\omega\varepsilon'\right)}{d\omega}E^2 \tag{A-2}$$

As shown in Chapter 2, these relations allow us to define the material *Q* (Q_{mat}) as

$$Q_{mat} = \frac{\dfrac{\partial(\omega\varepsilon')}{\partial\omega}}{2\varepsilon''} \tag{A-3}$$

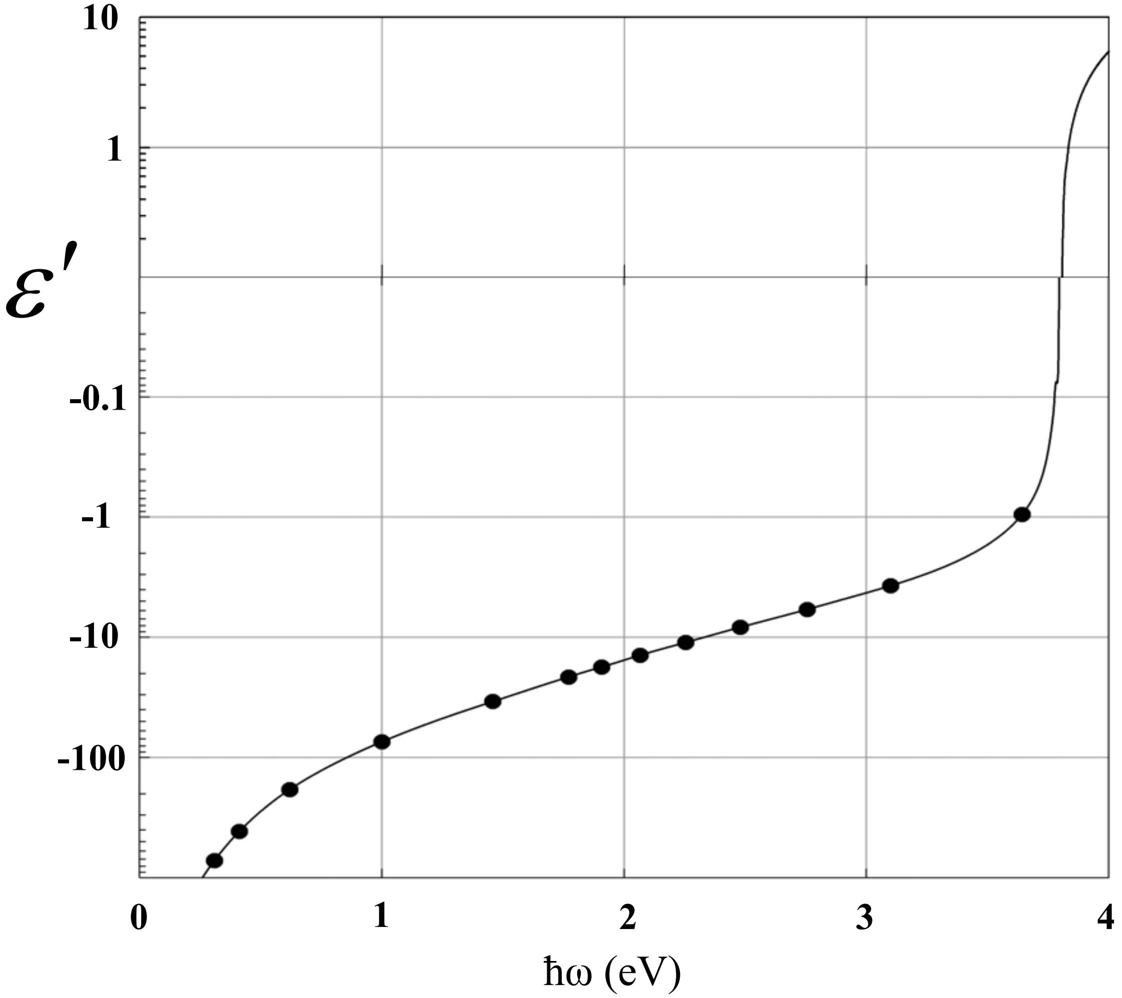

Figure A-1: Empirically determined real component of ε versus photon energy

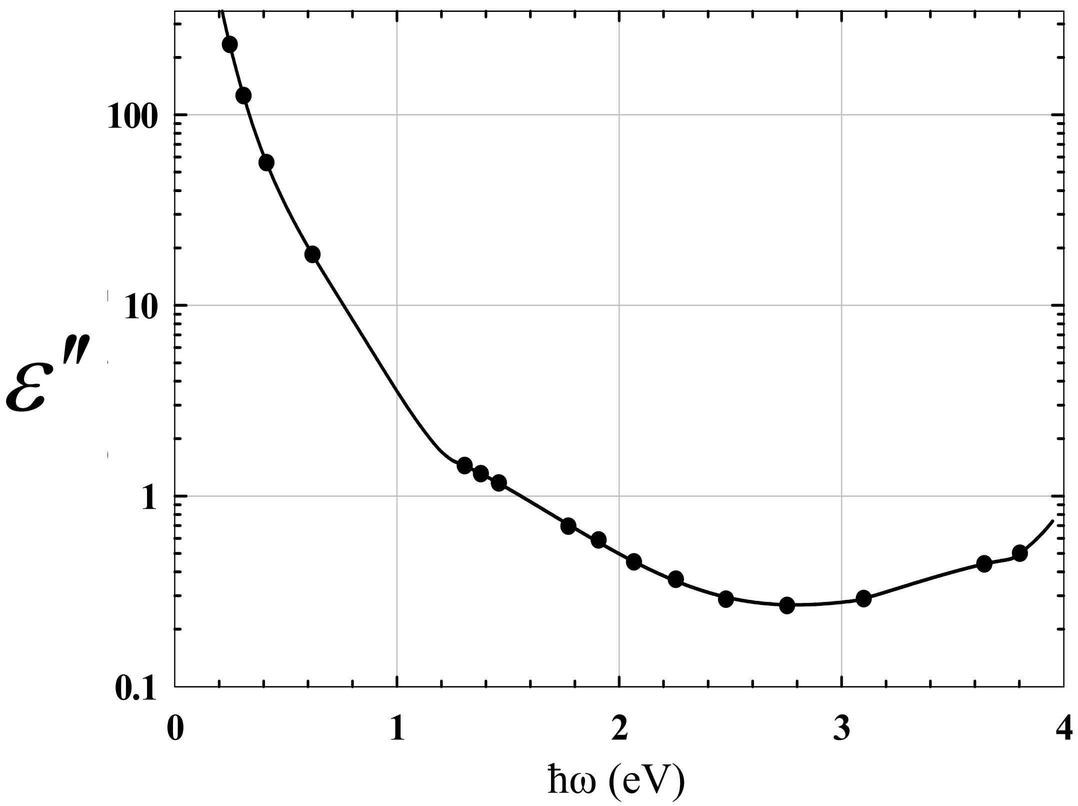

Figure A-2: Empirically determined imaginary component of ε versus photon energy

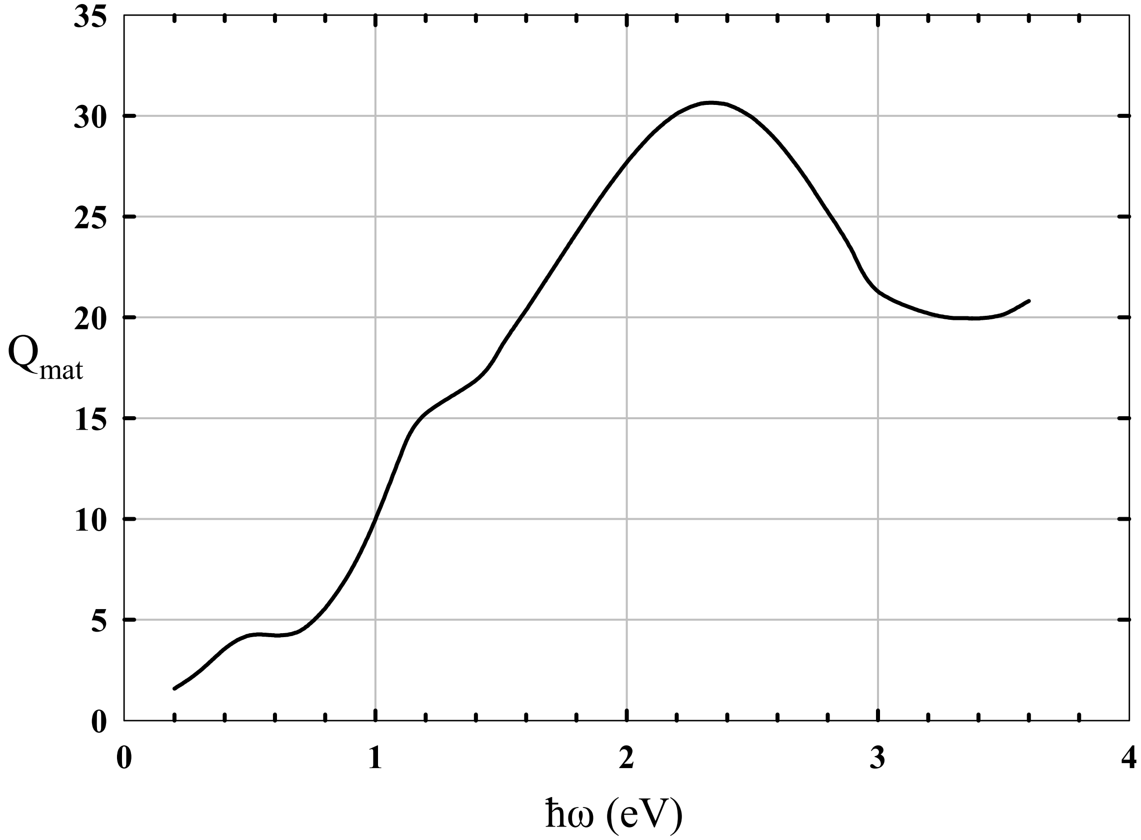

Figure A-3: Material *Q_{mat}* of silver

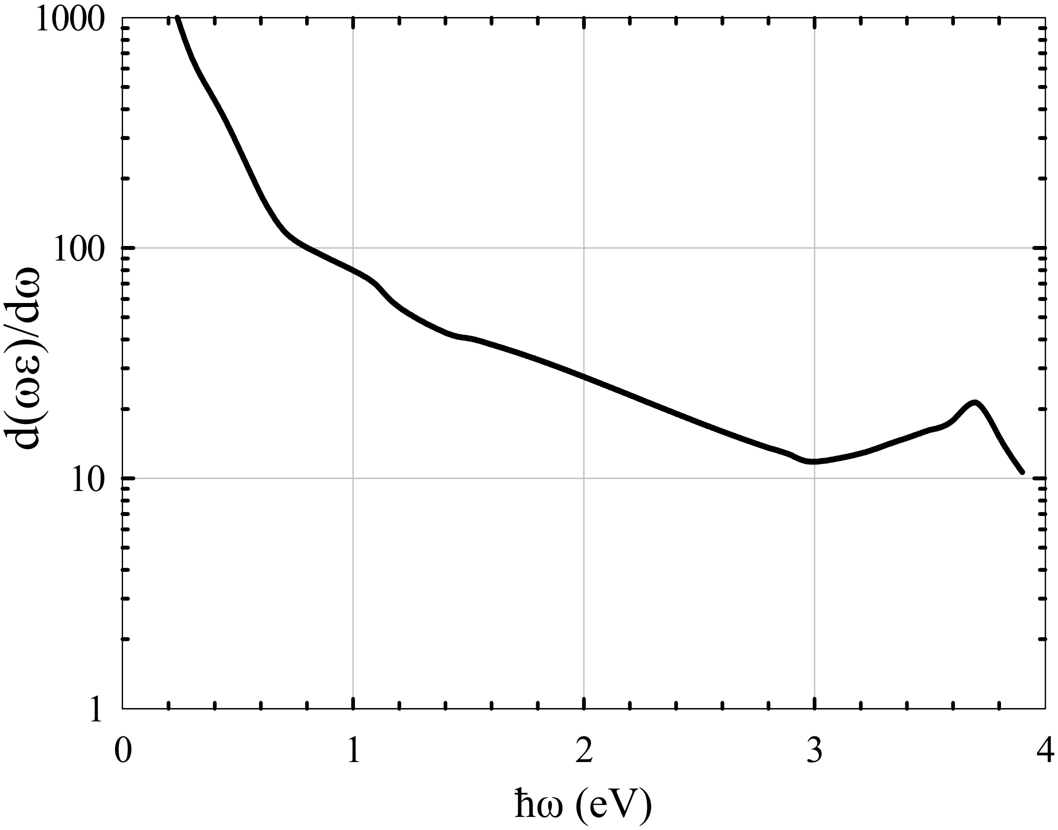

Figure A-4: Plot of the differential dielectric constant of silver which is used in the determination of the energy contained in the field

Appendix B Sample 2D FDTD Code written in C

```
FD1D_3.2.c    2D TM simulation PML  */
/* dx/dt = 2*c */
/* 2.5 eV photons */

# include <math.h>
# include <stdlib.h>
# include <stdio.h>
#define NR_END 1
#define FREE_ARG char*

double **dmatrix(long, long, long, long);

#define IE  400
#define JE  400

main ()
{
  double **hz, **dx, **dy;
  double **ex, **ey, **ix, **iy;
  double **sx, **sy;
  float dummy1[JE], dummy2[JE], dummy3[JE];
  int l,n,i,j,ic,jc,nsteps, npml, npml1, lim1, lim2, switch1;
  float ddx, dt, T, epsz, pi, epsilon, sigma, eaf, ddx2, B1, B2, C1;
  float xn, xxn, xnum, xd, curl_e, curlh, gamma1, gamma2, gamma3, ddd;
  float t0, pulse, w0, chi0, dchi0, wp2, ww, krl, epss, epsag;
  float sigeps, chi1, photonenergy, www, kshft, indexs;
  float gi1[IE], gi2[IE], gi3[IE];
  float gj1[JE], gj2[JE], gj3[JE];
  float fi1[IE], fi2[IE], fi3[IE];
  float fj1[JE], fj2[JE], fj3[JE];
  double **idx, **idy;
  float pulseback, pulseey, factor1, factor3, pulseex;
  FILE *fp, *fopen();
  FILE *fp1, *fp2;

  hz=dmatrix(0,IE-1,0,JE-1);
  dx=dmatrix(0,IE-1,0,JE-1);
  dy=dmatrix(0,IE-1,0,JE-1);
  sx=dmatrix(0,IE-1,0,JE-1);
  sy=dmatrix(0,IE-1,0,JE-1);
  ex=dmatrix(0,IE-1,0,JE-1);
  ey=dmatrix(0,IE-1,0,JE-1);
  ix=dmatrix(0,IE-1,0,JE-1);
  iy=dmatrix(0,IE-1,0,JE-1);
  idx=dmatrix(0,IE-1,0,JE-1);
  idy=dmatrix(0,IE-1,0,JE-1);
  ic= IE/2;
  jc= JE/2;
  lim1=220;
```

```
lim2 = 230;
ddx = 0.000000002e14;       /* Cell size */
dt = ddx/6e8;               /* Time steps */
ddx2 = ddx*1e-5;
epsz = 8.8e-12;
pi = 3.14159;
w0 = 1.193;
ww = 2.5;              /* photon energy (eV) */
www = ww*15.2013;     /* photon angular freq * 10^-14 */
chi0 = 10942*dt - 9172*(1- exp(-1.193*dt));
dchi0 = -11319*pow(1-exp(1.193*dt),2);
wp2 = 13054;
t0 = -1.193;
krl = 7.30102;
epss = 3.14947;
indexs = sqrt(epss);
kshft =  krl*0.00506708*ddx2;
epsag = -8.0315;
ddd = (lim2-lim1)*ddx2;
gamma1 = sqrt(krl*krl - epss*ww*ww) / 197.35;
gamma2 = sqrt(krl*krl - epsag*ww*ww) / 197.35;
gamma3 = sqrt(krl*krl - ww*ww)/ 197.35;
B1 = 0.5 * ((epss/epsag) + (gamma1/gamma2));
B2 = 0.5 * ((epss/epsag) - (gamma1/gamma2));
C1 = epsag*(B1*exp((gamma3+gamma2)*ddd)+B2*exp((gamma3-gamma2)*ddd));
sigeps = t0*13054.;
chi1 = -1.*t0*t0*13052.;
factor1= exp(-gamma1*ddx2);
factor3= exp(-gamma3*ddx2);

/* initialize matricies */
for ( j=0; j < JE; j++) {
  /* printf( "%2d   ", j);       */
  for ( i=0; i< IE; i++ ) {
    dx[i][j] = 0. ;
    idx[i][j] = 0. ;
    dy[i][j] = 0. ;
    idy[i][j] = 0. ;
    ex[i][j] = 0.;
    ey[i][j] = 0.;
    hz[i][j] = 0.;
    ix[i][j] = 0.;
    iy[i][j] = 0.;
    sx[i][j] = 0.;
    sy[i][j] = 0.;
  /*  printf( "%5.2f ", ga[i][j]);     */
  }
  /* printf( " \n");  */
}

/* Calculate the PML Parameters */
 for (i=0; i<IE; i++ ) {
  gi1[i] = 0.0;
```

```
 gi2[i] = 1.0;
 gi3[i] = 1.0;
 fi1[i] = 0.0;
 fi2[i] = 1.0;
 fi3[i] = 1.0;
}
for(j=0; j< JE; j++) {
 dummy1[j] = 0.0;
 dummy2[j] = 0.0;
 dummy3[j] = 0.0;
 gj1[j] = 0.0;
 gj2[j] = 1.0;
 gj3[j] = 1.0;
 fj1[j] = 0.0;
 fj2[j] = 1.0;
 fj3[j] = 1.0;
}

printf( "Number of PML vert cells --> ");
scanf("%d", &npml);
printf( "Number of PML horizontal cells --> ");
scanf("%d", &npml1);

for( i= 0; i<= npml1; i++) {
 /* xnum = npml - i; */
 xnum = npml1 - i;
 xd = npml1+0.5 ;
 xxn = xnum/xd;
 xn = 0.1*pow(xxn, 2.0);
 /* printf(" %d %7.4f %7.4f \n", i,xxn,xn); */
 /* gi1[i] = xn; */
 gi1[IE-1-i] = xn;
 /* gi2[i] = 1.0/(1.0 + xn); */
 gi2[IE-1-i] = 1.0/ (1.0 + xn);
 /* gi3[i] = (1.0 - xn)/(1.0+ xn); */
 gi3[IE-i-1] = (1.0 - xn)/(1.0+ xn);
 /* printf(" %d %f %f %f\n", IE-1-i,gi1[IE-1-i],gi2[IE-1-i],gi3[IE-1-i]); */
}
for( i= 0; i<= npml1; i++) {
 xnum = npml1 - i + 0.5;
 xd = npml1+0.5 ;
 xxn = xnum/xd;
 xn = 0.1*pow(xxn, 2.0);
 /* fi1[i] = xn; */
 fi1[IE-1-i] = xn;
 /* fi2[i] = 1.0/(1.0 +xn); */
 fi2[IE-1-i] = 1.0/(1.0 +xn);
 /* fi3[i] = (1.0 - xn)/(1.0+xn); */
 fi3[IE-1-i] = (1.0 - xn)/(1.0+xn);
 /* printf(" %d %f %f %f\n", IE-1-i,fi1[IE-1-i],fi2[IE-1-i],fi3[IE-1-i]);  */
}

for(j=0; j<= npml; j++) {
```

```
   xnum = npml -j;
   xd = npml+0.5;
   xxn = xnum/xd;
   xn = 0.33*pow(xxn, 3.0);
   /* printf(" %d %7.4f  %7.4f \n", i, xxn,xn); */
   gj1[j] = xn;
   fj1[JE-j-1] = xn;
   gj2[j] = 1.0 / (1.0 + xn);
   fj2[JE-j-1] = 1.0 / (1.0 + xn);
   gj3[j] = (1.0 - xn)/(1.0 + xn);
   fj3[JE-j-1] = (1.0 - xn)/(1.0 + xn);
  }
  for(j=0; j< npml; j++) {
   xnum = npml -j+0.5;
   xd = npml+0.5;
   xxn = (xnum)/xd;
   xn = 0.33*pow(xxn, 3.0);
   fj1[j] = xn;
   gj1[JE-1-j] = xn;
   fj2[j] = 1.0/(1.0+xn);
   gj2[JE-1-j] = 1.0/(1.0+xn);
   fj3[j] = (1.0-xn)/(1.0 +xn);
   gj3[JE-1-j] = (1.0-xn)/(1.0 +xn);
  }

  /* printf("gi + fi \n");
  for(i=0; i<IE; i++) {
   printf( "%2d   %f   %5.2f   %5.2f \n", i, gi1[i], gi2[i], gi3[i]);
   printf( "      %5.2f   %5.2f   %5.2f \n", fi1[i], fi2[i], fi3[i]);
  }         */

  /* printf("gj + fj \n");
  for(j=0; j<JE; j++) {
   printf( "%2d   %5.2f   %5.2f \n", j, gj2[j], gj3[j]);
   printf( "      %5.2f   %5.2f   %5.2f \n", fj1[j], fj2[j], fj3[j]);
  }       */

 /* t0 = 20.0;       */
 T = 0;
 nsteps = 1;

 /* initialize hard source input spatial function */
 /* dummy1 is for Hz, dummy2 is for Ey */
for(j=npml;j<JE-npml;j++) {
 dummy1[j] = 1;
 dummy2[j] = 1;
 dummy2[j] = 1;
}
 /* for(j=npml+1; j < lim1;j++) {
      dummy1[j] = epss*exp(gamma1*(j-lim1)*ddx2);
      dummy2[j] = dummy1[j]*krl/(ww*epss);
      dummy3[j] = -gamma1*epss*exp(gamma1*(j-lim1-0.5)*ddx2)*197.35/krl;
 }
```

```
dummy3[lim1] =-gamma1*epss*exp(-0.5*gamma1*ddx2)*197.35/krl;

for(j=lim1; j <= lim2; j++) {
     dummy1[j] = epsag*(B1 * exp(gamma2*(j-lim1)*ddx2) +
       B2*exp(-gamma2*(j-lim1)*ddx2));
     dummy2[j] = dummy1[j]*krl/(ww*epsag);
     if(j>lim1)
            dummy3[j] = -epsag*gamma2*197.35*(B1 * exp(gamma2*
            (j-lim1-0.5)*ddx2)
            -B2*exp(-gamma2*(j-lim1-0.5)*ddx2))/krl;
}
for(j = lim2+1; j < JE -npml; j++) {
     dummy1[j] = C1*exp(-gamma3*(j-lim1)*ddx2);
     dummy2[j] = dummy1[j]*krl/ww;
     dummy3[j] = C1*exp(-gamma3*(j-lim1-0.5)*ddx2)*gamma3*197.35/krl;
}          */
switch1 = 0;

while (nsteps >0) {
  printf( "nsteps --> ");
  scanf("%d", &nsteps);
  printf("%d \n", nsteps);

  for ( n=1; n <= nsteps; n++) {
     T = T+1;
     printf(" %f \n",T);
  /*   ------- Start of the Main FDTD Loop ----------      */

   /* Put a Sinusoidal Source */

    pulse = exp(-pow(T/60,2))* sin(www*dt*T);
    /* hz[ic][jc] = pulse;  */
    pulseback = exp(-pow(T/60,2))*sin(www*dt*T + kshft);
    pulseey= exp(-pow((T+0.5)/60,2))*sin(www*dt*(T+0.5) - (kshft/2));
    pulseex = exp(-pow((T+0.5)/60,2))*sin(www*dt*(T+0.5)+(3.14159/2));

    for(j=0; j< JE; j++) {
      hz[1][j] = pulse*dummy1[j];
    }

  /* Calculate the Dx field */
  /* separates the known field from the scattered field in the j direction*/
    for ( j=0; j<JE-1; j++) {
      for ( i = 0; i< IE-1; i++ ) {
        if (j==JE-npml)
            curlh = (hz[i][j+1]+hz[i][j]*factor3) - hz[i][j];
        else if (j==npml)
            curlh =  hz[i][j+1] -(hz[i][j] +hz[i][j+1]*factor1);
        else curlh = hz[i][j+1] - hz[i][j];
        idx[i][j] = idx[i][j] + gi1[i]*curlh;
        dx[i][j] = gj3[j]*dx[i][j] +
          gj2[j]*(0.5*curlh + idx[i][j]);
            }
```

```
      }

      /* Calculate the Dy field */
      /* Adds in the source hz field 1 point behind the real source */
      for ( j=0; j<JE; j++) {
        for ( i = 0; i< IE-1; i++ ) {
          if (i==0) curlh = -hz[i+1][j] + (pulse*dummy1[j] + hz[i][j]);
          else curlh = -hz[i+1][j] + hz[i][j];
          idy[i][j] = idy[i][j] + fj1[j]*curlh;
          dy[i][j] = fi3[i]*dy[i][j] +
            fi2[i]*(0.5*curlh + idy[i][j]);
        }
      }

      /* Calculate the Ex and Ey field from D field */
/*      for(j=1; j<=lim1;j++) {
        for(i=1; i< IE-1; i++) {
          ex[i][j] = dx[i][j]/epss;
          ey[i][j] = dy[i][j]/epss;
        }
      }

      for(j=lim1+1; j<=lim2;j++) {
        for(i=1; i<IE-1; i++) {
          ex[i][j] = (dx[i][j] - ix[i][j] - sx[i][j]*exp(-dt/t0))/
            (1+ sigeps*dt + chi1*dt/t0)   ;
          ey[i][j] = (dy[i][j] - iy[i][j] - sy[i][j]*exp(-dt/t0))/
            (1+ sigeps*dt + chi1*dt/t0)  ;
          iy[i][j] = iy[i][j] + sigeps*dt*ey[i][j];
          ix[i][j] = ix[i][j] + sigeps*dt*ex[i][j];
          sy[i][j] = exp(-dt/t0) * sy[i][j] + chi1*dt*ey[i][j]/t0;
          sx[i][j] = exp(-dt/t0) * sx[i][j] + chi1*dt*ex[i][j]/t0;
        }
      }

      for(j=lim2+1; j< JE-1; j++) {
        for(i=1; i< IE-1;i++) {
          ex[i][j] = dx[i][j];
          ey[i][j] = dy[i][j];
        }
      }                                */
      for(j=1; j<JE-1; j++){
         for(i=1;i<IE-1;i++){
          ex[i][j] = dx[i][j];
          ey[i][j] = dy[i][j];
         }
      }
      /* Add in the hard source E-field in both x and y directions */
      for(j=npml+1; j<JE-npml-1;j++) {
          ex[1][j] = dummy3[j]*pulseex;
          ey[1][j] = dummy2[j]*pulseey;
      }
```

```
    /* printf(%3f   %6.2f \n", T, ez[ic][jc]); */

    /* Set the Ez edges to 0, as part of the PML */
    for( j = 0; j< JE-1; j++ ) {
      ey[0][j] = 0.0;
      ey[IE-1][j] = 0.0;
      hz[0][j] = 0.0;
      hz[IE-1][j] = 0.0;
    }
    for(i=0; i < IE-1; i++) {
      ey[i][0] = 0.0;
      ey[i][JE-1] = 0.0;
      hz[i][0] = 0.0;
      hz[i][JE-1] = 0.0;
    }

    /* Calculate the Hz field */
    /* subtracts out the source term */
    for( j=1; j< JE-1; j++) {
      for ( i = 2; i < IE - 1; i++) {
/*          if (j==JE-npml-1)
        {
          if (i==1) curl_e = (ex[i][j+1]+ex[i][j]*factor3)
              - ex[i][j] -
             (ey[i+1][j]-pulseey*dummy2[j]) +ey[i][j] ;
          else curl_e = (ex[i][j+1]+ex[i][j]*factor3) -
             ex[i][j] -ey[i+1][j] +ey[i][j] ;
        }
        else if (j==npml -1)
        {
        if (i==1) curl_e = (ex[i][j+1]-ex[i][j+1]*factor1)
             - ex[i][j] -
            (ey[i+1][j]-pulseey*dummy2[j]) +ey[i][j] ;
        else curl_e = (ex[i][j+1]-ex[i][j+1]*factor1)
             - ex[i][j] -ey[i+1][j] +ey[i][j] ;
        }
        else
        { */  if (i==1) curl_e = ex[i][j+1] - ex[i][j] -
               (ey[i+1][j]-pulseey*dummy2[j]) +ey[i][j] ;
             else curl_e = ex[i][j] - ex[i][j-1] -ey[i][j] +ey[i-1][j] ;
       /* } */
        hz[i][j] = gi3[i]*fj3[j]*hz[i][j]
          + gi2[i]*fj2[j]*0.5* curl_e ;
      }
    }

  }
  /*   ------ end of the main FDTD loop ------- */

  /* for( j=1; j<jc; j++)  {
    printf( "%2d   ",j);
    for( i = 1; i<ic; i++ ) {
      printf( "%5.2f ", ez[2*i][2*j]);
```

```
      }
      printf( " \n");
    } */
    printf("t = %5.0f \n", T);

    /* write the Hz field out to a file "Hz" */
    fp = fopen( "Hz", "w");
    for( j= 0; j < JE; j++) {
      for(i=0; i < IE; i++) {
        fprintf( fp, "%6.3f ", hz[i][j]);
      }
      fprintf(fp, " \n");
    }
    fclose(fp);

  /* write the Ex field out to a file "Ex" */
    fp1 = fopen( "Ey", "w");
    for( j= 0; j < JE; j++) {
      for(i=0; i < IE; i++) {
        fprintf( fp1, "%6.3f \n", ey[i][j]);
      }
      /* fprintf(fp, " \n");  */
    }
    fclose(fp1);

    /* write hz field enveloppe out to a file "dummy" */
    fp2 = fopen( "dummy", "w");
    for( j= 0; j < JE; j++) {
        fprintf( fp2, "%6.3f \n", dummy1[j]);
      }
    fclose(fp2);
  }
}

double **dmatrix(long nrl, long nrh, long ncl, long nch)
/* allocate a double matrix with subscript range m[nrl..nrh][ncl..nch] */
{
long i, nrow=nrh-nrl+1,ncol=nch-ncl+1;
double **m;
/* allocate pointers to rows */
m=(double **) malloc((size_t)((nrow+NR_END)*sizeof(double*)));
/* if (!m) nrerror("allocation failure 1 in matrix()");    */
m += NR_END;
m -= nrl;
/* allocate rows and set pointers to them */
m[nrl]=(double *) malloc((size_t)((nrow*ncol+NR_END)*sizeof(double)));
/* if (!m[nrl]) nrerror("allocation failure 2 in matrix()");    */
m[nrl] += NR_END;
m[nrl] -= ncl;
for(i=nrl+1;i<=nrh;i++) m[i]=m[i-1]+ncol;
/* return pointer to array of pointers to rows */
return m;
}
```

BIBLIOGRAPHY

1 K. Krane, *Modern Physics* (John Wiley and Sons, New York, 1983).

2 G. P. Agrawal (Academic Press, San Diego, 2001) and references within.

3 D.J. Griffiths, *Introduction to Electrodynamics* (Prentice Hall, Upper Saddle River, 1999).

4 J.M. Liu, *Photonic Devices* (Cambridge University Press, Cambridge, 2005).

5 D. Demille, *Applied Physics Letters*, vol. 74, p. 4165 (1995).

6 A. Gongora and P.G.H. Sandars, Journal of Physics B: Atomic and Molecular Physics, vol. 19, p. 291 (1986).

7 R. Zia, *Guided Polariton Optics: A Combined Numerical, Analytical and Experimetnal Investigation of Surface Plasmon Waveguides*, PhD dissertation, Stanford University, 2006.

8 Melles Griot Catalog, 2005.

9 M. Born and E. Wolf, *Principles of Optics* (Cambridge University Press, Cambridge, 2003).

10 G.B. Airy, *Transactions of the Cambridge Philosophical Society*, vol. 5, p. 283 (1835).

11 A. Graff, D. Wagner, H. Ditlbacher and U. Kreibig, *European Physical Journal D*, vol. 34, p.263 (2005).

12 C. Kittel, *Introduction to Solid State Physics* (John Wiley and Sons, New York, 1996).

13 H. Raether, *Surface Plasmons*, vol. 111 of Springer-Verlag Tracts in Modern Physics (Springer-Verlag, New York, 1988).

14 E.N. Economou, *Physical Review,* vol. 182, no. 2, p539 (1969).

15 J.R. Sambles, G.W. Bradbery and F.Z. Yang, *Contemporary Physics*, vol. 32, p.173 (1991).

---

16 A.H. Wilson, *The Theory of Metals* (Cambridge University Press, London, 1936).

17 P.A.M. Dirac, *The Principles of Quantum Mechanics* (Clarendon Press, Oxford, 1996).

18 M. Fleischman, P.J. Hendra and A.J. McQuillan, *Chemical Physics Letters*, vol. 26, p.123 (1974).

19 T.M. Cotton, S.G. Schultz and R.P. Van Duyne, *Journal of the American Chemical Society*, vol. 102, p7962 (1980).

20 D.L. Jeanmaire and R.P. Van Duyne, *Journal of Electroanalytical Chemistry*, vol. 4, p.1 (1977).

21 S. Nie and S.R. Emory, *Science*, vol. 275, p. 1102 (1997).

22 K. Kneipp, H. Kneipp and M. Rentsch, *Journal of Molecular Structure*, vol. 76, p. 2444 (1996).

23 www.mesophotonics.com

24 R.K. Chang and T.E. Furtak, *Surface Enhanced Raman Scattering* (Plenum Press, New York, 1982).

25 M. Moskovits, *Journal of Raman Spectroscopy*, vol. 36, p. 485 (2005).

26 P. Etchegoin, L.F. Cohen, H. Hartigan, R.J.C. Brown, M.J.T. Milton and J.C. Gallop, *Journal of Chemical Physics*, vol. 119, p. 5281 (2003).

27 F.J. Garcia-Vidal and J.B. Pendry, *Physical Review Letters*, vol. 77, p.1163 (1996).

28 L. Novotny, R.X. Bian and X. S. Xie, *Physical Review Letters*, vol. 79, no. 4, p645 (1997).

29 O.J.F Martin and C. Girard, *Applied Physics Letters*, vol. 70, p705 (1997).

30 A.V. Bragas, S.M. Landi and O.E. Martinex, *Applied Physics Letters*, vol. 72, p.2075 (1998).

31 S. Grafstrom, *Journal of Applied Physics*, vol. 91, no. 4, p1717 (2002).

32 E.J. Sanchez, L. Novotny and X.S. Xie, *Physical Review Letters*, vol. 82, p. 4014 (1999).

---

33 A. Hartschuh, E.J. Sanchex, X.S. Xie and L. Novotny, *Physical Review Letters*, vol. 90, 095503 (2003).

34 A.Chimmalgi, T.Y. Choi, C.P. Grigoropoulos and K. Komvopoulos, *Applied Physics Letters*, vol. 82, no. 8, p. 1146 (2003).

35 J. Takahara, S. Yamagishi, H. Taki, A. Morimoto and T. Kobayashi, *Optics Letters*, vol. 22, 475 (1997).

36 T. Ono, M. Esashi, H. Yamada, Y. Sugawara, J. Takahara and K. Hane, Integrated and Functional Probes, p. 130 (from *Nano-Optics*, ch 5).

37 A.J. Badabjanyan, N.L. Maragaryan and K.V. Nerkararyan, *Journal of Applied Physics*, vol. 87, p. 3785 (2000).

38 R. Ruppin, *Physics Letters A*, vol. 340, p. 299 (2005).

39 M.I. Stockman, *Physical Review Letters*, vol. 93, no. 13, 137404 (2004).

40 A.D. Boardman, Hydrodynamic Theory of Plasmon-Polaritons on Plane Surfaces, p. 1 (from *Electromagnetic Surface Modes*, ch. 1).

41 W.L. Barnes, A. Dereux and T.W. Ebbesen, *Nature*, vol. 424, p. 824 (2003).

42 T.W. Ebbesen, H.J. Lezec, H.F. Ghaemi, T. Thio and P.A. Wolff, *Nature*, vol. 391, p. 667 (1998).

43 A. Krishnan, T. Thio, T.J. Kim, H.J., Lezec, T.W. Ebbesen, P.A. Wolff, J. Pendry, L. Martin-Moreno and F.J. Garcia-Vidal, *Optics Communications*, vol. 200, p. 1 (2001).

44 L. Martín-Moreno, F.J. Garcia-Vidal, H.J. Lezec, A. Degiron, A. and T.W. Ebbesen, *Physical Review Letter,* vol. 90**,** 167401 (2003).

45 H.J. Lezec, A. Degiron, E. Devaux, R.A. Linke, L. Martin-Moreno, F.J. Garcia-Vidal and T.W. Ebbesen, *Science*, vol. 297, p. 820 (2002).

46 W. Srituravanich, N. Fang, S. Durant, M. Ambati, C. Sun and X. Zhang, *Journal of Vacuum Science Technology B*, vol. 22, no. 6, pp.3475 (2004).

47 T. Thio, K.M. Pellerin and R.A. Linke, *Optics Letters*, vol. 26, p. 1972 (2001).

48 D. Zeisel, S. Nettesheim, B. Dutoit and R. Zenobi, *Applied Physics Letters*, vol. 68, p. 2491 (1996).

---

49 X. Shi, *Resonant Optical Transmission through a Single Sub-wavelength Aperture for Near Field Applications*, PhD Dissertation, Stanford University (2003).

50 T. Yatsui, M. Kourogi and M. Ohtsu, *Applied Physics Letters*, vol. 73, p. 2090 (1998).

51 N. Kroo, J.P. Thost, M. Volcker, W. Krieger and H. Walther, *Europhysics Letters*, vol. 15, p. 289 (1991).

52 D. Sarid, *Physical Review Letters*, vol. 47, p. 1927 (1981).

53 F.Y. Kou and T. Tamir, *Optics Letters*, vol. 12, p. 367 (1987).

54 K. Leosson, T Nikolajsen, A. Boltasseva and S.I. Bozhevolnyi, *Optics Express*, vol. 14, p. 314 (2006).

55 L.D. Landau, E.M. Lifshitz and L.P. Pitaevskii, *Electrodynamics of Continuous Media* (Butterworth-Heinenann, Oxford, 2002).

56 R.E. Collin, *Field Theory of Guided Waves* (IEEE Press, New York, 1991).

57 L.G. Schulz and F. R. Tangherlini, *Journal of the Opical Society of America*, vol. 44, p. 362 (1954).

58 L.G. Schulz, *Journal of the Opical Society of America*, vol. 44, p. 357 (1954).

59 V.G. Padalka and I.N. Shklyarevskii, *Opt. Spectr. U.S.S.R.* vol. 11, p. 285 (1961).

60 R. Philip and J. Trompette, *Compt. Rend.,* vol. 241, p. 627 (1955).

61 P.B. Johnson and R.W. Christy, *Physical Review B*, vol. 6, p. 4370 (1972).

62 E. Palik, *Handbook of Optical Constants of Solids* (Academic Press, New York, 1985).

63 A. Liebsch, *Electronic Excitations at Metal Surfaces* (Plenum Press, New York, 1997).

64 H. Ehrenreich and H.R. Phillip, *Physical Review*, vol. 128, no. 4 (1962).

65 G. Timp, et al., *IEDM Technical Digest,* pp. 615 (IEDM, San Francisco, 1998).

66 ITRS Roadmap, 2005.

---

67 B. Pettinger, G. Picardi, R. Schuster and G. Ertl, *Single Molecules*, vol. 5, p. 285 (2002).

68 M. Iwami, Y. Uehara and S. Ushioda, *Japanese Journal of Applied Physics*, vol. 39, no. 8, p. 4912 (2000).

69 K. Dickmann, F. Demming and J. Jersch, *Review of Scientific Instruments*, vol. 67, no. 3, p. 846 (1996).

70 J.P. Kottmann and O.J.F. Martin, *Optics Express*, vol. 8, no. 12, p. 655 (2001).

71 F. Moresco, M. Rocca, T. Hildebrandt and M. Henzler, *Physical Review Letters*, vol. 83, no. 11, p. 2238 (1999).

72 R. Zia, M.D. Selker, P.B. Catrysse and M.L. Brongersma, *Journal of the Optical Society of America,* vol. 21, p.12 (2004).

73 F.A. Burton and S.A. Cassidy, *Journal of Lightwave Technology*, vol. 8, no. 12, p. 1843 (1990).

74 C. Chen, P. Berini, D. Feng, S. Tanev and V.P. Tzolov, *Optics Express*, vol. 7, p. 260 (2000).

75 E. Anemogiannis and E.N. Glytsis, *Journal of Lightwave Technology,* vol. 10, p.1344 (1992).

76 A.K. Wong, *Resolution Enhancement Techniques in Optical Lithography* (SPIE Press, Bellingham, 2001).

77 G.E.H. Reuter and E.H. Sondheimer, *Proceedings of the Royal Society of London Series A*, vol. 195, no. 1042, p. 336 (1948).

78 C. Hinde, Plasmons in a Channel of Variable Width, unpublished (2005).

79 D.K. Gramotnev, *Journal of Applied Physics*, vol. 98, 104302 (2005).

80 G.I. Stegeman, N.E. Glass, A.A. Maradudin, T.P. Shen and R.F. Wallis, *Optics Letters*, vol. 8, p. 626 (1983).

81 K.V. Nerkararyan, *Physics Letters A*, vol. 237, p. 103 (1997).

82 R. Caflisch, Plasmons in a Channel of Variable Width, unpublished (2004).

---

83 A. Taflove and S.C. Hagness, *Computational Electrodynamics, the Finite-Difference Time-Domain Method* (Artech House, Boston, 2000).

84 D.M. Sullivan, *Electromagnetic Simulation Using the FDTD Method* (IEEE Press, Piscataway, 2000).

85 K.S. Yee, *IEEE Transactions on Antennas and Propagation*, vol. 14, p. 302 (1966).

86 H.T. Miyazaki and Y. Kurokawa, *Physical Review Letters*, vol. 96, 097401 (2006).

87 G.I. Stegeman, R.F. Wallis and A.A. Maradudin, *Optics Letters*, vol. 8, p. 396 (1983).

88 J.D. Joannopoulos, R.D. Meade and J.N. Winn, *Photonic Crystals* (Princeton University Press, Princeton, 1995).

89 E.M. Anderson, *Electric Transmission Line Fundamentals* (Reston Publishing Company, Reston, 1985).

90 S. Ramo, J.R. Whinnery and T. Van Duzer, *Fields and Waves in Communication Electronics* (John Wiley and Sons, Singapore, 1994).

91 P. Horowitz and W. Hill, *The Art of Electronics* (Cambridge University Press, Cambridge, 1989).

92 A. Alu and N. Engheta, *Journal of the Optical Society of America B*, vol. 23, no. 3, p. 571 (2006).

93 T.C. Paulick, *Journal of Applied Physics*, vol. 64, p. 1384 (1988).

94 D.L. Mills, *Physical Review B*, vol. 12, p. 4036 (1975).

95 M. Staffaroni, Consequences of Surface Roughness, unpublished (2005).

96 M. Rocca, *Surface Science Report*s, vol. 22, p. 1 (1995).

97 S. Suto, K.D. Tsuei, E.W. Plummer and E. Burstein, *Physical Review Letters*, vol. 63, p. 2590 (1989).

98 M. Rocca, *Surface Science Reports*, vol. 22, p. 1 (1995).

99 R. Contini and J.M. Layet, *Solid State Communications*, vol. 64, p. 1179 (1987).

100 J.D. Jackson, *Classical Electrodynamics* (John Wiley and Sons, Singapore, 1999).

101 R.H. Ritchie, *Progress of Theoretical Physics*, vol. 29, p. 607 (1963).

102 H. Raether, *Excitation of Plasmons and Interband Transitions by Electrons* (Springer-Verlag, New York, 1980).

103 E.H. Sondheimer, *Advances in Physics*, vol. 1, p. 1 (1952).

104 U. Kreibig and C.V. Fragstein, *Z. Physik*, vol. 224, p. 307 (1969).

105 A.B. Pippard, *Proceedings of the Royal Society of London A*, vol. 191, p. 385 (1947).

106 J.T. Verdeyen, *Laser Electronics* (Prentice Hall, Upper Saddle River, 2000).

107 K.L. Kliewer and R. Fuchs, *Physical Review*, vol. 172, p. 607 (1968).

108 D. Pines, *Elementary Excitations in Solids* (Benjamin, New York, 1963).

109 K. Fuchs, *Proceedings of the Cambridge Philosophical Society*, vol. 34, p. 100 (1938).

110 D.P. Siu, *Surface Plasmon Effects in Metal-Barrier-Metal Structures*, PhD Dissertation, Univeristy of California at Berkeley, 1978.

111 http://www.seagate.com/cda/newsinfo/newsroom/releases /article/0,1121,1503,00.html

112 C.A. Balanis, *Advanced Engineering Electromagnetics* (John Wiley and Sons, Hoboken, 1989).